nature cell biology

Article

https://doi.org/10.1038/s41556-025-01827-2

Lineage-determining transcription factors constrain cohesin to drive multi-enhancer oncogene regulation

Received: 7 May 2025

Accepted: 28 October 2025

Published online: 02 December 2025

Check for updates

Yeqiao Zhou[1,2,3,9], Atishay Jay[2,3,4,5,9], Noah Burget[1,2,3], Tobias Friedrich[1,2,3], Sora Yoon[4], Jessica Alsing[6], Guy Nir[7], Rudolf Grosschedl[8], Golnaz Vahedi[2,3,4] ✉ & Robert B. Faryabi[1,2,3] ✉

Multiple enhancers, often separated by vast genomic distances, regulate key genes. However, how the folding of individual chromatin fibres enables cell-type-restricted multi-enhancer regulation remains unclear. Here, using acute protein degradation and time-resolved chromatin conformation capture in mantle cell lymphoma, we found that the B cell-lineage-determining factor EBF1 organizes multiple enhancers around sparsely distributed genes essential for B cell identity and oncogenesis. Time-resolved sub-diffraction optical tracing of more than 100,000 chromatin fibres further revealed diverse topological conformations that facilitate multi-enhancer interactions. Mechanistically, we discovered that enhancer positioning at local topological centres is required for promoter engagement, with EBF1 acting as a permeable barrier to loop-extruding cohesin at enhancers. Extending these findings to T cell leukaemia, we show that lineage-determining transcription factors such as EBF1 and TCF1 radially position enhancers within gene loci to enable multi-enhancer regulation of key oncogenes at the single-allele level.

Precise spatiotemporal control of gene expression relies on the activity of *cis*-regulatory elements, including enhancers and promoters[1–6]. Previous studies have indicated that multiple distal enhancers can be in the spatial proximity of a single gene promoter[7–11]. Enhancer activation has been attributed to lineage-determining transcription factors (TFs)[12–20]. However, how these factors instruct the physical folding of individual chromatin fibre to facilitate multi-enhancer–promoter interactions remains unclear.

Sequencing-based chromatin conformation capture techniques have implicated complex enhancer–promoter interaction networks[21–26]; yet, these population-based methods obscure the behaviour of individual alleles and are limited to detecting pairwise interactions in fragmented chromatin. By contrast, Oligopaint DNA fluorescence in situ hybridization (FISH) has enabled visualization of a handful of selected regulatory elements within individual cells[27–29], but cannot resolve how enhancer and promoter positioning relates to surrounding chromatin. To overcome these limitations, we implemented Optical Reconstruction of Chromatin Architecture (ORCA)[30,31], a sequential DNA FISH-based method, to examine the precise folding of entire genomic loci at sub-diffraction resolution in individual cancer cells.

ORCA applied to the *Sox9* and *Pitx1* loci has revealed structural diversity underlying chromatin folding changes during

[1]Department of Pathology and Laboratory Medicine, University of Pennsylvania, Philadelphia, PA, USA. [2]Institute for Immunology and Immune Health, University of Pennsylvania, Philadelphia, PA, USA. [3]Epigenetics Institute, University of Pennsylvania, Philadelphia, PA, USA. [4]Department of Genetics, University of Pennsylvania, Philadelphia, PA, USA. [5]Department of Bioengineering, University of Pennsylvania, Philadelphia, PA, USA. [6]Department of Pharmacology and Toxicology, University of Texas Medical Branch, Galveston, TX, USA. [7]Department of Biochemistry and Molecular Biology, University of Texas Medical Branch, Galveston, TX, USA. [8]Max Planck Institute of Immunobiology and Epigenetics, Freiburg, Germany. [9]These authors contributed equally: Yeqiao Zhou, Atishay Jay. ✉e-mail: vahedi@pennmedicine.upenn.edu; faryabi@pennmedicine.upenn.edu

development[32,33], primarily focusing on the interplay between topologically associating domains (TADs), the loop-extruding cohesin complex and the insulator protein CTCF. Unlike cell-type-invariant TADs, enhancer activity and positioning are highly lineage- and disease-specific[2,3,11,25,27,34]. Notably, loss of cohesin or CTCF profoundly alters TAD structures with context-dependent effects on enhancer–promoter interactions and transcription[35–41], suggesting that the requirement for these architectural factors may be context dependent.

Lineage-determining TFs are known to activate lineage-specific enhancers in normal and cancer cells[42–44], but their role in the spatial positioning of enhancers remains poorly understood. Recent studies have shown that the T cell-lineage-determining factor TCF1 (ref. 45) and the pluripotent factor KLF4 (ref. 46) contribute to chromatin reorganization in their corresponding developmental contexts. We and others have also shown that NOTCH1, a key signalling-dependent oncogenic TF, contributes to reorganization of enhancer–promoter interactions in cancers[27,47]. These population-level studies provide evidence that non-architectural TFs contribute to enhancer positioning. However, how lineage-determining TFs organize locus-wide chromatin folding to instruct multi-enhancer gene regulation remains unknown.

In this study, we optically traced chromatin at four loci in mantle cell lymphoma (MCL) and T acute lymphoblastic leukaemia (T-ALL) to examine how chromatin folding at individual alleles enables cancer-type-restricted multi-enhancer gene regulation (Supplementary Table). Through time-resolved tracing of >100,000 chromatin fibres, we discovered that the placement of distal enhancers and promoters toward local spatial centres is required for their long-range interactions. We demonstrated that B and T cell-lineage-determining TFs EBF1 (ref. 43) and TCF1 (ref.48) bind cancer-type-restricted enhancers and act as permeable barriers to cohesin traffic, thereby restricting loop extrusion and promoting the local centralization of interacting enhancers and promoters. These findings suggest a general mechanism by which lineage-determining TFs coordinate the spatial positioning of multiple regulatory elements to control gene expression and drive oncogenesis.

Results

EBF1 binds distal enhancers and promotes MCL survival

To elucidate the role of lineage-determining TFs in cancer-type-restricted multi-enhancer gene regulation, we examined the dependency of B cell lymphomas to EBF1, a TF that is required for B cell-lineage specification[49–51]. Analysis of published datasets[52] revealed high expression and essentiality of *EBF1* across several non-Hodgkin B cell lymphomas, including MCL (Extended Data Fig. 1a), the observations that were further supported by our CRISPR-Cas9-mediated knockout of EBF1 in additional MCL models (Extended Data Fig. 1b–d). This finding prompted us to examine the activity of EBF1-bound genomic elements in MCL Granta519. High-confidence EBF1-bound elements, identified using two independent EBF1 antibodies, were enriched for enhancer-associated histone marks H3K27ac and H3K4me1, while being depleted of the Polycomb-associated repressive mark H3K27me3 (Fig. 1a). Additionally, 75% of EBF1-bound elements were located more than 10 kb from active gene promoters (Extended Data Fig. 1e).

EBF1 degradation and restoration rapidly alter EBF1 chromatin binding in MCL

Observing that EBF1 predominantly binds distal enhancers in MCL led us to examine its immediate effects on enhancer activity and positioning. We employed the dTAG degron system[53] and generated ~100 independent MCL Granta519 clones in which $FKBP^{F36V}$ degradation tag was knocked into the endogenous *EBF1* C terminals (hereafter EBF1-FKBP-KI MCL) (Extended Data Fig. 1f). Among these independent lines, clones 97 and 27 were transcriptionally most similar to parental Granta519 cells and were therefore used for all subsequent studies (Extended Data Fig. 1g).

Temporal immunoblotting analysis with a polyclonal anti-EBF1 antibody (RG)[43], recognizing an N-terminal EBF1 peptide, showed acute depletion and full restoration of EBF1 as early as 2 h after dTAG ligand $dTAG^{V}$-1 (hereafter dTAG) addition and washout, respectively (Fig. 1b). Prolonged EBF1 degradation phenocopied EBF1 knockout and impaired MCL proliferation (Fig. 1c). In contrast to EBF1 knockout, 24-h acute EBF1 depletion had only a marginal impact on EBF1-FKBP-KI MCL proliferation (Fig. 1c).

Using ChIP-seq to examine EBF1 chromatin occupancy dynamics, we identified 7,777 bona fide EBF1-binding sites at which chromatin-bound EBF1 was efficiently removed and restored following 6-h dTAG ligand addition and washout, respectively (Fig. 1d). Thus, the EBF1 degron system provided a tractable and robust strategy to dissect the direct effects of EBF1 on MCL chromatin structure and topology on an hourly timescale without affecting cell proliferation. Unless otherwise stated, all subsequent experiments were performed at short time points of 6 and 24 h.

Fig. 1 | EBF1 binds distal enhancers in gene-dense and gene-sparse hubs. **a**, Heatmap displaying enrichment of active histone marks at 25,227 reproducible EBF1-binding sites determined by two ChIP-grade antibodies (RG and MP). EBF1-binding sites are ordered by hierarchical clustering of normalized EBF1, H3K27ac, H3K4me1 and H3K27me3 ChIP-seq signals. **b**, Western blotting of EBF1 in EBF1-FKBP-KI Granta519 clones 27 and 97 showing rapid and reproducible removal and restoration of EBF1 protein levels after $dTAG^{V}$-1 (referred to as dTAG) treatment and washout, respectively. The 125 nM dTAG treatment and washout (WO) are examined for 0–24 h. β-Actin is a loading control. **c**, EBF1 loss impedes growth of Granta519 clone 27. Relative cell growth (CellTiter Glo) of clone 27 with or without 125 nM dTAG treatment for 6 days. Data represent mean ± s.e.m. of $n = 5$ biological replicates. *P* value obtained by two-sided *t*-test. **d**, Heatmap of EBF1 occupancy showing 7,777 bona fide EBF1-bound elements determined with $\log_2$(fold change) < −1 in EBF1-removed (6 h + dTAG and 24 h + dTAG versus 0 h) and $\log_2$(fold change) > 1 in EBF1-restored (6 h WO and 24 h WO versus 24 h + dTAG) Granta519 clone 27. Each column is centred on EBF1-bound elements ± 2-kb flanking sequences with 50-bp resolution. **e**, Pileup plots showing TAD boundaries are invariant in Granta519-Cas9 cells with (top) and without (bottom) EBF1 expression. Centred around 575 EBF1-bound TAD boundaries (left). 1,867 EBF1-unbound boundaries (right). **f**, Population-average enhancer–promoter hubs defined by EBF1 and SMC1 HiChIP in Granta519. Groups of interacting enhancers and/or promoters are plotted in an ascending order of their total pairwise interactions from EBF1 HiChIP using RG antibody (left), MP antibody (middle) and SMC1 HiChIP (right). Population-average enhancer–promoter hubs are defined as the groups of enhancers and promoters with total pairwise interactions above the elbow of total interaction distribution. The top two hubs of each HiChIP are marked and named with their representative genes. RG, a polyclonal anti-EBF1 antibody recognizing an N-terminal EBF1 peptide; MP, Millipore anti-EBF1 antibody. **g**,**h**, Gene-dense *DOT1L* and gene-sparse *BCL2* hubs display distinct distributions of enhancers and promoters and loops across comparable linear genomic spans. ChIP-seq tracks showing enrichment of EBF1, SMC1, CTCF and H3K27ac at proximal and distal enhancers of *DOT1L* (**g**) and *BCL2* (**h**), which are the top two highest interacting hubs defined in **f**. HiChIP arcs displaying normalized significant interactions among enhancers and promoters. Bottom track indicating positions of expressed Ensembl genes in Granta519. **i**, Box-and-whisker plots showing higher number of genes per megabase in gene-dense compared with gene-sparse hubs defined by SMC1 HiChIP. The number of hubs in each group is listed in parentheses. Box-and-whisker plots show centre line, median; box limits, upper (75th) and lower (25th) percentiles; and whiskers, 1.5 × interquartile range. *P* values obtained by a two-sided Wilcoxon rank-sum test. **j**, Barplots depicting the fraction of interactions among enhancers (E) and promoters (P) in gene-dense and gene-sparse hubs defined by EBF1 HiChIP, RG antibody. The number of hubs in each group is listed in parentheses. **k**,**l**, Gene Ontology (GO) terms specifically enriched in gene-dense (**k**) or gene-sparse (**l**) hubs. The top 500 expressed genes in each class of hubs are used as input. Source numerical data and unprocessed blots are available in source data.

https://doi.org/10.1038/s41556-025-01827-2

MCL chromatin accessibility, TAD boundaries and compartments are insensitive to rapid EBF1 changes

Chromatin structure and topology are both crucial for precise gene expression control[8,11,54–56]. Given that EBF1 establishes lineage-specific chromatin accessibility during B cell specification[43,57], we first examined EBF1 immediate impact on MCL chromatin structure. Time-resolved ATAC-seq revealed a substantial loss of chromatin accessibility 48 h after EBF1 removal (Extended Data Fig. 1h,i) coinciding with significantly impaired proliferation (Fig. 1c). By contrast, chromatin accessibility remained unchanged 6 h and 24 h after dTAG ligand addition and washout, indicating that the immediate effects of EBF1 on MCL chromatin accessibility are minimal.

Compartments and TADs are population-level features of chromatin architecture that influence enhancer positioning, activity and specificity[1,58,59]. Examination of TAD boundaries and compartments by in situ Hi-C showed that EBF1-bound TAD boundaries were invariant to EBF1 knockout (Fig. 1e and Extended Data Fig. 1b). Similarly, loss of EBF1 for 3 days did not markedly alter MCL genome compartmentalization

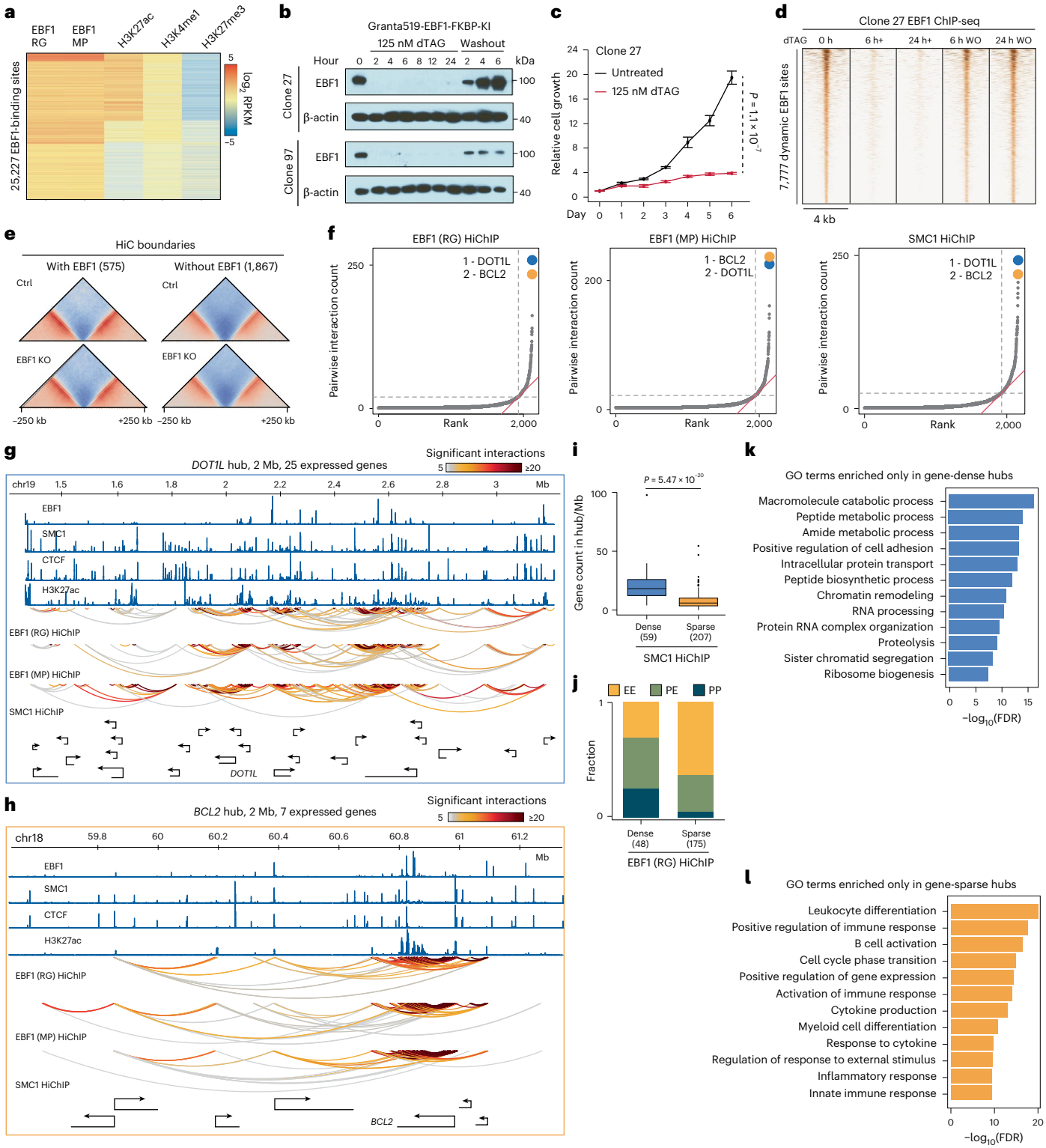

(Extended Data Fig. 1j). Thus, compartments and TAD boundaries remain stable despite rapid or prolonged EBF1 depletion in MCL.

EBF1-involved interactions participate in MCL population-average enhancer–promoter hubs

As EBF1 loss did not alter compartments and TADs, we postulated that EBF1 organizes ensemble enhancer–promoter hubs, defined as networks of pairwise interacting enhancers and promoters detectable at the population level, though not necessarily occurring simultaneously within individual cells. To test this, we performed HiChIP using a validated antibody against the cohesin component SMC1a[23,27] and two independent EBF1 antibodies (RG and MP; Millipore) to examine high-resolution (~5 kb) pairwise interactions involving EBF1 and cohesin.

To investigate potential interplay between EBF1 and ensemble enhancer–promoter hubs, we first compared H3K27ac, EBF1 and YY1 occupancy at enhancer and promoter elements engaged in cohesin-mediated loops (Extended Data Fig. 1k). As expected, H3K27ac was equally enriched at enhancers and promoters interacting with other enhancers or promoters, whereas YY1, which preferentially binds promoters[60], was more abundant at promoter–promoter interactions. In contrast, EBF1 preferentially bound enhancers that interact with other enhancers, suggesting a potential role for EBF1 in mediating enhancer–enhancer and/or enhancer–promoter interactions.

Intrigued by this observation, we examined the relationship between EBF1 and MCL ensemble enhancer–promoter hubs in greater detail. Interacting enhancers and promoters identified by cohesin or EBF1 HiChIP were asymmetrically distributed, with only a subset forming highly connected hubs characterized by extensive pairwise interactions (Fig. 1f). Analysis of cohesin-involved loops revealed that 12.6% of loci (266 out of 2,115) participated in ensemble hubs with up to 250 pairwise interactions. Similarly, EBF1-mediated interactions formed 186 (MP) and 223 (RG) hubs, with 171 shared between the two libraries and 166 also marked as hubs by SMC1 HiChIP (Extended Data Fig. 1l), exemplified by hubs containing the histone methyltransferase *DOT1L*[61] and the anti-apoptotic factor *BCL2* (ref. 62) (Fig. 1f). Together, these findings suggest strong concordance between highly interacting enhancer and promoter groups that coalesce through EBF1- and cohesin-associated loops.

EBF1-bound gene-dense and gene-sparse hubs encompass distinct classes of genes

To better understand the potential regulatory environments formed by EBF1-bound ensemble hubs, we closely inspected the *DOT1L* and *BCL2* loci (the two hubs with the highest numbers of EBF1- and cohesin-mediated pairwise interactions; Fig. 1f–h). Although both *DOT1L*- and *BCL2*-containing hubs consisted of interactions among highly acetylated EBF1- and SMC1-bound elements and spanned comparable linear genomic lengths, the gene-dense *DOT1L* hub harboured 3.5-times more expressed genes than the gene-sparse *BCL2* hub. Genome-wide, fewer than 25% of the EBF1-bound hubs were located in gene-dense regions with more than 15 active genes per hub (Extended Data Fig. 1m). Similar to the *DOT1L* hub, gene-dense hubs displayed disproportionately higher gene densities, with nearly fourfold more genes per megabase than gene-sparse hubs (median 16 versus 4 genes) (Fig. 1i and Extended Data Fig. 1n).

Consistent with these observations, more than 50% of pairwise interactions in gene-sparse hubs occurred between enhancers (Fig. 1j), whereas over 70% of interactions in gene-dense hubs involved either enhancer–promoter or promoter–promoter pairs. These differences suggest that gene-dense and gene-sparse hubs may be architecturally distinct. Notably, genes within gene-dense hubs function in general cellular processes such as chromatin remodelling and RNA processing (Fig. 1k), including *GAPDH*, *ACLY*, *BRD4* and *EEF1A2*. In contrast, genes within gene-sparse hubs encoded proteins involved in B cell-related pathways (Fig. 1l), exemplified by *PAX5*, *BCL2L11*, *IKZF1* and *EBF1* itself[63–65], further supporting the potential structure–function distinction between gene-dense and gene-sparse hubs.

EBF1 preferentially regulates MCL population-average gene-sparse hubs

The differential positioning of lineage-related and housekeeping genes in gene-sparse and gene-dense hubs led us to examine whether EBF1 differentially organizes these two classes of hubs. Consistent with the greater number of enhancers and promoters in gene-dense hubs, we observed more EBF1-bound regulatory elements in gene-dense than in gene-sparse hubs (Fig. 2a and Extended Data Fig. 2a). However, EBF1 binding at enhancers and promoters was significantly more dynamic in gene-sparse hubs following dTAG addition and washout (Fig. 2b,c). Concordantly, EBF1 depletion and restoration more significantly and reproducibly altered the expression of genes located in gene-sparse compared with gene-dense hubs (Fig. 2d and Extended Data Fig. 2b), exemplified by the proto-oncogene *MYC* (Fig. 2e,f) and the PD-L1-encoding gene *CD274* (Extended Data Fig. 2c–e).

Given the limited resolution of Hi-C and the dependency of HiChIP on the immunoprecipitated protein, we performed time-resolved Micro-C[21,22] to directly examine whether EBF1 differentially impacts the genome architecture of gene-sparse and gene-dense hubs. EBF1 depletion and restoration gradually altered interaction frequencies in hubs (Fig. 2g). While the number of enhancer and/or promoter loops with greater than twofold changes in interaction frequency were comparable between the two hub types, the magnitude of these changes was greater in gene-sparse hubs, which exhibited longer loops among enhancers and/or promoters (Fig. 2h,i and Extended Data Fig. 2f,g). Together, our data suggest a preferential role for EBF1 in controlling structure–function of population-average gene-sparse hubs in MCL.

Optical chromatin tracing of individual *MYC* alleles in MCL reveals pronounced EBF1-instructed topological changes

Given that *MYC* exemplified the differential impact of EBF1 on gene-sparse and gene-dense hubs in MCL, we examined its population-average looping using EBF1 and SMC1 HiChIP. We observed frequent pairwise interactions between the promoter and the two bona fide super-enhancers E1 and E2 located 525 kb and 433 kb 5′ of *MYC*, respectively[66] (Fig. 3a). However, these data cannot determine whether the *MYC* hub reflects an emergent property of population-averaged pairwise interactions or whether EBF1-instructed multiway interactions occur simultaneously within individual cells. To address this, we performed time-resolved, single-allele-resolution mapping of *MYC* locus topology using our modified ORCA protocol (a multiplexed FISH approach employing sequential hybridization for super-resolution imaging of distances between all chromatin segments along a locus[31]; Fig. 3b and Supplementary Table). We designed 5,891 primary oligonucleotide probes tiling a 900-kb region flanking the *MYC* promoter (Fig. 3a and Supplementary Table). During sequential imaging, uniquely barcoded probes marking 30-kb segments were efficiently labelled, imaged and subsequently removed until all 30 segments were precisely localized (Extended Data Fig. 3a,b). The registration of high-accuracy fiducial signals, which continuously marked alleles, enabled super-resolution measurement of the three-dimensional (3D) positions of all 30 segments in >60% of chromatin traces (Fig. 3c and Extended Data Fig. 3a), achieving substantially higher efficiency than previous studies[32,33].

We reproducibly visualized ~43,000 chromatin traces from untreated, 6-h and 24-h dTAG-treated, and 6-h and 24-h dTAG-washout EBF1-FKBP-KI MCL clones 27 and 97 (Supplementary Table). The absence of gaps between adjacent segments enabled us to use average inter-segment distances, rather than arbitrary cutoffs, to determine interacting (looping) distal segments. Across all five conditions, population-average ORCA and Micro-C interaction frequency maps

https://doi.org/10.1038/s41556-025-01827-2

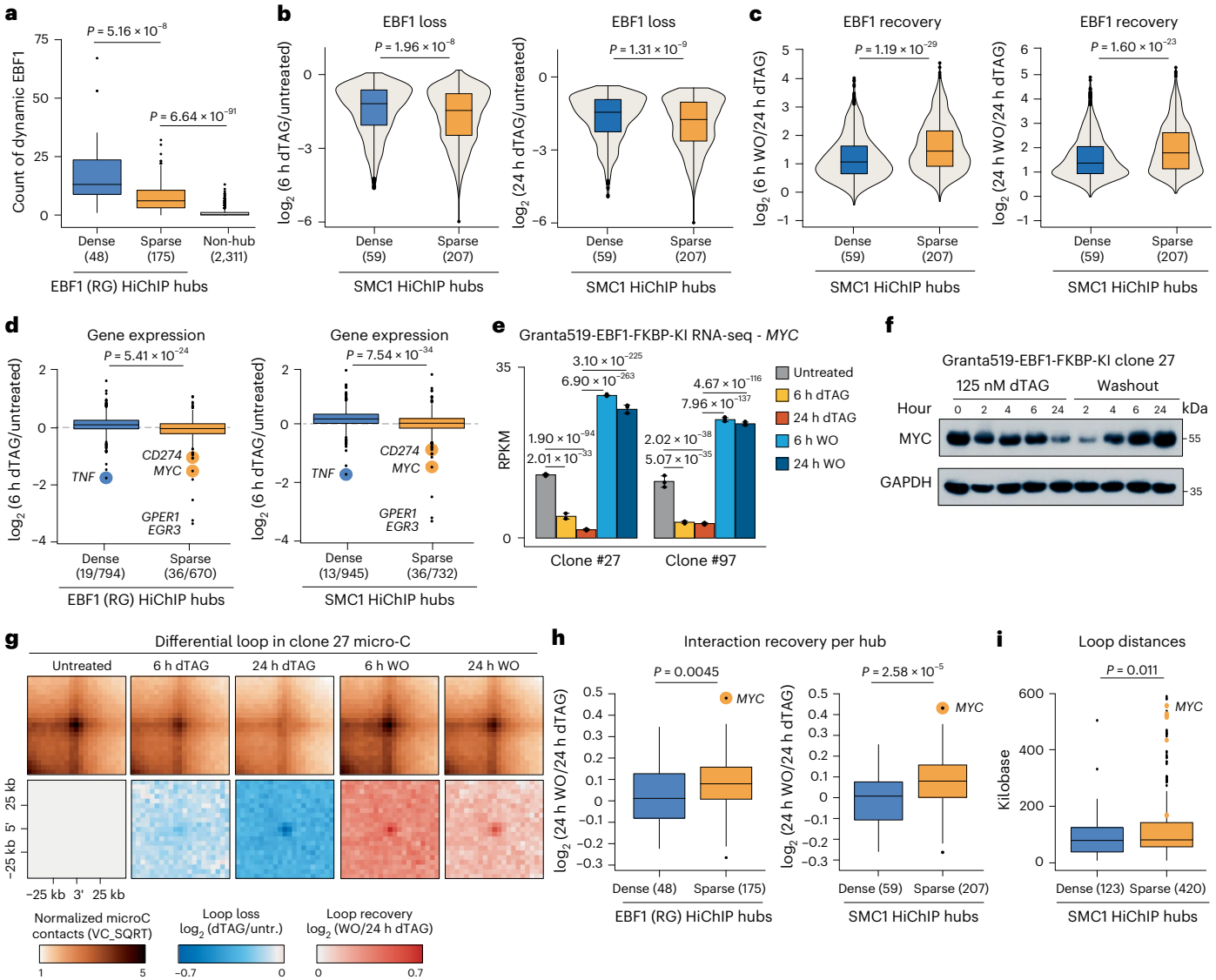

Fig. 2 | EBF1 preferentially activates target genes in gene-sparse hubs by promoting interactions with distal enhancers. a, Box-and-whisker plot comparing the number of EBF1-binding sites in gene-dense, gene-sparse and non-hub regions, as determined with EBF1 HiChIP. The number of hubs in each group is listed in parentheses. Box-and-whisker plots show centre line, median; box limits, upper (75th) and lower (25th) percentiles; whiskers, 1.5 × interquartile range. Family-wise error rate (FWER)-adjusted *P* values obtained by a two-sided Wilcoxon rank-sum test. **b**, Box-and-whisker and violin plots showing significantly higher loss of EBF1 binding in gene-sparse compared with gene-dense hubs 6 h (left) and 24 h (right) after dTAG treatment. The number of hubs in each group is listed in parentheses. Box-and-whisker plots as described in **a**. *P* values obtained by a two-sided Wilcoxon rank-sum test. **c**, Box-and-whisker and violin plots showing significantly higher recovery of EBF1 binding in gene-sparse compared with gene-dense hubs 6 h (left) and 24 h(right) after dTAG washout. The number of hubs in each group is listed in parentheses. Box-and-whisker plots as shown in **a**. *P* values obtained by a two-sided Wilcoxon rank-sum test. **d**, Box-and-whisker plots showing more significant downregulation of genes in gene-sparse compared with gene-dense hubs defined by EBF1 (left) and SMC1 (right) HiChIP 6 h after dTAG treatment. Note that there are fewer expressed genes in gene-sparse hubs. Numbers of differential/expressed genes in each group are listed in parentheses. Box-and-whisker plots as in **a**. *P* values obtained by a two-sided Wilcoxon rank-sum test. **e**, Barplots of normalized RNA-seq reads showing significant *MYC* down- and upregulation 6 h and 24 h after dTAG treatment and washout, respectively, in Granta519-EBF1-FKBP-KI clones 27 and 97. Data represent mean ± s.d. of three replicates per condition. False discovery rate (FDR) from DESeq2. **f**, Time-course western blotting showing MYC protein levels in Granta519-EBF1-FKBP-KI clone 27 after dTAG treatment and washout. GAPDH is loading control. **g**, Pileup plots of normalized time-course Micro-C interaction maps of clone 27 showing interactions among enhancers and promoters in EBF1 HiChIP hubs decrease upon dTAG treatment and recover after dTAG washout. Each heatmap showing ±25-kb flanking the centre with 5-kb resolution. **h**, Box-and-whisker plots showing significantly stronger recovery of Micro-C interactions among enhancers and promoters 24 h after dTAG washout in gene-sparse compared with gene-dense hubs as defined by EBF1 (left) and SMC1 (right) HiChIP. Yellow dots represent the average $\log_2$(fold change) of 24 h washout over 24 h dTAG of interactions in *MYC* hubs. The number of hubs in each group is listed in parentheses. Box-and-whisker plots as in **a**. *P* values obtained by a two-sided Wilcoxon rank-sum test. **i**, Box-and-whisker plots showing longer genomic distances of interactions among enhancers and promoters in gene-sparse compared with gene-dense hubs. Yellow dots represent interactions of the *MYC* hub. The number of loops in each group is listed in parentheses. Box-and-whisker plots are as shown in **a**. *P* values obtained by a two-sided Wilcoxon rank-sum test. Source numerical data and unprocessed blots are available.

https://doi.org/10.1038/s41556-025-01827-2

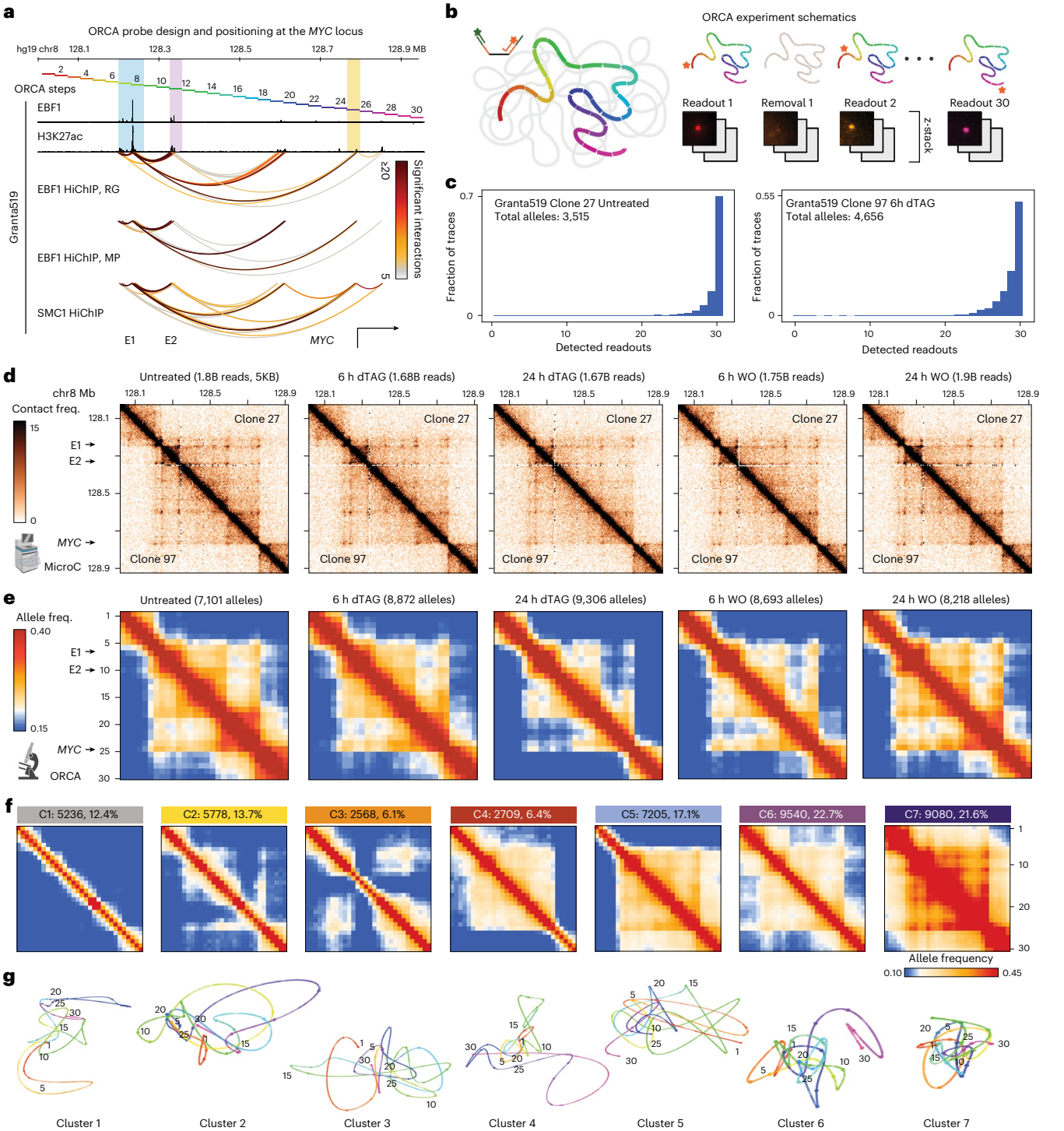

Fig. 3 | Single-allele optical tracing of the *MYC* locus reveals EBF1-instructed topological changes. a, ChIP-seq tracks showing EBF1 and H3K27ac at the two distal super-enhancers E1 and E2 located 525 and 433 kb 5′ of the *MYC* promoter in MCL. SMC1 and EBF1 HiChIP arcs displaying normalized significant interactions among promoters and enhancers in Granta519. Bottom track indicates E1, E2 and *MYC* gene location. Top track indicates the 30 steps of ORCA experiments. **b**, Schematic of ORCA experiment procedures at the *MYC* locus in Granta519. **c**, Representative barplots showing the majority of traces have all 30 segment readouts detected in the ORCA experiments of clone 27 (left) and clone 97 (right) in untreated (left), 6 h dTAG treatment (right), 24 h dTAG treatment, 6 h dTAG washout and 24 h dTAG washout conditions (Supplementary Table). Only traces with five or fewer missing barcodes are used in remaining analyses. **d**, Time-course Micro-C interaction frequency maps showing gradual and reproducible (top, clone 27; bottom, clone 97) reduction and recovery of interactions at the *MYC* locus after dTAG treatment and washout. Resolution, 5 kb. Bottom left icon shows sequencing-based data. **e**, Time-course ORCA allele frequency maps showing gradual reduction and recovery of interactions at the *MYC* locus after dTAG treatment and washout. Each condition combines the alleles from clones 27 and 97 and uses the average distance between two consecutive segments as the cutoff for determining interaction. Alleles are not imputed, and missing values are excluded from the calculations. Bottom left, icon shows imaging-based data. **f**, Allele frequency maps of *MYC* locus traces for each of the seven common topological conformations. Clustering and calculation of frequencies are performed on pairwise distance matrices of imputed alleles from all conditions in the two clones. **g**, Example reconstructed chromatin traces for each of the seven common topological conformations of the *MYC* locus. Numbers on the traces indicate the 30 ORCA steps. Source numerical data are available.

were highly correlated and concordantly detected the *MYC* TAD/sub-TAD boundaries and enhancer–promoter loop dots (Fig. 3d,e and Extended Data Fig. 3c,d).

Notably, ORCA average distance and interaction frequency maps revealed more pronounced EBF1-dependent changes in *MYC* locus topology (Fig. 3e and Extended Data Fig. 3c). Time-resolved ORCA experiments showed that a stripe-like feature emanating from the *MYC* promoter to its distal super-enhancers E1 and E2 gradually diminished following EBF1 degradation. This data also revealed that EBF1 removal steadily reduced interactions across the telomeric TAD boundary, separating the *MYC* promoter from its 3′ flanking sequences. Of note, EBF1 restoration progressively reinstated interactions between centromeric and telomeric sub-TADs, re-established the *MYC*-E1/E2 stripe and recovered cross-telomeric TAD boundary interactions. Besides confirming high quality of our ORCA, these data demonstrated that, even at the population level, ORCA provides additional insights into the impact of EBF1 on *MYC* locus topology in MCL.

EBF1 alters the frequency of *MYC* common topological conformations in MCL

Leveraging the single-allele resolution of ORCA, we next asked whether EBF1 instructs a unique chromatin conformation or changes the frequency of existing topological conformations available to *MYC*. Clustering of high-dimensional chromatin traces from all EBF1-FKBP-KI MCL cells identified seven distinct common conformations, each represented by >2,000 traces (Fig. 3f and Extended Data Fig. 3e). These common conformations displayed varying levels of compaction, with the most open and compact traces grouped together in conformations C1 and C7, respectively. We next performed a similar analysis in our time-resolved ORCA experiments to examine the impact of EBF1 on common conformations of the *MYC* locus. While the overall set of *MYC* common conformations remained unchanged (Extended Data Fig. 4a–c), EBF1 removal and restoration rapidly altered the prevalence of traces with certain chromatin conformations (Extended Data Fig. 3e). Collectively, these data revealed that EBF1 does not alter the constellation of topologies available to *MYC* but rather increases the likelihood of conformations that favour *MYC* interaction with its distal enhancers, resulting in pronounced EBF1-dependent differences in population-average interaction frequency maps.

To complement this analysis, we inspected features of individual alleles using Optical Looping Interactive Viewing Engine (OLIVE), our interactive portal for qualitative and quantitative study of chromatin traces[67]. Despite being located at opposite ends of the locus on the linear genome (Fig. 3a), the *MYC* promoter and its two super-enhancers tended to localize near the local spatial centres of chromatin traces exhibiting conformations permissive to promoter–enhancer interactions (Fig. 3g). Intrigued by this observation, we calculated the geometric centre of each chromatin trace and measured the distance of each segment from this centre to assess its connectivity relative to other regions of the chromatin fibre (Methods). Consistent with visual observations, traces with different common conformations displayed distinct local radial patterns (Extended Data Fig. 3f). Notably, the *MYC* promoter was generally positioned closer to the local geometric centre in conformations with higher likelihood of enhancer–promoter interactions, suggesting that the radial positioning of the *MYC* promoter within the locus may influence its capacity to engage distal enhancers.

EBF1 instructs *MYC* multi-enhancer interactions in individual MCL cells

Given EBF1-mediated changes in the frequency of *MYC*'s topological conformations, we examined how EBF1 impacts the heterogeneity of E1 and E2 positioning. Observing a lack of coordination in *MYC* promoter–enhancer interactions between alleles of the same nucleus (Fig. 4a), we first compared the frequency of alleles exhibiting *MYC*-to-E1 interactions to those of distance-matched non-enhancer/promoter pairs across the locus as internal controls (Fig. 4b). This analysis revealed that *MYC* and E1 interacted in 37% of alleles in dTAG-untreated cells. Following EBF1 removal, this frequency significantly decreased and reached to a level comparable with internal controls 24 h post-treatment. Conversely, EBF1 restoration rapidly and significantly increased the frequency of *MYC*-to-E1 interactions within 6 h, restoring levels comparable with dTAG-untreated cells. Similarly, the allele frequency of pairwise *MYC*-to-E2 interactions was 24% in untreated cells, decreased to a level comparable with controls 24 h after EBF1 removal, and rapidly restored within 6 h after dTAG washout (Fig. 4c). These data, consistent with Micro-C results, further demonstrate that EBF1 binding to *MYC* super-enhancers reduces *MYC* promoter–enhancer spatial proximity in individual MCL chromatin fibres.

To examine whether multi-enhancer–promoter interactions are present in individual chromatin fibres, we quantified the frequency of alleles with only pairwise *MYC*-to-E1, *MYC*-to-E2 or three-way *MYC*–E1–E2 interactions. *MYC*–E1–E2 simultaneous interactions were reproducibly observed in 12% of alleles (Fig. 4d and Extended Data Fig. 3g). Although relatively rare, *MYC*–E1–E2 interactions were twice as frequent as expected from distance-matched non-enhancer/promoter element triplets. Bootstrapping analysis further substantiated the significance of this observation (Fig. 4e).

We next compared the frequency of alleles with *MYC*–E1–E2 interactions in our time-resolved ORCA (Fig. 4d,e and Extended Data Fig. 3g). EBF1 loss gradually reduced the occurrence of *MYC*–E1–E2 three-way

Fig. 4 | The *MYC* promoter and enhancers interact at the local geometric centres in MCL. a, Distances between *MYC* promoter, E1 and E2 significantly increase and decrease after dTAG treatment and washout, respectively. Two representative nuclei per condition are shown with fiducial and magnified images for *MYC*–E1–E2, *MYC*–E1, *MYC*–E2 and E1–E2. To distinguish the steps imaged with Alexa647 sequentially, E1, E2 and *MYC* are pseudo-coloured as cyan, magenta and yellow, and fiducial using Cy3 is pseudo-coloured as green. Scale bars, 1 µm. Scale bars on zoomed-in images represent 250 nm. **b**, Barplots of allele frequencies with E1 (step 7 or 8) and *MYC* (step 25) interactions compared with the distance-matched pairs using a sliding window (Methods). Bootstrapping is performed per condition by sampling 500 alleles 1,000 times and error bars show 95% CIs. **c**, Same as **b** for E2 (step 11) and *MYC* (step 25). **d**, Barplots showing fraction of alleles with *MYC*–E1–E2, only *MYC*–E1, only *MYC*–E2 or no *MYC* promoter–enhancer interaction (neither) per condition. Control regions are defined in Methods. **e**, Box-and-whisker and violin plots showing decrease and recovery of allele frequency with *MYC*–E1–E2, only *MYC*–E1 and only *MYC*–E2 interactions after dTAG treatment and washout. Each point represents the allele frequencies calculated from 500 randomly sample alleles with a total of 1,000 rounds of random sampling per condition. Box-and-whisker plots show, centre line, median; box limits, upper (75th) and lower (25th) percentiles; whiskers, 1.5 × interquartile range. FWER-adjusted *P* values obtained by a two-sided Wilcoxon rank-sum test. **f**, Definition of geometric centre and radius of gyration. **g**, Box-and-whisker plots showing distribution of radius of gyration of alleles with *MYC*–E1–E2, only *MYC*–E1, only *MYC*–E2 or no *MYC* promoter–enhancer interaction (neither) in untreated MCL. The number of alleles in each category is indicated in parenthesis. Box-and-whisker plots are described in **e**. FWER-adjusted *P* values obtained by a two-sided Wilcoxon rank-sum test. **h**, Distances of each segment to the geometric centres of chromatin traces with *MYC*–E1–E2, only *MYC*–E1, only *MYC*–E2 or no *MYC* promoter–enhancer interactions (neither). The median values of stratified alleles are calculated and plotted for each ORCA segment in untreated cells. Each point represents the median centrality calculated from 500 randomly sample alleles with a total of 1,000 rounds of random sampling. Error bars show 95% CI from bootstrapping. **i**, Example reconstructed chromatin traces for alleles with *MYC*–E1–E2 three-way interaction, *MYC*–E1 interaction, *MYC*–E2 interaction and no interaction emphasizing the central positioning of interacting elements. Rg, radius of gyration. Source numerical data are available.

https://doi.org/10.1038/s41556-025-01827-2

interactions across individual alleles to a level comparable with distance-matched internal controls. Conversely, EBF1 restoration rapidly and significantly increased the frequency of multi-enhancer–promoter interactions to a level comparable with dTAG-untreated cells within 6 h. Notably, we observed differences in both the magnitude and kinetics of recovery: three-way *MYC*–E1–E2 interactions recovered more rapidly and frequently than pairwise interactions (Fig. 4e). In summary, our findings demonstrate that beyond promoting pairwise enhancer–promoter interactions in individual MCL cells, EBF1 contributes to the maintenance and establishment of multi-enhancer interactions, an EBF1-preferred topological conformation that enables rapid *MYC* induction.

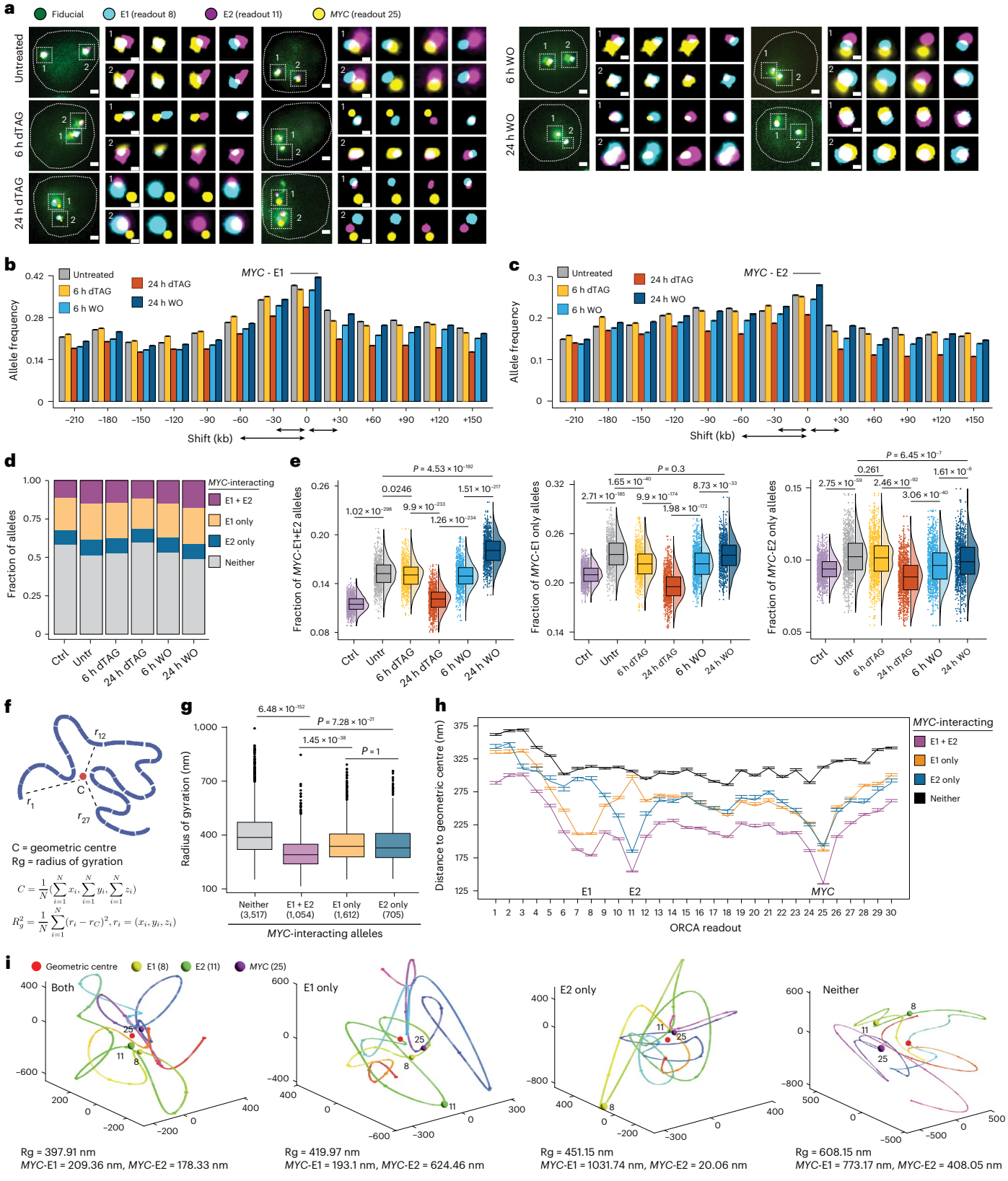

$$C = \frac{1}{N}\left(\sum_{i=1}^{N} x_i, \sum_{i=1}^{N} y_i, \sum_{i=1}^{N} z_i\right)$$

$$R_g^2 = \frac{1}{N}\sum_{i=1}^{N}(r_i - r_C)^2, r_i = (x_i, y_i, z_i)$$

The *MYC* promoter and enhancers interact at the local spatial centres in MCL

Our single-allele-resolution data revealed that EBF1 orchestrates multi-enhancer interactions to regulate *MYC* expression in MCL. However, the mechanisms by which chromatin fibre folding at the level of individual alleles enables multi-enhancer gene regulation, and whether lineage-determining TFs coordinate locus-wide folding of chromatin fibres and multi-enhancer interactions remain unclear.

Considering the observed correlation between the *MYC* promoter's local radial positioning and the favourability of locus conformation for enhancer–promoter interactions (Extended Data Fig. 3f), we hypothesized that local centring of the *MYC* promoter and its enhancers influences their multiway interactions. The radius of gyration, a metric of chromatin fibre compaction, indicated that traces containing *MYC* multi-enhancer interactions were significantly more compact than those with only *MYC*-to-E1, only *MYC*-to-E2 or no *MYC* promoter–enhancer interactions (Fig. 4f,g and Extended Data Fig. 4d). Notably, despite being located at the opposite ends of the locus on the linear genome, *MYC*, E1 and E2 were positioned closer to the geometric centre in traces featuring multi-enhancer interactions (Fig. 4h,i and Extended Data Fig. 4d). By contrast, segments of chromatin traces with no enhancer–promoter interactions exhibited uniformly larger distances from the locus centre. Of note, E1 and E2 were separated from the centre in traces with only *MYC*-to-E2 and only *MYC*-to-E1 interactions, respectively. Similar patterns persisted following EBF1 degradation and restoration, despite changes in allele frequencies of MYC-to-E1/E2 interactions (Extended Data Fig. 4e–h). Collectively, these findings suggest that EBF1 contributes to the local radial positioning of enhancers to facilitate multi-enhancer–promoter interactions in individual MCL cells.

EBF1 selectively impacts cohesin distribution on MCL chromatin

The interplay between EBF1 and the central positioning of enhancers at the *MYC* locus prompted us to examine how EBF1 influences chromatin occupancy of CTCF, YY1 and cohesin, factors known to facilitate enhancer–promoter interactions[68–70]. In contrast with CTCF and YY1, changes in SMC1 and EBF1 occupancy correlated following dTAG treatment and washout (Fig. 5a and Extended Data Fig. 5a). Consistent with the observation that EBF1 has a greater impact on looping in gene-sparse than gene-dense hubs, we further observed markedly greater changes in SMC1 loading at these loci (Figs. 2g–i and 5b and Extended Data Figs. 2g and 5b). As SMC1 levels remained invariant after EBF1 modulation (Fig. 5c), these data collectively suggest that EBF1 impacts the distribution of cohesin on chromatin, with more pronounced effects at gene-sparse hubs.

EBF1 positions enhancers to the spatial centre of *MYC* locus by constraining cohesin traffic in MCL

Considerable evidence supports the role of cohesin in shaping genome topology through the loop-extrusion model[71–73]. After loading onto chromatin, cohesin complexes dynamically extrude chromatin until they are unloaded, or their movement is blocked or paused by extrusion barriers such as CTCF. To gain a more mechanistic understanding of the interplay between EBF1, cohesin and enhancer positioning in MCL, we conducted an in-depth analysis of SMC1 chromatin occupancy at bona fide EBF1-bound elements (Fig. 1d). In contrast with CTCF, high SMC1 levels were detectable at sites with broad EBF1 occupancy (Extended Data Fig. 5c). Notably, EBF1 loss led to significantly greater decreases in SMC1 occupancy at the broad EBF1-bound elements, exemplified by *NEK2*, *UST* and *MYC* loci, where changes in EBF1 markedly altered SMC1 levels, but not CTCF, both at the EBF1-bound elements and their immediate flanking sequences, an observation that was generalizable genome-wide (Fig. 5d and Extended Data Fig. 5d–g). Collectively, these data reinforce our earlier finding that SMC1 occupancy is EBF1-dependent (Fig. 5a) and further suggest a potential role for EBF1 in influencing cohesin movement on chromatin, leading to cohesin accumulation at and near EBF1-bound elements.

We next sought to unify these observations and determine how EBF1-mediated cohesin redistribution contributes to enhancer positioning by considering two hypotheses. EBF1 may increase the loading of cohesin onto chromatin, thereby facilitates extrusion of EBF1-bound enhancers towards promoters. Alternatively, EBF1 might impede cohesin movement along the chromosome, which could also account for the cohesin enrichment at and near EBF1-bound sites and increases in the frequency of alleles with enhancer–promoter interactions (Fig. 5d and Extended Data Fig. 5e,f).

To distinguish between these two hypotheses, we leveraged our ORCA data together with physical polymer modelling. Aside from two strong extrusion barriers corresponding to the centromeric and telomeric CTCF-bound TAD boundaries, we differentiated the two models based on EBF1's influence on loop-extruding factor (LEF) loading and movement parameters (Fig. 5e, Extended Data Fig. 5h and Supplementary Table). In the first model, consistent with EBF1 acting

Fig. 5 | EBF1 positions enhancers to the *MYC* locus geometric centres by constraining cohesin traffic. a, Box-and-whisker plots showing differential SMC1 ChIP-seq signals in 6 h dTAG treatment (left) and washout (right) per quartile (Q1, $n = 3{,}765$; Q2, $n = 3{,}573$; Q3, $n = 4{,}143$; Q4, $n = 5{,}001$) of EBF1 loading changes 6 h after dTAG treatment. Box-and-whisker plots show centre line, median; box limits, upper (75th) and lower (25th) percentiles; whiskers, 1.5 × interquartile range. *P* values obtained by a two-sided Wilcoxon rank-sum test. **b**, Box-and-whisker and violin plots comparing differential SMC1 ChIP-seq signals in 6 h dTAG treatment (left) and washout (right) at SMC1 peaks located in gene-sparse and gene-dense hubs. The number of hubs in each group is listed in parentheses. Box-and-whisker plots are described in **a**. *P* values obtained by a two-sided Wilcoxon rank-sum test. **c**, Time-course western blotting of SMC1 and EBF1 in Granta519-EBF1-FKBP-KI clone 27 showing SMC1 protein is invariant to EBF1 removal and restoration. β-Actin is the loading control. **d**, ChIP-seq tracks showing EBF1, SMC1, CTCF and YY1 signals in MCL at the *MYC* super-enhancers E1 and E2 centred around EBF1-binding sites and the *MYC* gene body. Note concordant changes in SMC1 and EBF1 levels at the EBF1-bound sites after dTAG treatment and washout. **e**,**f**, Allele frequency maps for simulated *MYC* locus polymers in EBF1 wild-type (**e**) and EBF1-degraded (perturbed) (**f**) conditions. Allele frequencies are calculated using 10 as the cutoff for interaction between two monomers. The frequency of pairwise interactions between 900 monomers is equivalent to a 1-kb genomic resolution (top rows), and the median of pairwise interaction frequencies of each 30 monomers is equivalent to a 30-kb resolution (bottom). See Methods for the parameters distinguishing EBF1 as an extruder loader (left column) or barrier (right column). Top left icon, simulation-based data. **g**, Barplots of allele frequencies of monomers representing E1 (left), E2 (right) and *MYC* compared with the distance-matched pairs using a sliding window (Methods). Error bars show s.d. of allele frequency calculated from 1,000 randomly sampled polymers in 1,000 iterations. **h**, Box-and-whisker and violin plots showing the decrease of *MYC*–E1–E2 interaction frequencies in perturbed *MYC* locus. Each point represents the allele frequencies calculated from 1,000 randomly sample polymers with a total of 1,000 iterations per condition. Control regions are shifted 60 monomers to the left of *MYC*, E1 and E2 monomers. Box-and-whisker plots are described in **a**. *P* values obtained by a two-sided Wilcoxon rank-sum test. **i**, Box-and-whisker plots showing distribution of radius of gyration of simulated polymers with *MYC* interacting with E1, E2, both or neither in wild-type scenario. The number of polymers in each category is indicated in parentheses. Box-and-whisker plots are described in **a**. FWER-adjusted *P* values obtained by a two-sided Wilcoxon rank-sum test. **j**, Distances of each monomer to the geometric centres of the polymers with *MYC* interacting with E1, E2, both or neither. The median values and s.d. across stratified polymers are calculated and plotted for each of the 900 monomers in the wild-type scenario. The number of simulated polymers in each category is the same as **i**. Each point represents the median centrality calculated from 1,000 randomly sample alleles with a total of 1,000 rounds of random sampling per condition. Error bars show 95% CI from bootstrapping. Source numerical data and unprocessed blots are available.

https://doi.org/10.1038/s41556-025-01827-2

as a facilitator of cohesin loading, LEFs preferentially loaded at polymer regions corresponding to EBF1-enriched elements. In the second model, the EBF1-enriched elements determined both the span and the blocking ability of TAD-internal permeable barriers that impeded the movement of uniformly loaded LEFs along the polymers.

Both models, assuming identical density and lifetime of LEFs, produced population-level features reminiscent of architectural stripes, loop dots and TAD boundaries (Figs. 3e and 5e,f and Extended Data Fig. 5h). However, the loading model resulted in unusually strong jet-like interactions near the EBF1-binding sites and further diverged from the Micro-C by predicting stronger *MYC*-to-E1, *MYC*-to-E2, intra-TAD loop dots and non-uniform intra-TAD interactions. Conversely, the permeable barrier model more faithfully recapitulated the diverse population-level features observed by Micro-C and

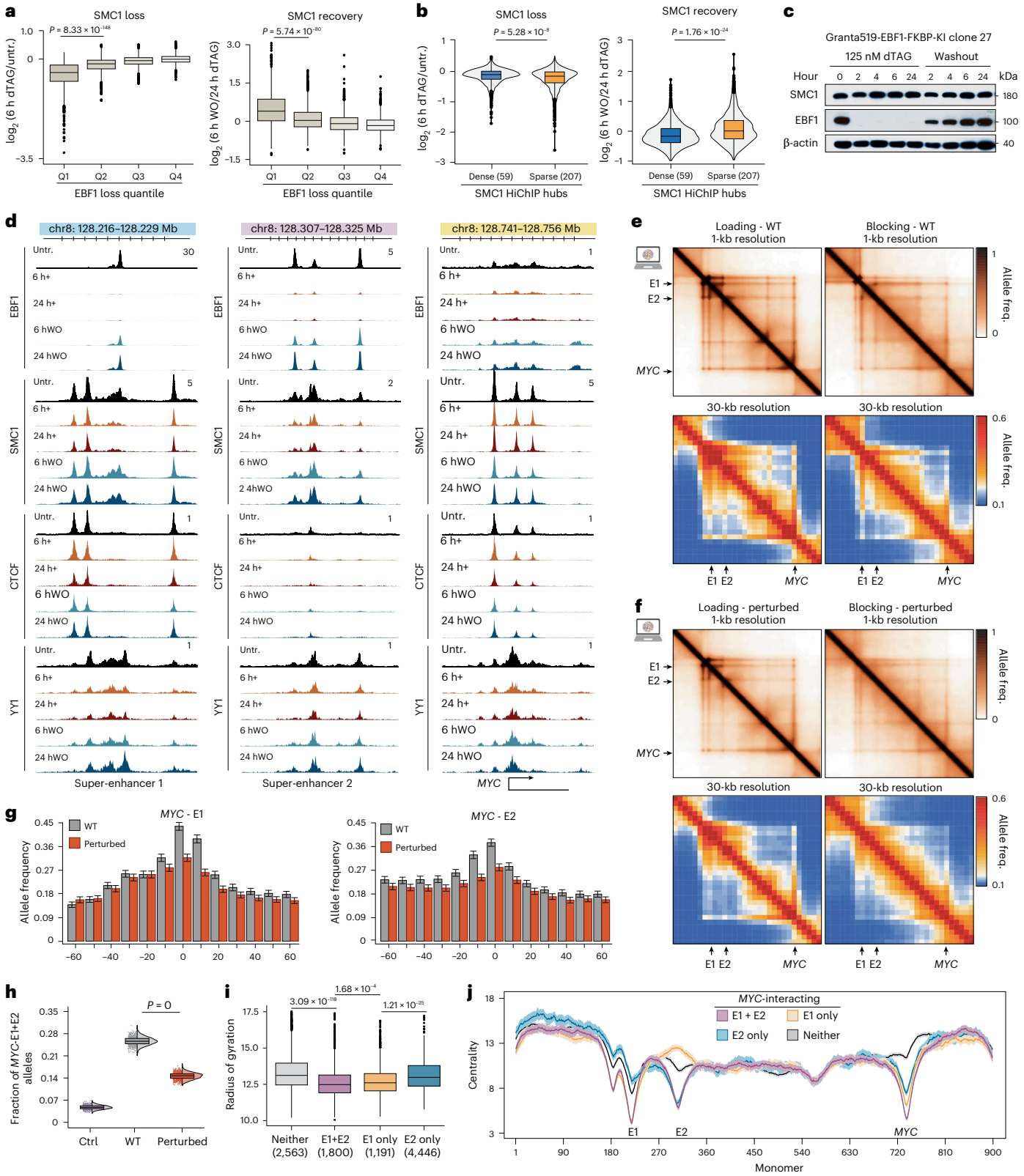

population-average ORCA interaction maps, including *MYC*-to-E1 and *MYC*-to-E2 loop dot differences, uniformly distributed intra-TAD interactions and the absence of unusual jet-like interactions near the diagonals of the interaction maps.

We further examined how the two plausible mechanisms could account for EBF1's effect on population-average pairwise interactions (Figs. 3e and 5e,f and Extended Data Fig. 5h). The loading model predicted a complete loss of intra-TAD structure, accompanied by persistent chromatin-jet-like interactions near cohesin loading sites (features not observed in sequencing or imaging of the *MYC* locus after EBF1 loss). In contrast, the permeable barrier model accurately reproduced the observed reductions in *MYC*-to-E2 loops compared with *MYC*-to-E1, as well as effects of EBF1 loss on intra-TAD interactions seen in Micro-C and ORCA data.

We next quantitatively compared frequency of alleles with pairwise and multi-enhancer–promoter interactions observed in experimental and synthetic chromatin fibres (Figs. 4d–h and 5g–j and Extended Data Fig. 5i). The permeable barrier model more accurately predicted the frequencies of these interactions and captured their reduction following EBF1 loss. Polymers lacking *MYC*-to-E1 or *MYC*-to-E2 interactions exhibited displacement of the E1 or E2 regions from their local geometric centres, respectively. Those with *MYC*–E1–E2 three-way interactions were more compact, with the promoter and two enhancer segments positioned closer to their geometric centres.

Further support for EBF1 functioning as a permeable barrier to cohesin movement came from examining the insulation potential of EBF1-bound sites using Micro-C data (Extended Data Fig. 5j,k). Compared with their flanking sequences, EBF1-bound elements exhibited higher insulation potential, which was markedly reduced upon EBF1 loss, without affecting insulation at other accessible elements, including CTCF-bound elements. This analysis complements our polymer modelling studies, and together demonstrate that a constrained loop-extrusion mechanism best explains both population- and single-allele-level experimental observations. These findings suggest that EBF1-mediated modulation of cohesin traffic patterns at the *MYC* locus constrains enhancer positioning, thereby organizing *MYC* multi-enhancer interactions in MCL.

EBF1 binds and activates *KLF7* promoter without changing its local radial positioning in GSI-resistant T-ALL

To investigate the generalizability of our findings, we next studied T-ALL, where EBF1 de-repression is required for resistance to γ-secretase inhibitor (GSI), a Notch signalling antagonist[74]. During long-term EBF1 de-repression, >100 loci switched from transcriptionally inactive B to active A compartment, including *KLF7*, a T cell-proliferation regulator[74–76] (Extended Data Fig. 6a). Concordantly, GSI-resistant cells exhibited high expression of *KLF7*, whereas the gene was inactive in GSI-sensitive cells. Notably, analyses of H3K27ac and EBF1 chromatin occupancy revealed prominent gains in chromatin activity and EBF1 binding exclusively at the *KLF7* gene body, with no significant changes at any distal element. We thus leveraged the *KLF7* locus to investigate whether gene activation alone is sufficient for central positioning.

Hi-C and Micro-C showed reproducible increases in population-average interaction frequencies and TAD boundaries' insulations across the *KLF7* locus in GSI-resistant cells. These observations were corroborated by our 37-step ORCA experiments, which used 8,128 primary oligonucleotides to image ~11,000 *KLF7* alleles (Extended Data Fig. 6a–c and Supplementary Table). Single-allele-resolution studies further revealed notable compaction and decreased pairwise distances between most segments within the *KLF7* locus in GSI resistance (Extended Data Fig. 6b–e and Supplementary Table). Examination of local radial positioning showed central placement of the 3′ TAD boundary (step 31) and several elements co-bound by CTCF and SMC1 in GSI-sensitive cells (Extended Data Fig. 6f,g). In GSI-resistant cells, similar analyses showed the central positioning of elements with a concurrent increase of CTCF and SMC1 binding, potentially facilitating the multiple stripe-like features observed in the population-average interaction map of these cells. Despite being near the locus's midpoint on the linear genome, the local radial positioning of the *KLF7* promoter remained unchanged in GSI resistance. Collectively, *KLF7* chromatin tracing suggests that gene activation is not sufficient to drive the central positioning of distal regulatory elements.

EBF1 positions *ZEB2* and its enhancer to local spatial centre to enable their interactions in GSI-resistant T-ALL

T-ALL-associated TF *ZEB2* (ref.77) was de-repressed with a B-to-A compartment shift in GSI resistance (Fig. 6a). Unlike *KLF7*, EBF1 bound to and activated a GSI-resistance-restricted enhancer ~200 kb 5′ of *ZEB2*. We observed the formation of a stripe between the EBF1-bound enhancer and *ZEB2*, but not *GTDC1*, which was already expressed in GSI-sensitive cells (Fig. 6a–c). This allowed us to investigate whether EBF1-dependent distal enhancer activation alters local radial positioning of enhancers and promoters.

A 30-step chromatin tracing of the *ZEB2* locus with 5,912 primary oligonucleotide probes showed marked increases in average interaction frequencies, reductions in pairwise spatial distances and

Fig. 6 | EBF1 positions the *ZEB2* promoter and enhancer towards the local geometric centres in GSI-resistant T-ALL. a, ChIP-seq tracks showing the gain of active histone marks H3K27ac, EBF1, CTCF and SMC1 at the *ZEB2* locus in GSI-resistant DND41. Normalized SMC1 HiChIP arches showing gain of interactions in GSI-resistant DND41. The PC1 values of Hi-C contact correlation matrices in GSI-sensitive and GSI-resistant cells showing shift from the B (<0) to A (>0) compartment. Rainbow-coloured bars indicate the 30 steps of the ORCA experiments. Bottom track indicates the positions of expressed genes. **b**, Normalized Micro-C (top) and Hi-C (bottom) interaction frequency maps showing gain of interactions in GSI-resistant (right) compared with GSI-sensitive (left) at the *ZEB2* locus in GSI-sensitive versus GSI-resistant DND41. **c**, Differential (GSI-resistant minus GSI-sensitive) normalized Micro-C interaction maps with 30-kb resolution matching ORCA showing gain of stripe between the *ZEB2* promoter and enhancer in GSI-resistant DND41. **d**, ORCA pairwise distance maps of *ZEB2* chromatin traces in GSI-sensitive (left) and GSI-resistant (right) DND41. Each point represents the median of pairwise distances between two segments across all alleles. Alleles are not imputed, and missing values are excluded from the calculation. **e**, Cumulative distribution of radius of gyration of *ZEB2* chromatin traces in GSI-sensitive and GSI-resistant DND41 showing overall compaction of *ZEB2* locus in GSI-resistant cells. *P* value obtained by a two-sided Kolmogorov–Smirnov test. **f**, Distances of each segment to the geometric centres of the chromatin traces of *ZEB2* locus in GSI-sensitive and GSI-resistant DND41. The median values of chromatin traces are calculated and plotted for each ORCA segment in GSI-sensitive and GSI-resistant cells. Note that *ZEB2* promoter (step 14) but not *GTDC1* (step 8) is positioned the closest to geometric centres of alleles in GSI resistance. The number of alleles in each condition is indicated in parentheses. Error bars show 95% CI from bootstrapping. **g**, Barplots of allele frequencies with *ZEB2* promoter–enhancer interactions (steps 14 and 20) in GSI-sensitive and GSI-resistant DND41 compared with the distance-matched pairs using a sliding window (Methods). Cutoff for interaction, 250 nm. Bootstrapping of 500 randomly sampled alleles with a total of 1,000 rounds of random sampling per condition and error bars show 95% CIs. **h**,**i**, Allele frequency maps of chromatin traces for each of the five common topological conformations of the *ZEB2* locus in GSI-sensitive (**h**) and GSI-resistant (**i**) DND41. Clustering and calculation of frequencies are separately performed on pairwise distance matrices of alleles from each condition. **j**, Distances of each segment to the geometric centres of chromatin traces with or without *ZEB2* promoter–enhancer interactions in GSI-resistant DND41. The median values of stratified alleles are calculated and plotted for each ORCA segment. The number of alleles is indicated in parentheses. Error bars show 95% CI from bootstrapping. **k**, Example reconstructed chromatin traces for alleles in GSI-resistant DND41 with (left) and without (right) *ZEB2* enhancer–promoter interaction emphasizing the central positioning of interacting elements. Source numerical data are available.

https://doi.org/10.1038/s41556-025-01827-2

substantial locus compaction in GSI-resistant cells (Fig. 6a–e and Supplementary Table). Despite these similarities, the *KLF7* and *ZEB2* loci exhibited distinct changes in local radial positioning. While the centrality of the *KLF7* promoter remained unchanged, the *ZEB2* promoter became the closest segment to the local geometric centre in GSI resistance (Fig. 6f).

Notably, the *ZEB2* promoter and its EBF1-bound enhancer (step 20) exhibited the highest increase in interaction frequency compared with distance-matched internal controls, potentially facilitated by the formation of common topological conformations permissive to promoter–enhancer interactions (Fig. 6g–i). Notably, the *ZEB2* promoter and its EBF1-bound enhancer were positioned markedly closer to the local geometric centre only in traces exhibiting enhancer–promoter interactions (Fig. 6j,k). Together, our single-allele-resolution studies of *ZEB2* and *KLF7* in GSI-resistant T-ALL support our observations in MCL and demonstrate that gene activation alone is insufficient; rather

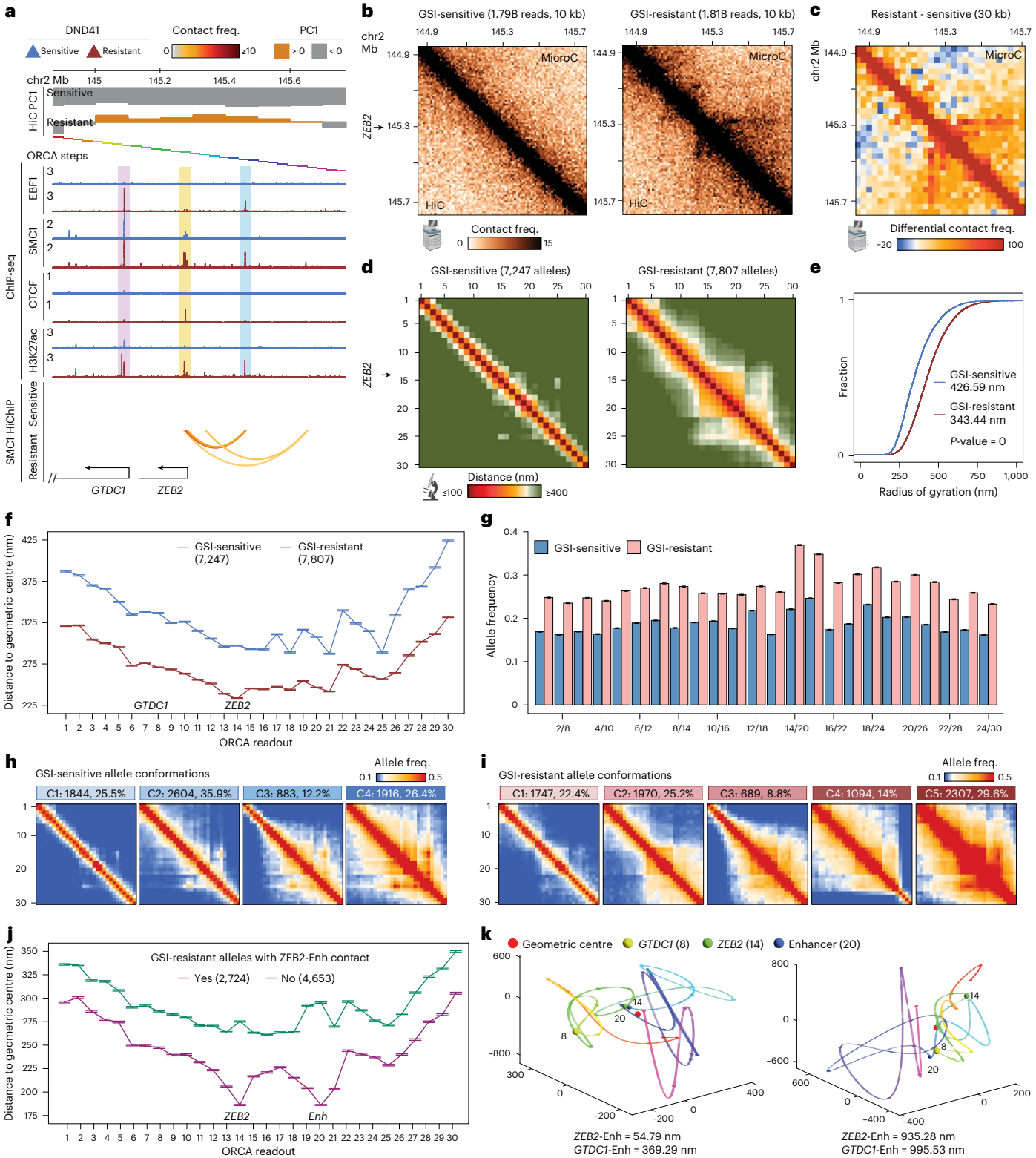

https://doi.org/10.1038/s41556-025-01827-2

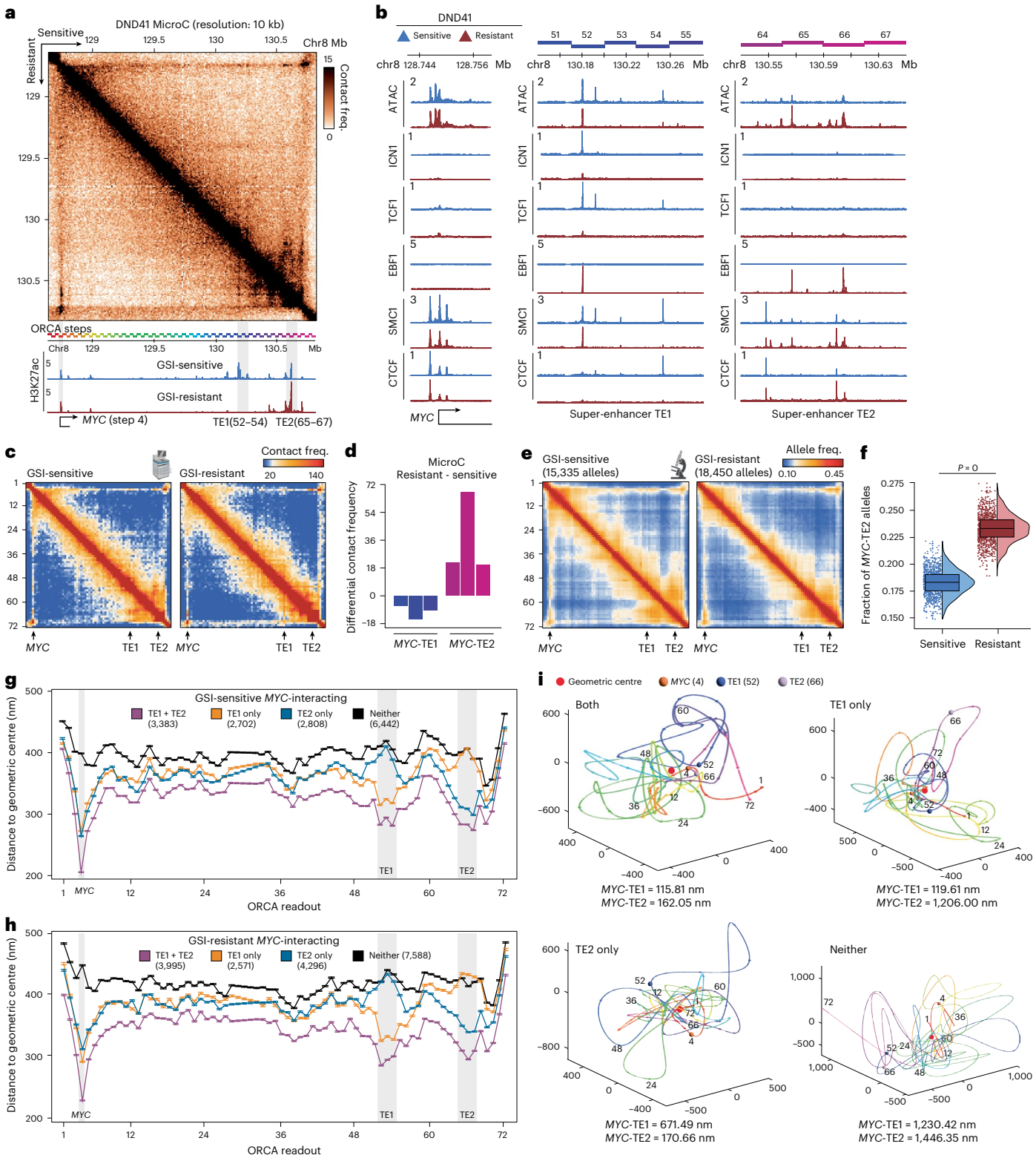

EBF1-dependent distal enhancer activation is required for central positioning of regulatory elements.

EBF1-mediated cohesin redistribution in MCL is also observed in GSI-resistant T-ALL

We next examined whether the EBF1-mediated changes in cohesin traffic pattern observed in MCL were also generalizable to T-ALL. Like MCL, we observed significant increases in chromatin accessibility and SMC1 occupancy, but not CTCF, at 78.5% of GSI-resistant EBF1-bound elements. These changes exhibited distinct patterns of EBF1 and SMC1 co-occupancy, exemplified by *ZNF195* and *GADD45B* loci (Extended Data Fig. 6h–j). Consistent with findings in MCL, elements co-occupied by CTCF and EBF1 showed the smallest increases, whereas broad EBF1-bound elements lacking CTCF displayed the highest gain of SMC1 in GSI resistance. Additionally, EBF1-bound elements exhibited stronger insulation potential compared with their flanking sequences

Fig. 7 | Two *MYC* distal super-enhancers interact with the promoter near local geometric centres in GSI-sensitive and GSI-resistant DND41. a, Normalized Micro-C interaction maps at 10-kb resolution in GSI-sensitive (top) and GSI-resistant (bottom) DND41. H3K27ac ChIP-seq tracks showing two super-enhancers TE1 and TE2 located more than 1.5 Mb 3′ of the *MYC* promoter in GSI-sensitive DND41 (bottom). Note the loss of TE1 and increase in TE2 activity in GSI-resistant DND41. Rainbow-coloured bars indicate the 72 steps of the ORCA experiments. **b**, ATAC-seq and ChIP-seq genome tracks showing invariant accessibility, SMC1 and CTCF levels at the *MYC* promoter in GSI-sensitive and GSI-resistant DND41. In contrast, intracellular NOTCH1 (ICN1)/TCF1-bound super-enhancer TE1 lost most of its accessible elements, as well as SMC1 and CTCF binding, whereas super-enhancer TE2 gained EBF1, SMC1 and CTCF binding and accessibility at several elements. Coloured bars on the top indicate the coverage of ORCA steps. **c**, Normalized Micro-C interaction frequency maps in GSI-sensitive (left) and GSI-resistant (right) DND41 at 30-kb resolution matching ORCA steps showing a stripe-like feature connecting the *MYC* promoter and the two distal super-enhancers. **d**, Quantification of Micro-C normalized interaction frequencies between the *MYC* promoter (bin number 4) and TE1 (bin numbers 52–54) or TE2 (bin numbers 65–67) in GSI-sensitive and GSI-resistant DND41. **e**, Allele frequency maps for GSI-sensitive (left) and GSI-resistant (right) DND41 *MYC* chromatin traces from two biological replicates per condition. Each condition uses the average distance between two consecutive segments as the cutoff for determining interaction. Alleles are not imputed, and missing values are excluded from the calculation of frequencies. **f**, Box-and-whisker and violin plots showing increase in allele frequency with only *MYC*–TE2 interaction in GSI-resistant DND41. Each point represents the allele frequencies calculated from 1,000 randomly sampled alleles with a total of 1,000 rounds of random sampling per condition. Box-and-whisker plots show centre line, median; box limits, upper (75th) and lower (25th) percentiles; whiskers, 1.5 × interquartile range. FWER-adjusted *P* value obtained by a two-sided Wilcoxon rank-sum test. **g**,**h**, Distances of each segment to the geometric centres of chromatin traces with *MYC*–TE1–TE2, only *MYC*–TE1, only *MYC*–TE2 or no *MYC* promoter–enhancer interactions (neither) in GSI-sensitive (**g**) and GSI-resistant (**h**) DND41. The median values of stratified alleles are calculated and plotted for each ORCA segment in untreated cells. The number of alleles in each category is indicated in parentheses. Error bars show 95% CI from bootstrapping. **i**, Example reconstructed chromatin traces for alleles with *MYC*–TE1–TE2 three-way interaction or only *MYC*–TE1 interaction from GSI-sensitive DND41, and only *MYC*–TE2 interaction or no promoter–enhancer interactions (neither) from GSI-resistant DND41 emphasizing the central positioning of interacting elements. Source numerical data are available.

(Extended Data Fig. 6k). Together, these data suggest that parallel to MCL, gain of EBF1 binding during GSI-resistance acquisition alters the cohesin traffic pattern in T-ALL.

The *MYC* promoter and enhancers interact at the local spatial centres in individual GSI-sensitive and GSI-resistant T-ALL cells

Observing EBF1's effect on enhancer local central positioning in MCL and GSI-resistant T-ALL, we next asked whether T cell-linage-determining TFs, including TCF1 (ref. 12), influence enhancer local radial positioning in GSI-sensitive T-ALL. In this context, EBF1 is not expressed and two super-enhancers TE1 and TE2, located 1.35 Mb and 1.85 Mb 3′ of the promoter, interact with *MYC* (Fig. 7a and Extended Data Fig. 8a)[74].

Previously, we demonstrated that differential TE1 and TE2 activity is the epigenetic mechanism of *MYC* reactivation in GSI resistance[74]. In GSI-sensitive cells, examination of TE1 identified three TCF1-bound accessible elements. While all three elements were deacetylated in GSI resistance, one remained accessible, SMC1-bound, and *MYC* interactive (albeit at a lower frequency) potentially due to replacement of TCF1 with EBF1 (Fig. 7a–d). Similarly, examination of TE2 in GSI-sensitive T-ALL revealed several highly acetylated and accessible elements unbound by EBF1/TCF1, which may be regulated by other TFs. Unlike TE1, several elements in TE2 concomitantly gained accessibility, acetylation, SMC1 and EBF1 binding, and *MYC* interaction in GSI-resistant cells (Fig. 7a–d). Collectively, these findings suggest that differential binding of lineage-determining TFs alters the activity, cohesin occupancy, and positional dynamics of the two T-ALL-restricted *MYC* super-enhancers during GSI-resistance acquisition.

We next sought to investigate the impact of TF binding on the positioning of TE1 and TE2 by tracing 15,335 GSI-sensitive and 18,450 GSI-resistant *MYC* chromatin fibres using highly reproducible, stable and efficient 72-step ORCA (Fig. 7a–e, Extended Data Fig. 7a–d and Supplementary Table). In GSI-resistant cells, the *MYC* promoter was closer to TE2 but separated from TE1 (Extended Data Fig. 7e). Concordantly, *MYC*-to-TE1-only and *MYC*-to-TE2-only allele frequencies reproducibly decreased and increased in GSI resistance, respectively (Fig. 7f and Extended Data Figs. 7f,g and 8b–e). Similar to observations in MCL, three-way interactions among *MYC*, TE1 and TE2 were present in T-ALL, but became less frequent in GSI-resistant cells, where TE1 was inactive.

Our studies in GSI-sensitive and GSI-resistant T-ALL further showed that traces containing *MYC*–TE1–TE2 interactions were markedly more compact than the other chromatin fibres (Extended Data Fig. 7h). Notably, despite being at the two ends of an ~2-Mb locus, TE1, TE2 and the *MYC* promoter spatially positioned toward local geometric centres to interact (Fig. 7g,i and Extended Data Fig. 7i). Of note, a non-acetylated EBF1-bound element within TE1 exhibited high SMC1 binding and was the closest segment to the local geometric centres in GSI-resistant traces (Fig. 7a,b,h). Collectively, these results confirm our findings in MCL and suggest that the local radial positioning of enhancers may be a general mechanism leveraged by lineage-determining factors EBF1 and TCF1 to facilitate multiway interactions among genomic elements regardless of their activity.

Intrigued by the impact of EBF1 and TCF1 on *MYC* enhancer positioning in MCL and T-ALL, we next designed comprehensive polymer simulations to systematically examine how different regiments of LEF loading (targeted versus uniform) and barrier permeability shape TF-bound element positioning and their surroundings (Extended Data Fig. 9a–e). In the absence of targeted loading, decreasing barrier permeability drew TF-bound elements closer to local geometric centres. Conversely, targeted loading without barriers displaced elements away from the geometric centres. This separation was neutralized when strong barriers were placed at the LEF loading sites. Collectively, these locus- and TF-agnostic studies complement our locus-specific data in MCL and T-ALL, suggesting that TFs beyond EBF1 and TCF1 may constrain cohesin movement to facilitate multi-enhancer–promoter interactions (Extended Data Fig. 8f).

Discussion

The prevalence and mechanisms by which multiple enhancers regulate a single target gene have long intrigued biologists[9,10,78–81]. In this study, we utilized rapid degradation of EBF1 in MCL as a model to investigate direct role of lineage-determining TFs in chromatin folding and multiway enhancer–promoter interactions. Our time-resolved chromatin tracing showed heterogeneous positioning of EBF1-bound enhancers in enhancer–promoter hubs and their dynamic responses to EBF1 modulation. We found that when alleles form enhancer–promoter interactions, EBF1 positions these elements at their local geometric centres. We extended these findings to drug-resistant T-ALL and TCF1, revealing a general mechanism by which lineage-determining TFs facilitate interactions of regulatory elements in nuclear space.

Lineage-determining TFs can open thousands of chromatin sites during development[12,42–44,82,83]. The long-term activity of such factors, including EBF1, can markedly reshape chromatin accessibility landscape during tumourigenesis and drug-resistance development[74,84–88]. In pro-B cells, Ebf1 degradation demonstrated its necessity for maintaining chromatin accessibility[89]. By contrast, our data showed negligible effects on chromatin accessibility after rapid EBF1 degradation in MCL, a cancer of mature B cells. These findings suggest a potential

cell-type-specific requirement for EBF1 in establishing and maintaining chromatin accessibility. Extending this observation to chromatin topology, it is perhaps not surprising that, unlike global reorganization of chromatin architecture driven by long-term EBF1 activity during T-ALL drug resistance, short-term EBF1 changes primarily resulted in invariant TADs and compartments, with only locus-specific alterations in enhancer–promoter interactions within gene-sparse hubs.

Cohesin is enriched at distal enhancers and implicated in enhancer–promoter communication via loop extrusion[35,36,38,40,73]. Given the potential cell-type-specific activity of enhancers, lineage-determining TFs have been suggested to also participate in orchestrating loop extrusion[26,41]. Cohesin can also accumulate at convergently transcribed genes upon depletion of Ctcf and Wapl[71,90]. Polymer simulation studies further linked cohesin with gene promoters by showing that, rather than targeted loaders, RNA polymerases may serve as barriers to extrusion driven by uniformly loaded cohesin (an observation that awaits experimental validation)[71]. Our multipronged studies demonstrated cooperation between EBF1 and SMC1 in multiple systems and further revealed EBF1's role in constraining cohesin movement at distal enhancers. Future studies enabling the simultaneous tracking of 3D genome dynamics of multiple loci, together with lineage-determining TFs and/or cohesin movement in live cells across various systems and loci, will be needed to determine whether additional lineage-determining TFs can directly form chromatin loops, load architectural proteins, obstruct loop extrusion or regulate multiway interactions through other novel mechanisms.

Online content

Any methods, additional references, Nature Portfolio reporting summaries, source data, extended data, supplementary information, acknowledgements, peer review information; details of author contributions and competing interests; and statements of data and code availability are available at https://doi.org/10.1038/s41556-025-01827-2.

References

1. Jin, F. et al. A high-resolution map of the three-dimensional chromatin interactome in human cells. *Nature* **503**, 290–294 (2013).
2. Zhang, Y. et al. Chromatin connectivity maps reveal dynamic promoter-enhancer long-range associations. *Nature* **504**, 306–310 (2013).
3. Ren, B. & Yue, F. Transcriptional enhancers: bridging the genome and phenome. *Cold Spring Harb. Symp. Quant. Biol.* **80**, 17–26 (2015).
4. Maston, G. A., Evans, S. K. & Green, M. R. Transcriptional regulatory elements in the human genome. *Annu. Rev. Genomics Hum. Genet.* **7**, 29–59 (2006).
5. Papantonis, A. & Oudelaar, A. M. Mechanisms of enhancer-mediated gene activation in the context of the 3D genome. *Annu. Rev. Genomics Hum. Genet*. https://doi.org/10.1146/annurev-genom-120423-012301 (2025).
6. Gasperini, M., Tome, J. M. & Shendure, J. Towards a comprehensive catalogue of validated and target-linked human enhancers. *Nat. Rev. Genet.* **21**, 292–310 (2020).
7. Perlman, B. S. et al. Enhancer-promoter hubs organize transcriptional networks promoting oncogenesis and drug resistance. *Nat. Commun.* **15**, 8070 (2024).
8. Schoenfelder, S. & Fraser, P. Long-range enhancer-promoter contacts in gene expression control. *Nat. Rev. Genet.* **20**, 437–455 (2019).
9. Uyehara, C. M. & Apostolou, E. 3D enhancer-promoter interactions and multi-connected hubs: Organizational principles and functional roles. *Cell Rep.* **42**, 112068 (2023).
10. Mumbach, M. R. et al. Enhancer connectome in primary human cells identifies target genes of disease-associated DNA elements. *Nat. Genet.* **49**, 1602–1612 (2017).
11. Furlong, E. E. M. & Levine, M. Developmental enhancers and chromosome topology. *Science* **361**, 1341–1345 (2018).
12. Johnson, J. L. et al. Lineage-determining transcription factor TCF-1 initiates the epigenetic identity of T cells. *Immunity* **48**, 243–57 e10 (2018).
13. Whyte, W. A. et al. Master transcription factors and mediator establish super-enhancers at key cell identity genes. *Cell* **153**, 307–319 (2013).
14. Hnisz, D. et al. Super-enhancers in the control of cell identity and disease. *Cell* **155**, 934–947 (2013).
15. Suva, M. L., Riggi, N. & Bernstein, B. E. Epigenetic reprogramming in cancer. *Science* **339**, 1567–1570 (2013).
16. Spitz, F. & Furlong, E. E. Transcription factors: from enhancer binding to developmental control. *Nat. Rev. Genet.* **13**, 613–626 (2012).
17. Miyazaki, K., Miyazaki, M. & Murre, C. The establishment of B versus T cell identity. *Trends Immunol.* **35**, 205–210 (2014).
18. Stadhouders, R., Filion, G. J. & Graf, T. Transcription factors and 3D genome conformation in cell-fate decisions. *Nature* **569**, 345–354 (2019).
19. Heinz, S. et al. Simple combinations of lineage-determining transcription factors prime cis-regulatory elements required for macrophage and B cell identities. *Mol. Cell.* **38**, 576–589 (2010).
20. Vahedi, G. A. C. P. et al. Helper T-cell identity and evolution of differential transcriptomes and epigenomes. *Immunol. Rev.* **252**, 24–40 (2013).
21. Hsieh, T. H. et al. Mapping nucleosome resolution chromosome folding in yeast by micro-C. *Cell* **162**, 108–119 (2015).
22. Hsieh, T. S. et al. Resolving the 3D Landscape of transcription-linked mammalian chromatin folding. *Mol. Cell.* **78**, 539–53 e8 (2020).
23. Mumbach, M. R. et al. HiChIP: efficient and sensitive analysis of protein-directed genome architecture. *Nat. Methods* **13**, 919–922 (2016).
24. Fasolino, M. et al. Genetic variation in type 1 diabetes reconfigures the 3D chromatin organization of T cells and alters gene expression. *Immunity* **52**, 257–74 e11 (2020).
25. Rao, S. S. et al. A 3D map of the human genome at kilobase resolution reveals principles of chromatin looping. *Cell* **159**, 1665–1680 (2014).
26. Aboreden, N. G. et al. LDB1 establishes multi-enhancer networks to regulate gene expression. *Mol. Cell.* **85**, 376–93 e9 (2025).
27. Petrovic, J. et al. Oncogenic notch promotes long-range regulatory interactions within hyperconnected 3D cliques. *Mol. Cell.* **73**, 1174–90 e12 (2019).
28. Johnstone, S. E. et al. Large-scale topological changes restrain malignant progression in colorectal cancer. *Cell* **182**, 1474–89 e23 (2020).
29. Zhao, J. et al. Oncogenic transcription factors instruct promoter-enhancer hubs in individual triple negative breast cancer cells. *Sci. Adv.* **10**, eadl4043 (2024).
30. Boettiger, A. & Murphy, S. Advances in chromatin imaging at kilobase-scale resolution. *Trends Genet.* **36**, 273–287 (2020).
31. Mateo, L. J., Sinnott-Armstrong, N. & Boettiger, A. N. Tracing DNA paths and RNA profiles in cultured cells and tissues with ORCA. *Nat. Protoc.* **16**, 1647–1713 (2021).
32. Chen, L. F. et al. Structural elements promote architectural stripe formation and facilitate ultra-long-range gene regulation at a human disease locus. *Mol. Cell.* **83**, 1446–61 e6 (2023).
33. Hung, T. C., Kingsley, D. M. & Boettiger, A. N. Boundary stacking interactions enable cross-TAD enhancer-promoter communication during limb development. *Nat. Genet.* **56**, 306–314 (2024).
34. de Laat, W. & Duboule, D. Topology of mammalian developmental enhancers and their regulatory landscapes. *Nature* **502**, 499–506 (2013).

35. Rao, S. S. P. et al. Cohesin loss eliminates all loop domains. *Cell* **171**, 305–20 e24 (2017).
36. Hsieh, T. S. et al. Enhancer-promoter interactions and transcription are largely maintained upon acute loss of CTCF, cohesin, WAPL or YY1. *Nat. Genet.* **54**, 1919–1932 (2022).
37. Thiecke, M. J. et al. Cohesin-dependent and -independent mechanisms mediate chromosomal contacts between promoters and enhancers. *Cell Rep.* **32**, 107929 (2020).
38. Kim, M. et al. Multifaceted roles of cohesin in regulating transcriptional loops. Preprint at *bioRxiv* https://doi.org/10.1101/2024.03.25.586715 (2024).
39. Kane, L. et al. Cohesin is required for long-range enhancer action at the Shh locus. *Nat. Struct. Mol. Biol.* **29**, 891–897 (2022).
40. Zhu, Y., Denholtz, M., Lu, H. & Murre, C. Calcium signaling instructs NIPBL recruitment at active enhancers and promoters via distinct mechanisms to reconstruct genome compartmentalization. *Genes Dev.* **35**, 65–81 (2021).
41. Patta, I. et al. Nuclear morphology is shaped by loop-extrusion programs. *Nature* **627**, 196–203 (2024).
42. Lambert, S. A. et al. The human transcription factors. *Cell* **172**, 650–665 (2018).
43. Boller, S. et al. Pioneering activity of the C-terminal domain of EBF1 shapes the chromatin landscape for B cell programming. *Immunity* **44**, 527–541 (2016).
44. Zaret, K. S. & Carroll, J. S. Pioneer transcription factors: establishing competence for gene expression. *Genes Dev.* **25**, 2227–2241 (2011).
45. Wang, W. et al. TCF-1 promotes chromatin interactions across topologically associating domains in T cell progenitors. *Nat. Immunol.* **23**, 1052–1062 (2022).
46. Di Giammartino, D. C. et al. KLF4 is involved in the organization and regulation of pluripotency-associated three-dimensional enhancer networks. *Nat. Cell Biol.* **21**, 1179–1190 (2019).
47. Kloetgen, A. et al. Three-dimensional chromatin landscapes in T cell acute lymphoblastic leukemia. *Nat. Genet.* **52**, 388–400 (2020).
48. Rothenberg, E. V. Transcriptional control of early T and B cell developmental choices. *Annu. Rev. Immunol.* **32**, 283–321 (2014).
49. Lin, H. & Grosschedl, R. Failure of B-cell differentiation in mice lacking the transcription factor EBF. *Nature* **376**, 263–267 (1995).
50. Northrup, D. L. & Allman, D. Transcriptional regulation of early B cell development. *Immunol. Res.* **42**, 106–117 (2008).
51. Rothenberg, E. V. B cell specification from the genome up. *Nat. Immunol.* **11**, 572–574 (2010).
52. Tsherniak, A. et al. Defining a cancer dependency map. *Cell* **170**, 564–76 e16 (2017).
53. Nabet, B. et al. The dTAG system for immediate and target-specific protein degradation. *Nat. Chem. Biol.* **14**, 431–441 (2018).
54. Heintzman, N. D. et al. Distinct and predictive chromatin signatures of transcriptional promoters and enhancers in the human genome. *Nat. Genet.* **39**, 311–318 (2007).
55. Strahl, B. D. & Allis, C. D. The language of covalent histone modifications. *Nature* **403**, 41–45 (2000).
56. Blackwood, E. M. & Kadonaga, J. T. Going the distance: a current view of enhancer action. *Science* **281**, 60–63 (1998).
57. Lin, Y. C. et al. A global network of transcription factors, involving E2A, EBF1 and Foxo1, that orchestrates B cell fate. *Nat. Immunol.* **11**, 635–643 (2010).
58. Nora, E. P. et al. Spatial partitioning of the regulatory landscape of the X-inactivation centre. *Nature* **485**, 381–385 (2012).
59. Dixon, J. R. et al. Topological domains in mammalian genomes identified by analysis of chromatin interactions. *Nature* **485**, 376–380 (2012).
60. Lam, J. C. et al. YY1-controlled regulatory connectivity and transcription are influenced by the cell cycle. *Nat. Genet.* **56**, 1938–1952 (2024).
61. Vatapalli, R. et al. Histone methyltransferase DOT1L coordinates AR and MYC stability in prostate cancer. *Nat. Commun.* **11**, 4153 (2020).
62. Kapoor, I., Bodo, J., Hill, B. T., Hsi, E. D. & Almasan, A. Targeting BCL-2 in B-cell malignancies and overcoming therapeutic resistance. *Cell Death Dis.* **11**, 941 (2020).
63. Schwickert, T. A. et al. Stage-specific control of early B cell development by the transcription factor Ikaros. *Nat. Immunol.* **15**, 283–293 (2014).
64. Tessoulin, B. et al. BCL2-family dysregulation in B-cell malignancies: from gene expression regulation to a targeted therapy biomarker. *Front. Oncol.* **8**, 645 (2018).
65. Pongubala, J. M. et al. Transcription factor EBF restricts alternative lineage options and promotes B cell fate commitment independently of Pax5. *Nat. Immunol.* **9**, 203–215 (2008).
66. Ryan, R. J. H. et al. A B cell regulome links notch to downstream oncogenic pathways in small B cell lymphomas. *Cell Rep.* **21**, 784–797 (2017).
67. Zhou, Y. et al. OLIVE provides rapid visualization and analysis of chromatin tracing experiments. *Cell Rep. Methods*. https://doi.org/10.1016/j.crmeth.2025.101209 (2025).
68. Weintraub, A. S. et al. YY1 is a structural regulator of enhancer-promoter loops. *Cell* **171**, 1573–88 e28 (2017).
69. Zuin, J. et al. Cohesin and CTCF differentially affect chromatin architecture and gene expression in human cells. *Proc. Natl Acad. Sci. USA* **111**, 996–1001 (2014).
70. Wendt, K. S. et al. Cohesin mediates transcriptional insulation by CCCTC-binding factor. *Nature* **451**, 796–801 (2008).
71. Banigan, E. J. et al. Transcription shapes 3D chromatin organization by interacting with loop extrusion. *Proc. Natl Acad. Sci. USA* **120**, e2210480120 (2023).
72. Sanborn, A. L. et al. Chromatin extrusion explains key features of loop and domain formation in wild-type and engineered genomes. *Proc. Natl Acad. Sci. USA* **112**, E6456–E6465 (2015).
73. Vian, L. et al. The energetics and physiological impact of cohesin extrusion. *Cell* **173**, 1165–78 e20 (2018).
74. Zhou, Y. et al. EBF1 nuclear repositioning instructs chromatin refolding to promote therapy resistance in T leukemic cells. *Mol. Cell.* **82**, 1003–20 e15 (2022).
75. Flotho, C. et al. A set of genes that regulate cell proliferation predicts treatment outcome in childhood acute lymphoblastic leukemia. *Blood* **110**, 1271–1277 (2007).
76. Schuettpelz, L. G. et al. Kruppel-like factor 7 overexpression suppresses hematopoietic stem and progenitor cell function. *Blood* **120**, 2981–2989 (2012).
77. De Coninck, S., Berx, G., Taghon, T., Van Vlierberghe, P. & Goossens, S. ZEB2 in T-cells and T-ALL. *Adv. Biol. Regul.* **74**, 100639 (2019).
78. Ferrai, C., de Castro, I. J., Lavitas, L., Chotalia, M. & Pombo, A. Gene positioning. *Cold Spring Harb. Perspect. Biol.* **2**, a000588 (2010).
79. Beagrie, R. A. et al. Complex multi-enhancer contacts captured by genome architecture mapping. *Nature* **543**, 519–524 (2017).
80. Zhao, J. & Faryabi, R. B. Spatial promoter-enhancer hubs in cancer: organization, regulation, and function. *Trends Cancer* **9**, 1069–1084 (2023).
81. Phanstiel, D. H. et al. Static and dynamic DNA loops form AP-1-bound activation hubs during macrophage development. *Mol. Cell.* **67**, 1037–48 e6 (2017).
82. Li, R. et al. Dynamic EBF1 occupancy directs sequential epigenetic and transcriptional events in B-cell programming. *Genes Dev.* **32**, 96–111 (2018).
83. Bossen, C. et al. The chromatin remodeler Brg1 activates enhancer repertoires to establish B cell identity and modulate cell growth. *Nat. Immunol.* **16**, 775–784 (2015).

84. Sunkel, B. D. & Stanton, B. Z. Pioneer factors in development and cancer. *iScience* **24**, 103132 (2021).
85. Lyu, H. et al. Pioneer factor GATA6 promotes colorectal cancer through 3D genome regulation. *Sci. Adv.* **11**, eads4985 (2025).
86. Fu, X. et al. FOXA1 upregulation promotes enhancer and transcriptional reprogramming in endocrine-resistant breast cancer. *Proc. Natl Acad. Sci. USA* **116**, 26823–26834 (2019).
87. Corces, M. R. et al. Lineage-specific and single-cell chromatin accessibility charts human hematopoiesis and leukemia evolution. *Nat. Genet.* **48**, 1193–1203 (2016).
88. Hu, Y. et al. Lineage-specific 3D genome organization is assembled at multiple scales by IKAROS. *Cell* **186**, 5269–89 e22 (2023).
89. Zolotarev, N., Bayer, M. & Grosschedl, R. EBF1 is continuously required for stabilizing local chromatin accessibility in pro-B cells. *Proc. Natl Acad. Sci. USA* **119**, e2210595119 (2022).
90. Busslinger, G. A. et al. Cohesin is positioned in mammalian genomes by transcription, CTCF and Wapl. *Nature* **544**, 503–507 (2017).

Methods

Experimental model and subject details

Cell culture. DND41, JVM-2 and PGA-1 were purchased from the Leibniz-Institute DSMZ-German Collection of Microorganisms and Cell Lines (DSMZ, cat. nos. ACC525, ACC12 and ACC766). HEK293T (CRL-11268) was purchased from ATCC. Granta519 was from the Broad Novartis Cancer Cell Line Encyclopedia[66]. DND41, JVM-2 and PGA-1 were cultured in RPMI 1640 (Corning, cat. no. 10-040-CM) supplemented with 10% fetal bovine serum (Hyclone, cat. no. SH30070.03), 2 mM L-glutamine (Corning, cat. no. 25-005-CI), 100 U ml^{-1} and 100 µg ml^{-1} penicillin–streptomycin (Corning, cat. no. 30-002-CI), 100 mM nonessential amino acids (Gibco, cat. no. 11140-050), 1 mM sodium pyruvate (Gibco, cat. no. 11360-070) and 0.1 mM 2-mercaptoethanol (Sigma, cat. no. M3148). HEK293T and Granta519 were cultured in DMEM (Corning, cat. no. 10-013-CV) supplemented with 10% fetal bovine serum (Hyclone, cat. no. SH30070.03) and 100 U ml^{-1} and 100 µg ml^{-1} penicillin–streptomycin (Corning, cat. no. 30-002-CI). GSI-resistant DND41 cells were generated as previously described[74]. All cell lines, including the cell lines described below, were grown at 37 °C and 5% CO_2 and were used at a low passage number (<12) and subjected to regular *Mycoplasma* tests and short tandem repeat profiling.

Lentiviral packaging. Lentivirus was produced in HEK293T cells as previously described[27]. In brief, 4.5×10^6 HEK293T cells were plated in 8 ml DMEM in 10-cm dishes 12–16 h before transfection. The lentiviral constructs, packaging plasmid (pCMVdelta) and envelope plasmid (VSV-G) were co-transfected using FuGene HD (Promega, cat. no. E2311). The cells were returned to the incubator for 6–8 h before replacement with 6 ml of medium. Lentiviral supernatants were collected 48 h post-transfection, subjected to 0.45-µm filtration and stored at −80 °C.

CRISPR-Cas9 editing. CRISPR/Cas9 system was used for knocking out EBF1 in Granta519, JVM-2 and PGA-1. Codon-optimized version of Cas9 carrying puromycin resistance gene (Cas9-puro) and sgRNA vectors carrying mCherry (LRmCherry2.1)[91] were used. Cells were transduced with Cas9-puro lentivirus by spinfection at 2,000 rpm for 90 min at 22 °C in the presence of 6 µg ml^{-1} Polybrene (Sigma-Aldrich, cat. no. H9268). Transduced cells were selected 3 days after spinfection with incremental 0.5–2 µg ml^{-1} puromycin until most cells were viable, and maintained in 1 µg ml^{-1} puromycin. Expression of Cas9 was confirmed with western blot (CST, cat. no. 14697S). sgRNA targeting *EBF1* exon 3 (EBF1-g7) was optimized as previously described[74]. Cells transduced with sgRNA were sorted with $DAPI^-mCherry^+$ gating on FACS Aria and used for RNA-seq, Hi-C and apoptosis experiments in Fig. 1.

Generation of Granta519 single cell clones with endogenous EBF1 tagged with $FKBP12^{F36V}$. sgRNA targeting the stop codon of human *EBF1* gene (EBF1-KI-gRNA) was designed with Benchling (https://www.benchling.com/) and cloned in lentiviral sgRNA vector expressing GFP (LRG). Repair templates with $FKBP12^{F36V}$-HA-HA-P2A-BSD cassettes flanked by 447-bp sequences homologous to upstream and downstream of the EBF1 stop codon were designed with SnapGene and synthesized in pUC57 plasmid by GenScript (pUC57-FKBP). Granta519-Cas9-expressing cells were electroporated with LRG-EBF1-KI-gRNA and pUC57-FKBP using an Invitrogen Neon Transfection System as per the manufacturer's recommendations. Cells were replated in a 12-well plate with antibiotic-free medium for 24 h and transferred to full medium with blasticidin selection for 15 days. Live single cells were sorted to 96-well plates containing blasticidin and cultured until visible clones were formed and further expanded. Genomic DNA was extracted with a Quick-DNA Miniprep Plus kit 200 Preps (Zymo, cat. no. D4069) and PCR primers targeting the insertion site were used to determine the homozygous insertion of the FKBP cassette. Single cell clones with homozygous insertion of the FKBP cassette were subject to $dTAG^V$-1 (Bio-Techne, cat. no. 6914) dosage and time titration by western blot. Finally, several single cell clones including Granta519-EBF1-FKBP-KI 26, 27, 29 and 97 showed complete degradation of EBF1 in a 24-h 125 nM $dTAG^V$-1 treatment and were further validated with time-course RNA-seq.

RNA sequencing. Strand-specific RNA-seq for DND41 GSI-sensitive and GSI-resistant cells was previously published (GSE173872)[74]. RNA-seq was performed in the following cells with three replicates per condition: Granta519-Cas9 control and LRmCherry2.1-EBF1-g7 cells sorted 3 days post-transduction; Granta519-EBF1-FKBP-KI clones 26, 27, 29 and 97 treated with 125 nM $dTAG^V$-1 for 0, 6 and 24 h; and Granta519-EBF1-FKBP-KI clones 27 and 97 treated with 125 nM $dTAG^V$-1 for 24 h and washed with dTAG-free medium five times and replated for 6 and 24 h (washout). In all experiments, $3–5 \times 10^5$ cells were washed with 1× PBS and lysed with 350 µl RLT Plus buffer (QIAGEN) supplemented with 2-mercaptoethanol, vortexed briefly and immediately proceeded to RNA isolation with an RNeasy Plus Micro kit (QIAGEN, cat. no. 74034). RNA integrity numbers (RINs) were determined using TapeStation 4150 (Agilent), and all samples used for RNA-seq library preparation had RIN > 9.5. A total of 300–800 ng of total RNA was used and libraries were prepared using the SMARTer Stranded Total RNA Sample Prep kit-HI Mammalian (Clontech, cat. no. 634873). Libraries were paired-end sequenced on Illumina NextSeq 550 (38 bp+38 bp) or Novaseq 6000 (61 bp+61 bp).

Assay for transposase-accessible chromatin sequencing. ATAC-seq was performed as previously described[92] and three replicates were performed for each condition. In brief, 5×10^4 cells were pelleted at 800*g* and washed with 50 µl of ice-cold 1× PBS (Corning, cat. no. 21031CV), followed by a 2-min treatment with 50 µl lysis buffer (10 mM Tris-HCl, pH 7.4, 3 mM $MgCl_2$, 10 mM NaCl and 0.1% Igepal, Millipore, cat. no. CA-630). Pelleted nuclei were resuspended in 50 µl of transposition buffer (25 µl of 2× TD buffer, 22.5 µl of molecular biology grade water and 2.5 µl Tn5 transposase (Illumina, cat. no. FC-121-1030)) to tag the accessible chromatin for 45 min at 37 °C. Tagmented DNA was purified with MinElute Reaction Cleanup kit (QIAGEN, cat. no. 28204) and amplified with seven PCR cycles. Libraries were purified using QiaQuick PCR purification kit (QIAGEN, cat. no. 28106) and eluted in 20 µl EB buffer. Indexed libraries were assessed for nucleosome patterning on TapeStation 4150 (Agilent) and paired-end sequenced on Illumina NextSeq 550 (38 bp+38 bp) or Novaseq 6000 (61 bp+61 bp).

Chromatin immunoprecipitation sequencing. ChIP-seq for histone marks was performed as previously described[27]. In brief, 1×10^7 cells were crosslinked with 1% formaldehyde and lysed. Nuclei were extracted and resuspended in 1% SDS and sonicated using Brandson 450 sonicator with 25% amplitude, 0.5 s on, 1 s off for a total of 4 min 30 s on. Solubilized chromatin was then diluted and cleared with IgG (CST, cat. no. 2729S) and recombinant protein G-conjugated agarose beads (Invitrogen, cat. no. 15920-010) for 1 h at 4 °C. The cleared supernatant was subsequently immunoprecipitated with antibodies recognizing H3K27ac (Active Motif, cat. no. 39133), H3K4me1 (Abcam, cat. no. ab8895) or H3K27me3 (CST, cat. no. 9733) overnight at 4 °C. Buffers in all steps above were supplemented with protease inhibitors (Roche, cat. no. 11697498001). Antibody–chromatin complexes were captured with recombinant protein G-conjugated agarose beads, washed with low-salt wash buffer, high-salt wash buffer, LiCl wash buffer and TE buffer with 50 mM NaCl and eluted. Input samples were prepared by the same approach, without immunoprecipitation.

ChIP-seq for TFs was performed as previously described[83]. In brief, Dynabeads Protein G (Thermo Fisher Scientific, cat. no. 10003D) was incubated with (1) polyclonal anti-EBF1 (1C) antibody, which recognizes an N-terminal EBF1 peptide (RG)[43]; (2) commercial EBF1 antibody (Millipore, cat. no. AB10523); and (3) SMC1a (Bethyl, cat. no. A300-055A), YY1 (Active Motif, cat. no. 61779) and CTCF (EMD Millipore,

cat. no. 07-729) for 8–12 h in PBS + 0.5% BSA at 4 °C. Then, 4×10^7 cells were crosslinked with 1% formaldehyde and 1.5 mM EGS (Thermo Fisher Scientific, cat. no. 21565) and sonicated using a Brandson 450 sonicator with 17% amplitude, 10 s on, 1 min off, ten times. The lysate was then cleared by centrifuging for 5 min at 16,000*g* at 4 °C and incubating with antibody-bound beads and 1% Triton X-100 (Roche, cat. no. 10789704001) overnight at 4 °C. Buffers in all steps above were supplemented with protease inhibitors (Roche, cat. no. 11697498001). Antibody–chromatin complexes captured on beads were then separated on magnet and washed with wash buffer 1, 2, 3, LiCl wash buffer, TE buffer and eluted.

Following elution of histone mark and transcription factor samples, RNase (Roche, cat. no. 10109169001) and Proteinase K (Invitrogen, cat. no. 25530-049) treatments were performed, and reverse crosslinked at 65 °C overnight. DNA was purified with a QiaQuick PCR Purification kit (QIAGEN, cat. no. 28106). Libraries were then prepared using the NEBNext Ultra II DNA library Prep kit for Illumina (NEB, cat. no. E7645S) with single (NEB, cat. no. E7335, cat. no. E7710) or dual (NEB, cat. no. E7600, cat. no. E7780) indexing. Two replicates were performed for each condition. Indexed libraries were validated for quality and size distribution using a TapeStation 4150 (Agilent), quantified by a KAPA Library Quantification kit (Roche, cat. no. KK4824) and paired-end sequenced on Illumina NextSeq 550 (38 bp+38 bp) or Novaseq 6000 (61 bp+61 bp).

In situ Hi-C. In situ Hi-C was performed in Granta519-Cas9 control and LRmCherry2.1-EBF1-g7 cells sorted 3 days post-transduction. In brief, 1×10^6 cells were washed with 1× PBS containing 3% BSA and fixed with 2% formaldehyde, followed by using an Arima-Hi-C kit (ARIMA, cat. no. A510008) as per the manufacturer's instructions. Samples passing Arima-QC1 were used for library construction with an Accel-NGS 2S Plus DNA Library kit (Swift, cat. no. 21024) and 2S Set A Indexing kit (Swift, cat. no. 26148) and assessed with Arima-QC2. Samples passing Arima-QC2 were subsequently PCR-amplified based on Arima-QC2 calculations, quantified with TapeStation 4150 (Agilent) and a KAPA Library Quantification kit (Roche, cat. no. KK4824) and paired-end sequenced on an Illumina NextSeq 550 (38 bp+38 bp).

SMC1 and EBF1 HiChIP. SMC1 and EBF1 HiChIP was performed in Granta519 as previously described with slight modifications[27]. In brief, 2×10^7 cells were crosslinked with 2% formaldehyde (Thermo Fisher Scientific, cat. no. 28908) for 10 min and subsequently quenched with 0.125 M glycine (Invitrogen, cat. no. 15527-013). Chromatin was digested using MboI restriction enzyme (NEB, cat. no. R0147), followed by biotin incorporation with Biotin-14-dATP (Jena Bioscience, cat. no. NU-835-BIO14-S). DNA was then ligated with T4 ligase (NEB, cat. no. M0202L) and sonicated on a Covaris LE220. Sheared chromatin was diluted fourfold with ChIP dilution buffer (16.7 mM Tris pH 7.5, 167 mM NaCl, 1.2 mM EDTA, 0.01% SDS and 1.1% Triton X-100), cleared with IgG (CST, cat. no. 2729S) and then incubated with anti-SMC1 antibody (Bethyl, cat. no. A300-055A), polyclonal anti-EBF1 (1C) antibody recognizing an N-terminal EBF1 peptide (RG)[43] or commercial EBF1 antibody (Millipore, cat. no. AB10523) at 4 °C overnight. Chromatin–antibody complexes were captured by Protein-A magnetic beads (Pierce, cat. no. 88846) and subsequently washed with low-salt wash buffer, high-salt wash buffer and LiCl wash buffer (detailed procedure available upon request) and eluted. DNA was purified with a MinElute PCR Purification kit (QIAGEN, cat. no. 28004) and quantified using a Qubit dsDNA HS Assay kit (Invitrogen, cat. no. Q32851). Then, 50–150 ng DNA was used for capture with Dynabeads MyOne Streptavidin C-1 (Invitrogen, cat. no. 65001) and an appropriate amount of Tn5 enzyme (Illumina, cat. no. FC-121-1030) was added to captured DNA to generate the sequencing library. Paired-end sequencing was performed on an Illumina Novaseq 6000 (61 bp + 61 bp).

Micro-C. Micro-C was performed as previously described with optimization[22]. For each reaction, 5×10^6 cells were crosslinked with 1% formaldehyde for 10 min and quenched with 125 mM glycine for 5 min. Cells were washed with 1× PBS twice at room temperature and resuspended at 1×10^6 cells per ml and crosslinked at a final concentration of 3 mM EGS (Thermo Scientific, cat. no. PI21565). Double-crosslinking was quenched with 0.4 M glycine for 10 min at room temperature, washing twice with cold PBS and storing at −80 °C until further processing.

The thawed cell pellet was resuspended in 500 µl MB1 buffer (50 mM NaCl, 10 mM Tris-HCl, pH 7.5, 5 mM $MgCl_2$, 1 mM $CaCl_2$, 0.2 % NP-40 and 1× cOmplete EDTA-free PI) and rotated for 20 min at 4 °C. Nuclei were centrifuged at 8,000*g* for 5 min at 4 °C and rinsed with 500 µl MB1 once and resuspended in 500 µl MB1. Chromatin is digested by appropriate amounts of MNase (25 U per 10^6 for Granta519 and 20 U per 10^6 for DND41) for 10 min at 37 °C shaking at 850 rpm. MNase digestion was quenched by 4 mM EGTA for 10 min shaking at 65 °C. The nuclei pellet was rinsed twice in 500 µl cold MB2 (50 mM NaCl, 10 mM Tris-HCl, pH 7.5 and 10 mM $MgCl_2$), and 5 µl was saved and adjusted to 200 µl TE buffer and saved in −80 °C as 1% input. Digested chromatin was then subjected to de-phosphorylation with Shrimp Alkaline Phosphatase rSAP (NEB, cat. no. M0371S), end-chewing with T4 Polynucleotide Kinase (NEB, cat. no. M0201L) and end-labelling with Biotin-14-dATP (Jena Bio, cat. no. NU-835-BIO14-L) and Biotin-11-dCTP (Jena Bio, cat. no. NU-809-BIOX-L) (detailed procedure available upon request). Enzymatic reactions were quenched with 30 mM EDTA for 20 min at 65 °C and rinsed once with 500 µl of cold MB3 (50 mM Tris-HCl pH 7.5 and 10 mM $MgCl_2$). Chromatin was then ligated with T4 DNA ligase at 20 U μl^{-1} for 4 h with rotation at room temperature. After biotin-end removal with Exonuclease III for 15 min at 37 °C, 25 µl of 20 mg ml^{-1} Proteinase K and 25 µl of 10% SDS were added to sample or input and de-crosslinked at 65 °C and 850 rpm overnight.

After RNase A treatment at 37 °C for 45 min, chromatin was mixed with 1× volume of PCI (Invitrogen, cat. no. 15593031) at room temperature and extracted with MaXtract high density columns (QIAGEN, cat. no. 129056). Then, 0.1× volume of 3 M NaAc, 2.5× volume of 100% ethanol and 0.5 µl 20 mg ml^{-1} glycogen were added and precipitated at −80 °C for 2 h. Chromatin was pelleted and resuspended with 50 µl 1× TE and then concentrated with a ZymoClean DNA purification kit (Zymo, cat. no. D4013). For each input and sample, 1 µl purified chromatin was examined with Agilent D5000 reagent and ScreenTape (Agilent, cat. no. 5067-5588 and 5067-5589) and the remaining samples were separated in 3.5% NuSieve GTG Agarose gel (Lonza, cat. no. 50080). Successful MNase digestion and T4 ligation should yield ~70% mono-nuclei at 150 bp and di-nuclei at 300 bp on TapeStation, respectively. Ligated chromatin between 300 bp and 400 bp was excised from the gel and purified with Zymoclean Gel DNA Recovery kit (Zymo, cat. no. D4007) and eluted in 50 µl elution buffer. Samples were quantified with Qubit dsDNA HS Assay kit and saved at −80 °C until further processing.

For each sample, 5 µl Dynabeads MyOne Streptavidin C1 beads were transferred to a fresh tube with 500 µl 1× TBW (5 mM Tris-HCl, pH 7.5, 0.5 mM EDTA, 1 M NaCl and 0.05% Tween-20) and placed on magnetic rack. Beads were washed again with 1× TBW and resuspended in 150 µl 2× B&W buffer (10 mM Tris-HCl, pH 7.5, 1 mM EDTA and 2 M NaCl). Then, 100 µl elution buffer was added to each thawed chromatin sample and joined with beads and rotated at room temperature for 20 min. Beads were cleared on a magnet and resuspended in 300 µl 1× TBW shaking at 55 °C and 900 rpm for 2 min and cleared on a magnet. Beads were washed again with 1× TBW and 10 mM Tris-HCl and finally resuspended in 50 µl 0.1× TE. Beads containing chromatin were subject to end-prep and adaptor ligation using a NEBNext Ultra II DNA Library Prep kit (NEB, cat. no. E7645S) and washed twice with 1× TBW and 10 mM Tris-HCl before resuspension in 24 µl elution buffer. Minimum PCR with 2× KAPA HiFi Hot Start Mix (Roche, cat. no. KK2601) and NEB dual indexes were performed with DNA on beads and purified twice with SPRIselect beads (Beckman Coulter, cat. no. B23318), quantified with an

HSD1000 TapeStation 4150 (Agilent) and KAPA Library Quantification kit (Roche, cat. no. KK4824) and paired-end sequenced on an Illumina Novaseq 6000 (61 bp + 61 bp).

Optical reconstruction of chromatin architecture. *Probe design and synthesis*. The 3-Mb genomic sequences spanning *MYC* promoter in hg19 (chr8, 127,800,000–130,800,000) were divided into 100 × 30-kb bins/steps and extracted from Ensembl GRCh37.75 (Extended Data Fig. 8a). For each bin, multiple sets of 42-bp probes with homology to the genomic sequences were designed with OligoMiner pipeline[93] using the default parameters except adjusting the spacing between probes. The set with closest to 200 probes was further manually filtered by NCBI BLAST to remove probes with potential multiple hybridization sites on the human genome. This ensures that the signal of each step of the sequential imaging is specific, and the intensity is comparable. For probes in each step, a unique 20-bp barcode sequence was added to both sides[31,94]. For all probes, a pair of 20-bp universal primer binding sequences were added for PCR amplification, resulting in final probe length of 122 bp. A total of 19,649 probes were designed for the 3-Mb *MYC* locus and used in DND41 (Fig. 7). To further increase specificity, a subset of 5,891 probes covering 5′ of the *MYC* promoter were ordered as a separate pool and used in Granta519 (Figs. 3 and 4). A set of 8,128 probes and a set of 5,912 probes were designed for *KLF7* and *ZEB2* loci using similar procedures, respectively, and all probe sequences can be found in Supplementary Table. All oligonucleotide pools were purchased from Twist.

Oligonucleotide pools were amplified based on Twist recommended PCR amplification protocol to achieve maximal yield without overamplification. For instance, 2 ng *MYC* 3-Mb probes were first amplified using universal primers with fiducial binding sequence (20 bp) added to both forward and reverse primers. KAPA HiFi HotStart ReadyMix (Roche, cat. no. KM2605) was used with annealing temperature at 65 °C for 12 cycles as per the manufacturer's recommended PCR procedure. PCR products were purified with Zymo DNA Clean & Concentrator-5 (cat. no. D4013) and quantified with Nanodrop. Then, 1 µl of purified DNA was ran on a TapeStation HSD1000 to determine the uniform length of PCR products. Overamplification will lead to non-specific peaks larger than the expected product (162 bp). Then, 20 ng DNA per reaction was used for a second amplification with 6–10 reactions and examined again for a uniform PCR product. A similar quality control procedure was carried out for *MYC* 5′ probes, *KLF7* probes and *ZEB2* probes. PCR products were joined and purified with Zymo DNA Clean & Concentrator-5 (cat. no. 4013), and T7 in vitro transcription (NEB, cat. no. E2040S) was performed at 37 °C overnight. Reverse transcription was performed with maxima RT-H (Thermo, cat. no. EP0751) at 50 °C with universal forward primer for 2.5 h, and EDTA/NaOH was added to remove RNA at 92 °C for 10 min. Finally, ssDNA was purified with Zymo DNA Clean & Concentrator-100 (cat. no. D4030), SpeedVac dried and resuspended in molecular grade water to 50 µM.

Primary probe hybridization. The 40-mm round, glass coverslips (Bioptechs, cat. no. 10200-064) were coated with 0.01% poly-L-lysine (Sigma-Aldrich, cat. no. P4832) for 15 min at room temperature. SSCT/F buffer containing 2× SSC + 0.1% Tween-20 + 50% formamide (20× SSC Buffer, Corning, cat. no. 46-020-CM; Tween-20, Millipore, cat. no. 655204; and deionized formamide, Thermo, cat. no. AM9344) were prepared at room temperature and preheated in a water bath at 60 °C and 95 °C. A square region was drawn on each coverslip with a hydrophobic barrier pen (Vector Laboratories, cat. no. H-4000) and 200 µl of Granta519 or DND41 cells at 10^7 cells per ml in PBS were gently settled within the barrier. After 30 min of incubation in a humidified chamber at room temperature, the cells on coverslips were crosslinked with 4% formaldehyde in PBS (Thermo, cat. no. 28908) and permeabilized for 15 min with 0.5% Triton X-100 (Millipore, cat. no. 648466) in PBS at room temperature. Cells were then dehydrated with 70%, 90% and 100% ethanol for 2 min each and slightly air dried before washing in SSCT/F for 5 min at room temperature, 3 min at 95 °C and 20 min at 60 °C. A primary hybridization mix containing 7 µl of 50 µM probes, 10 µl of 100 mM dNTPS (Denville, cat. no. C788T68), 4 µl 10 mg ml^{-1} RNase A (Invitrogen, cat. no. EN0531), 45 µl 100% formamide and 24 µl 4× dextran sulfate mix (40% dextran sulfate, Sigma, cat. no. D8906; 4% PVSA, Sigma, cat. no. 278424; 8× SSC; and 0.4% Tween-20) were thoroughly mixed and added to each coverslip and sealed with a 22 × 30-mm coverslip. Coverslips were then heated on a heat block in 95 °C water bath for 3 min to denature genomic DNA and incubated overnight at 37 °C.

Sequential imaging. To accurately select fields of view (FOVs) and Z-stacks, hybridization of fiducial oligos and the first readout oligonucleotides was conducted before mounting the coverslip on the microscope, which differs from the original ORCA protocol. Specifically, the 22 × 30-mm coverslip was removed after overnight hybridization and the 40-mm round coverslip containing the cells was washed in 2× SSCT at 60 °C and room temperature for 10 min each. For *MYC* 5′ probes in Granta519 and *ZEB2* probes in DND41, secondary hybridization mix containing 1 µl 100 µM Cy3-fiducial oligonucleotides, 1 µl 20 µM Readout_008 oligonucleotides, 2 µl 10 µM NDB_1281_Alexa647 oligonucleotides, 22.5 µl 100% formamide, 22.5 µl 4× dextran sulfate mix and 41 µl H_2O were mixed and added per coverslip. For *MYC* 3-Mb probes in DND41, Readout_029 and NDB_1279_Alexa647 were used. For *KLF7* probes in DND41, Readout_005 and NDB_1279_Alexa647 were used. After 1 h of incubation in a humidified chamber at room temperature shielded from light, coverslips were washed in 2× SSCT at 60 °C and room temperature for 5 min each and transferred individually to 60-mm Petri dishes containing 2× SSC. Coverslips were either used immediately or stored for less than 24 h at 4 °C.

Sequential hybridization and imaging on the microscope (Bruker Vutara VXL, software version SRX 7.3.22) proceeded after visual confirmation of even cell distribution, bright fiducial signal at 0.05% laser power and a highly overlapping first readout signal at 0.5% laser power, which were the laser powers used for all ORCA experiments. After the first round of imaging, strand-displacement (also called toehold) oligonucleotides for the first readout were hybridized for 30 min in 25% formamide, 2× SSC and washed twice with 30% formamide in 2× SSC. Successful removal of the signal was confirmed with imaging. The coverslip was then rinsed of imaging buffer using 2× SSC, and the second readout oligonucleotides were hybridized for 30 min. For each 30-step ORCA, we conducted 60 rounds of hybridization, washing, imaging for each set of readout and strand-displacement oligonucleotides, a process that took 1 week on average. Similarly, all 36-step and 72-step ORCA experiments were conducted with 72 and 144 rounds of sequential hybridization, washing and imaging, and took 1 and 2 weeks on average, respectively. An automated fluidic system with daily refreshed buffers was used for all the experiments.

Cell proliferation. Cell proliferation was measured with a CellTiter Glo Luminescent Cell Viability Assay (Promega, cat. no. G7571) according to the manufacturer's instructions. The Granta519-EBF1-FKBP-KI clone 27 was plated in five replicates with 1,000 cells per well on 96-well plates. Luminescence was measured 24 h after plating (day 0) and every day for a total of 6 days. Statistics for cell growth changes were calculated using a Student's *t*-test.

Flow cytometry analysis. Granta519-Cas9, JVM-2-Cas9 and PGA-1-Cas9 cells with control or LRmCherry2.1-EBF1-g7 were sorted 3 days post-transduction and cultured for 3 days (day 6). For each replicate, 5×10^5 cells were washed in 1× PBS and resuspended in 100 µl 1× annexin V binding buffer (BD, cat. no. 556454). Then, 5 µl FITC-annexin V (BD, cat. no. 556420) was added and incubated in the dark at room temperature for 15 min. Then, 400 µl of 1× annexin V binding buffer containing 1:1,000 TO-PRO3 (Thermo Fisher Scientific, cat. no. R37170) was

added and immediately followed by flow cytometry analysis on a BD LSR II. A total of 1×10^6 Granta519-EBF1-FKBP-KI clones 27 and 97 were treated with 125 nM dTAG for 0, 6 and 24 h and stained with L/D Aqua (Invitrogen, cat. no. L34957) for 15 min at room temperature. Cells were washed with 1× PBS and then stained with 5 µl APC human anti-PD-L1 (BioLegend, cat. no. 329708) in 100 µl 1× PBS for 15 min on ice before analysis on BD LSR II. Experiments were repeated three times with 3–5 replicates per condition.

Western blot. A total of $0.2–1 \times 10^6$ cells were washed in ice-cold 1× PBS and lysed with whole lysis buffer (2% SDS and 60 mM Tris) supplemented with proteinase inhibitors. Protein concentration was determined with DC Protein Assay Reagents Package (Bio-Rad, cat. no. 5000116) and 5–20 µg proteins were used for SDS–PAGE electrophoresis in Tris-MES-SDS running buffer (GenScript, cat. no. M00654, cat. no. M00677). Gels were then transferred to a methanol-activated PVDF membrane (Cytiva, cat. no. 10600023), blocked with 5% skim milk in 1× TBST at room temperature for 1 h, and incubated with primary antibodies at 1:1,000 to 1:20,000 dilutions in 5% skim milk at 4 °C overnight. After washing with 1× TBST for 3 × 10 min, secondary antibodies (Millipore, cat. no. 401315-2 ml, cat. no. 401215-2 ml) were added at 1:3,000 or 1:6,000 dilution in 5% skim milk and incubated at room temperature for 1 h. Following a 3 × 15-min wash in 1× TBST, imaging was conducted with ECL Prime Western Blotting Detection Reagents (Cytiva, cat. no. RPN2232) and autoradiography films. Primary antibodies: GAPDH (D16H11) XP (CST, cat. no. 5174); MYC (Y69) (Abcam, cat. no. ab32072); β-actin clone AC-74 (Sigma-Aldrich, cat. no. A5316); Cas9 (7A9-3A3) (CST, cat. no. 14697); and SMC1 (BL-205-2G8) (Bethyl, cat. no. A700-018).

Statistics and reproducibility

The statistical significance of differences between measurements was determined by a two-sided Wilcoxon rank-sum test using R (version 3.6.1) wilcox.test function and FWER-adjusted for more than one test, unless otherwise stated. To comply with the journal's requirement for reporting exact *P* values, we indicated $P = 0$ in the figure whenever the calculated *P* values were below R's lower bound ($P < 2.2 \times 10^{-16}$) and hence unavailable for reporting. Statistical details of experiments can be found in the figure legends. No statistical method was used to predetermine sample size and no data were excluded from the analyses. The experiments were not randomized. The Investigators were blinded to allocation during ORCA data analysis. Visualizations were conducted with R and MATLAB.

In compliance with the journal's requirement for reporting the number of independent experiments or the sample size in each figure panel, we summarized the information here to avoid overwhelming the legends. ATAC-seq: three biological replicates per condition. Related to Extended Data Fig. 1h,i. ChIP-seq: two biological replicates per condition across the entire paper. In situ Hi-C: one biological replicate per condition. Related to Fig. 1e and Extended Data Fig. 1j. HiChIP: one biological replicate per condition across the entire paper. RNA-seq: three biological replicates per condition across the entire paper. Micro-C: Granta519: one technical replicate per condition for two biological replicates. Related to Figs. 2 and 3; Extended Data Figs. 2, 5 and 8. DND41: one biological replicate each for GSI-sensitive and GSI-resistant cells. Related to Figs. 6 and 7; Extended Data Figs. 6–8. ORCA: Granta519: one technical replicate per condition for two biological replicates. Related to Figs. 3–5 and Extended Data Figs. 3–5. DND41 *ZEB2*, *KLF7* loci: one biological replicate each for GSI-sensitive and GSI-resistant cells. Related to Fig. 6 and Extended Data Fig. 6. DND41 *MYC* locus: two biological replicates each for GSI-sensitive and GSI-resistant cells. Related to Fig. 7 and Extended Data Figs. 7 and 8.

Quantification and statistical analysis

Definition of regulatory elements. The following definitions of regulatory elements were used throughout the paper. Promoters were defined as ±2.5 kb from the transcription start site of each expressed gene. Enhancers were defined as H3K27ac peaks, excluding the ones overlapping with promoters.

Gene annotation. A total of 2,828,317 Ensembl transcripts in GRCh37.75 assembly were downloaded in gtf format. For each Ensembl gene id (ENSG), the longest transcript (ENST) was used to assign a unique transcriptional start site and gene position. After exclusion of genes annotated as rRNA or on chromosome M, 57,209 gene annotations were used in RNA-seq analysis.

ATAC-seq data analysis. *Alignment*. Reads from ATAC-seq experiments were trimmed with Trim Galore (version 0.4.1) with parameters -q 15 –phred33 –gzip –stringency 5 -e 0.1 –length 20. Trimmed reads were aligned to the Ensembl GRCh37.75 primary assembly including chromosomes 1–22, chrX, chrY, chrM and contigs using BWA (version 0.7.13)[95] with parameters bwa aln -q 5 -l 32 -k 2 -t 6. Paired-end reads were grouped with bwa sampe -P -o 1000000. Reads mapped to contigs, ENCODE blacklist and marked as duplicates by Picard (version 2.1.0) were discarded and the remaining reads were used in downstream analyses and visualization.

Peak calling and differential accessibility analysis. Peaks in each aligned replicate were identified using MACS2 (version 2.0.9)[96] with parameters –nomodel –nolambda –format = BAM -g hs -p 1E-5 –bw = 300 –keep-dup = 1. All peaks from replicates of each experiment were combined using bedtools 'merge' function and the union of peaks was quantified over each aligned bam file using bedtools 'coverage' and normalized to RPKM. Differential accessibility analysis was performed using DEseq2[97] with parameters test = 'Wald', betaPrior = F, fitType = 'parametric'. For comparison of time-course EBF1 degradation and restoration, significance cutoff was abs($\log_2$(fold change)) > 1 and false discovery rate (FDR) < 1×10^{-3}.

ChIP-seq data analysis. Reads from ChIP-seq experiments were aligned with the same procedure as ATAC-seq above. For Granta519-EBF1 ChIP-seq, peaks of each library were identified using MACS2 (version 2.0.9)[96]- with parameters -p 1E-3 -g hs –nomodel –shiftsize = 0.5 × fragment_length –format = BAM –bw = 300 –keep-dup = 1 and with corresponding input control. The 25,227 reproducible EBF1 ChIP-seq peaks identified in libraries of both replicates of both antibodies were used in downstream analyses. For comparing protein loading, reproducible EBF1-bound regions were quantified on each ChIP-seq bam files using bedtools 'coverage' and normalized to RPKM and averaged between the two replicates of each antibody. Clustering of reproducible EBF1-bound regions (Fig. 1a) was performed with R function hclust (dc, method = 'average', members = NULL) and hc_tree <- cutree (hc, *k* = 15) and visualized with 'pheatmap'. Dynamic EBF1 peaks were filtered as reproducible EBF1 peaks >5 averaged RPKM in untreated Granta519-EBF1-FKBP-KI clone 27. The 7,777 peaks with $\log_2$(fold change) < −1 of averaged RPKM between 6 h and 24 h dTAG-treated versus untreated and $\log_2$(fold change) > 1 of averaged RPKM between 6 h and 24 h washout versus 24 h dTAG-treated were defined as dynamic EBF1 peaks. SMC1, CTCF and YY1 ChIP-seq libraries were individually quantified on EBF1 peaks using bedtools 'coverage' and normalized to RPKM and averaged between the two replicates per condition and $\log_2$ fold changes were calculated as above.

For tag density plots, aligned bam files of the two replicates of each condition were merged using samtools (version 1.3)[98] 'cat' command. For each merged library, fragment length was estimated with HOMER 'makeTagDirectory'. HOMER 'annotatePeaks.pl' was used on merged libraries and visualized with R function 'pheatmap'. For merged libraries genome tracks, a bedgraph of reads normalized to reads per million was generated with bedtools 'genomecov'. Selected genomic loci were visualized with R package Sushi (version 1.18.0)[99] function

'plotBedgraph'. Genome-wide uploadable bigWig files were generated with UCSC tools (version 329)[100] 'bedGraphToBigWig'.

Hi-C, SMC1 HiChIP and Micro-C analysis. *Alignment and significant interaction calling*. Raw reads for Granta519-Cas9 ctrl and EBF1-KO Hi-C, Granta519-EBF1-FKBP-KI clones 27 and 97 time-course Micro-C, and DND41 parental and GSI-resistant Micro-C samples were processed with Juicer (version 1.5.6)[101] with parameters -g hg19 -s none. To generate interaction maps of 30-kb resolution in comparison with ORCA data, juicer_tools.1.7.6 'pre' command was used on merged_nodups.txt with -r 2,500,000, 1,000,000, 500,000, 250,000, 100,000, 50,000, 30,000, 25,000, 10,000 and 5,000 to generate the final.hic files. Normalized contact matrices were extracted using juicer_tools.1.7.6 'dump' command with 'observed VC_SQRT BP 30000' for chromosome 8 (*MYC*) and chromosome 2 (*ZEB2* and *KLF7*) for plotting interaction maps with R 'pheatmap' (Figs. 3, 6 and 7). Each .hic file was also converted to .mcool files using 'hic2cool convert' to maintain VC_SQRT normalization for quantification in Fig. 2.

Raw reads for each HiChIP sample were processed with Hi-C-Pro (version 2.5.0)[102] to obtain putative interactions with default parameters except LIGATION_SITE = GATCGATC and GENOME_FRAGMENT generated for MboI restriction enzyme. Valid pairs, self-circle and dangling-end interactions in *cis* were used as input for significant interaction calling in '.bedpe' format. Mango (version 1.2.0)[103] step 4 identified putative significant interaction anchors by MACS peak calling with MACS_qvalue = 0.05 and MACS_shiftsize = 75. Mango step 5 identified significant interactions with default parameters except maxinteractingdist = 2,000,000 and MHT = found. Only significant interactions with PETs ≥ 5 were used in the following analyses.

TAD boundary analysis. Raw reads for Granta519-Cas9 ctrl and EBF1-KO Hi-C samples were processed with Open2C's distiller-nf (version 0.3.4)[104] to generate mcool files. Boundaries were identified in Python (version 3.9.13) using cooltools[105] with window sizes of 50,000, 100,000 and filtered with boundary strength > 0.5 with both window sizes. Boundaries in control conditions with EBF1 < 2.5 kb are considered EBF1-bound. Pileup of EBF1-bound or EBF1-unbound boundaries in Ctrl and EBF1-KO Hi-C were calculated with cooltools.pileup and visualized with matplotlib.pyplot (Fig. 1e).

Long-range regulatory loops. Long-range regulatory loops were defined using SMC1 and EBF1 HiChIP significant interactions. Significant interactions with EBF1, SMC1, CTCF, YY1 or H3K27ac ChIP-seq signal on both loop anchors were further classified into enhancer–enhancer (EE), enhancer–promoter (EP), promoter–promoter (PP), CTCF–CTCF and other interactions based on the presence of enhancers, promoters and CTCF peaks at the summit of the two anchors ± 5 kb. Normalized interactions at selected loci were visualized with R package Sushi[99] (version 1.18.0) function 'plotBedpe'.

Differential compartment calling. A/B compartments detected at 50-kb resolution were tested. Hi-C processed data were converted into the HOMER (version 4.11)[19] 'HiCSummary' format. Subsequently, the Hi-C data were processed with HOMER command 'makeTagDirectories' with parameters -format 'HiCSummary'. To identify compartment regions across the genome, the HOMER runHiCpca.pl command was used on each condition with H3K27ac ChIP-seq as reference to ensure sign consistency via the -active option. To concatenate PC values from each condition, HOMER annotatePeaks.pl was used with the -noblanks and -bedGraph options. Scatter-plots of the PC values from EBF1 Ctrl and knockout conditions were plotted.

Hub analysis. Hubs were defined as previously described as '3D clique'[27]. In brief, an undirected graph of regulatory interactions was constructed for each HiChIP, where each vertex was an enhancer or a promoter, and each edge was a significant enhancer–enhancer, enhancer–promoter or promoter–promoter interaction. Clusters of interacting enhancers and/or promoters were defined by spectral clustering[106] of the regulatory graph interactions using cluster_louvain function in igraph R package with default parameters. Connectivity of an enhancer–promoter cluster was defined as the number of edges connecting vertices within the cluster. The connectivity of clusters was ranked in ascending order and plotted against the rank. Enhancer–promoter hubs were defined as clusters of enhancers and promoters with connectivity greater than the cutoff set as the elbow of the cumulative connectivity curve, which is shown as a tangent line in Fig. 1f. Hubs with >10 or ⩽10 expressed genes (defined in the following section) are considered gene-dense or gene-sparse hubs, respectively. Pairwise interactions between enhancers and promoters in hubs were quantified in Granta519-EBF1-FKBP-KI clone 27 time-course Micro-C .mcool files with VC_SQRT normalization using cooltools[105]. Interactions with $\log_2$(fold change) < −0.5 between 6 h or 24 h dTAG-treated versus untreated and $\log_2$(fold change) > 0.5 between 6 h or 24 h washout versus 24 h dTAG-treated were defined as differential loops. Pileup plots of differential loops on Granta519-EBF1-FKBP-KI clone 27 time-course Micro-C were generated with R package GENOVA (version 1.0.1)[107] APA and 'visualise' functions (Fig. 2g).

RNA-seq data analysis. RNA-seq data was aligned to Ensembl GRCh37.75 primary assembly, including chromosomes 1–22, chrX, chrY, chrM and contigs using STAR (version 2.5)[108] with parameters –outFilterIntronMotifs RemoveNoncanonicalUnannotated –alignIntronMax 100,000 –outSAMstrandField intronMotif –outSAMunmapped Within –chimSegmentMin 25 –chimJunctionOverhangMin 25. Strand-specific read counts were quantified using Subread (version 1.5.1) 'featureCounts' with parameters -t exon -g gene_id -s 1 -T 6 and used as input to differential gene expression analysis. Read counts were normalized to reads per million per kilobase (RPKM) for each gene. For Granta519-Cas9 ctrl and EBF1-KO samples, expressed genes were determined as genes with >1 RPKM in at least three of the individual libraries. For Granta519-EBF1-FKBP-KI clones 27 and 97, expressed genes were determined as genes with >1 average RPKM of the triplicates per condition in at least three conditions per clone. Pairwise differential gene expression analysis was performed using DEseq2 (ref. 97) with parameters test = 'Wald', betaPrior = F, fitType = 'parametric'. Significance cutoff was abs($\log_2$(fold change)) > 0.5 and FDR < 0.05. Expressed genes in gene-dense and gene-sparse hubs were ranked by averaged RPKM and the top 500 genes of each category were used to conduct Gene Ontology (GO) enrichment analysis. GO sets only enriched in gene-dense or gene-sparse hubs with FDR < 1×10^{-7} were visualized in R (Fig. 1k,l).

ORCA data analysis. *ChrTracer3, QC and imputation*. Raw images were exported as individual.tiff per FOV, step, z-plane and channel using Vutara SRX (no hardware version 7.1.38). Tiff files for each readout were compiled as ConvZscan.dax and ConvZscan.inf files using MATLAB as input for ChrTracer3[31]. ChrTracer3 was followed stepwise for drift correction, spot selection and spot fitting using default parameters except changing the pixel to nm conversion for *xy* and *z* planes. Traces identified in all FOVs per experiment were concatenated and further analysed in R and MATLAB. For each trace, the number of registered steps and brightness (column 'h' in ChrTracer3 output table) were used for quality control. For 30-step walks, traces with five or fewer missing steps were kept. For 36-step walks, the cutoff was six missing steps and for 72-step walks the cutoff was 15.

Distance and contact frequency. Granta519-EBF1-FKBP-KI *MYC* locus: pairwise distances were calculated on unimputed traces per condition (untreated, 6 h dTAG, 24 h dTAG, 6 h washout, 24 h washout) per biological replicate (clone 27 and clone 97). Using the median distance of all neighbouring steps (step 1 to 2, 2 to 3, … 29 to 30) as a cutoff,

the contact frequency vectors of unimputed traces were generated and the Pearson correlations were calculated. After confirmation of >95% correlation between the two replicates, the traces were combined for downstream analyses. More details can be found in Supplementary Table. The median distances across combined traces excluding missing values were used to plot the final distance map per condition (Extended Data Fig. 3). The neighbouring step cutoff was recalculated with combined traces and used to generate contact frequency maps (Fig. 3) and compare enhancer–promoter contact frequencies (Fig. 4). Interaction between *MYC* and super-enhancer E1 was defined as distances between either step 25-7 or 25-8 smaller than cutoffs per condition. The *MYC*-to-super-enhancer-E2 interaction was defined as the distance between step 25-11 smaller than cutoffs per condition. For E1, equally spaced bins were (1–18, 2–19, ..., 8–25, ..., 13–30) or (2–18 (for padding), 1–19, 2–20, ..., 7–25, ..., 12–30) (Fig. 4b). For E2, equally spaced bins were (4–18, 5–19, ..., 11–25, ..., 16–30) (Fig. 4c). Control regions were defined as (6–23, 7–24, 9–26) or (7–23, 8–24, 10–26) for *MYC*-to-E1 and (10–23, 11–24, 13–26) for *MYC*-to-E2 and the contact frequencies were averaged with missing values removed (Fig. 4d,e). Error bars in Fig. 4 are 95% CI of contact frequencies calculated from 1,000 sets of 500 randomly sampled alleles.

DND41 *KLF7* and *ZEB2* loci: pairwise distances were calculated on unimputed traces per condition (GSI-sensitive and GSI-resistant). The median distances across combined traces excluding missing values were used to plot the final distance map per condition (Fig. 6 and Extended Data Fig. 6). A cutoff of 250 nm was used for determining pairwise interaction.

For the DND41 *MYC* locus, pairwise distances were calculated on unimputed traces per condition (GSI-sensitive and GSI-resistant) in two biological replicates and combined. The median distances across combined traces excluding missing values were used to plot the final distance map per condition (Extended Data Fig. 7). The contact frequency matrices were generated using the median distance of all neighbouring steps per condition as cutoffs per condition. *MYC* and super-enhancer TE1 was defined as interacting whenever any distance between step 4 to steps 52, 53 or 54 was smaller than the condition's cutoff. *MYC* and super-enhancer TE2 was defined as interacting whenever any distance between step 4 to steps 65, 66 or 67 was smaller than the condition's cutoff. Error bars in Fig. 7 are 95% CIs of contact frequencies calculated from 1,000 sets of 1,000 randomly sampled alleles.

Clustering and radius of gyration. For the Granta519-EBF1-FKBP-KI *MYC* locus, filtered, imputed alleles from all conditions and replicates were combined and the pairwise distance vectors were calculated as input to *k*-means clustering using R 'kmeans' function with centres = 10 and iter.max = 20. The neighbouring step cutoff was recalculated with combined traces and used to generate contact matrices for each *k*. Interaction maps of each *k* were manually inspected and arranged as in Fig. 3f. The *k*-means clustering was then conducted on each condition and manually inspected to be arranged in the same order as Fig. 3f. Stratification of whether the allele has E1, E2 and *MYC* interactions were determined as described above using the unimputed values of the allele. Error bars in Fig. 4h and Extended Data Fig. 4e–h were CIs calculated from 1,000 sets of 500 randomly sampled alleles. Imputed alleles from all conditions were used for calculation of geometric centre and radius of gyration, respectively defined as $C = \frac{1}{N}(\Sigma_{i=1}^{N} X_i, \Sigma_{i=1}^{N} Y_i, \Sigma_{i=1}^{N} Z_i)$, and $R_g^2 = \frac{1}{N}\Sigma_{i=1}^{N}(r_i - C)^2$, where N is the number of steps of each trace and (X_i, Y_i, Z_i) are the coordinates of step i and $r_i = (X_i, Y_i, Z_i)$ of a trace. The centrality profile for each chromatin trace was generated by calculating the Euclidian distance between each step (X_i, Y_i, Z_i) along the trace from the trace genomic centre C (Fig. 4f).

Polymer simulations. Simulation of loop extrusion was performed using Open2C's polychrom Python library (version 0.1.1)[109] with slight modifications. The simulation framework was divided into two steps: a one-dimensional (1D) step and a 3D step. The 1D step tracks the movement of $c \times 2$ cohesin legs/anchors (c = the number of cohesins) across a polymer consisting of N monomers, where each monomer represents a genomic region of length M. The length in base pairs represented by the polymer can then be calculated as $L = N \times M$. A predefined number of cohesins c can each be either randomly loaded onto any monomer with a uniform probability distribution ('uniform loading'), or loaded onto a specific region/sequence of monomers with uniform probability from which it will extrude ('targeted loading'), these behaviours constitute the modified portion of the polychrom package. Targeted loading was primarily used in the loading scenario to simulate EBF1's loading of cohesin at specific locations, while uniform loading was utilized in the blocking scenario. At each 1D step, the two anchors of the cohesin can take four possible actions: (1) unimpeded cohesin movement, which is defined as translocation of the anchors at positions x_1 and x_2 to their adjacent monomers $x_1 - 1$ and $x_2 + 1$ followed by forming a synthetic chemical bond between monomors occupied by the anchors; (2) unload the entire cohesin, including both anchors, from the polymer with probability $\frac{1}{l}$ where l is the average number of monomers traversed ('lifetime') and load another cohesin in the same manner; (3) become blocked by a blocking element (CTCF or EBF1 as a blocker) at a monomer with probability p_b, which may then release the anchor with probability p_r at subsequent steps; or (4) become stalled against another cohesin anchor, in which case extrusion is also halted, but the lifetime l of the cohesin is reduced by one-tenth ($l_{\text{stalled}} = 0.1 \times l$). The 3D step reads the cohesin positions produced by the 1D step and maps them onto a polymer in 3D space created with OpenMM. The polymer was considered as a self-avoiding walk grown on a cubic lattice, and undergoes energy minimization followed by subsequent steps of cohesin movement as defined above. All thermodynamic and integration parameters were kept as the defaults provided by the polychrom library. The full list of altered simulation parameters distinguishing loading from blocking scenarios can be found in Supplementary Table. The outputs of the 3D steps are the (x, y, z) coordinates of each monomer in the ensemble of simulated polymers, which are used in subsequent analyses to calculate distances and interaction frequencies in Fig. 5.

Materials availability. Plasmids and cell lines generated in this study will be made available upon request.

Reporting summary

Further information on research design is available in the Nature Portfolio Reporting Summary linked to this article.

Data availability

Next-generation sequencing data are deposited and publicly available at the Gene Expression Omnibus under accession number GSE293368. Microscopy data reported in this paper are deposited at OLIVE data portals. All data supporting the findings of this study are available from the corresponding author on reasonable request. Source data are provided with this paper.

Code availability

This paper does not report any original code. Any additional information required to reanalyse the data reported in this paper is available from the corresponding author upon request.

References

91. Grevet, J. D. et al. Domain-focused CRISPR screen identifies HRI as a fetal hemoglobin regulator in human erythroid cells. *Science* **361**, 285–290 (2018).
92. Buenrostro, J. D., Giresi, P. G., Zaba, L. C., Chang, H. Y. & Greenleaf, W. J. Transposition of native chromatin for fast and sensitive epigenomic profiling of open chromatin, DNA-binding proteins and nucleosome position. *Nat. Methods* **10**, 1213–1218 (2013).

93. Beliveau, B. J. et al. OligoMiner provides a rapid, flexible environment for the design of genome-scale oligonucleotide in situ hybridization probes. *Proc. Natl Acad. Sci. USA* **115**, E2183–E2192 (2018).
94. Su, J. H., Zheng, P., Kinrot, S. S., Bintu, B. & Zhuang, X. Genome-scale imaging of the 3D organization and transcriptional activity of chromatin. *Cell* **182**, 1641–59 e26 (2020).
95. Li, H. & Durbin, R. Fast and accurate short read alignment with Burrows–Wheeler transform. *Bioinformatics* **25**, 1754–1760 (2009).
96. Zhang, Y. et al. Model-based analysis of ChIP-Seq (MACS). *Genome Biol.* **9**, R137 (2008).
97. Love, M. I., Huber, W. & Anders, S. Moderated estimation of fold change and dispersion for RNA-seq data with DESeq2. *Genome Biol.* **15**, 550 (2014).
98. Li, H. et al. The Sequence Alignment/Map format and SAMtools. *Bioinformatics* **25**, 2078–2079 (2009).
99. Phanstiel, D. H., Boyle, A. P., Araya, C. L. & Snyder, M. P. Sushi.R: flexible, quantitative and integrative genomic visualizations for publication-quality multi-panel figures. *Bioinformatics* **30**, 2808–2810 (2014).
100. Kent, W. J., Zweig, A. S., Barber, G., Hinrichs, A. S. & Karolchik, D. BigWig and BigBed: enabling browsing of large distributed datasets. *Bioinformatics* **26**, 2204–2207 (2010).
101. Durand, N. C. et al. Juicer provides a one-click system for analyzing loop-resolution Hi-C experiments. *Cell Syst.* **3**, 95–98 (2016).
102. Servant, N. et al. HiC-Pro: an optimized and flexible pipeline for Hi-C data processing. *Genome Biol.* **16**, 259 (2015).
103. Phanstiel, D. H., Boyle, A. P., Heidari, N. & Snyder, M. P. Mango: a bias-correcting ChIA-PET analysis pipeline. *Bioinformatics* **31**, 3092–3098 (2015).
104. Abdennur, N. & Mirny, L. A. Cooler: scalable storage for Hi-C data and other genomically labeled arrays. *Bioinformatics* **36**, 311–316 (2020).
105. Open2C et al. Cooltools: Enabling high-resolution Hi-C analysis in Python. *PLoS Comput. Biol.* **20**, e1012067 (2024).
106. Blondel, V. D., Guillaume, J. L., Lambiotte, R. & Lefebvre, E. Fast unfolding of communities in large networks. *J. Stat. Mech. Theory E*. https://doi.org/10.1088/1742-5468/2008/10/P10008 (2008).
107. van der Weide, R. H. et al. Hi-C analyses with GENOVA: a case study with cohesin variants. *NAR Genom. Bioinform.* **3**, lqab040 (2021).
108. Dobin, A. et al. STAR: ultrafast universal RNA-seq aligner. *Bioinformatics* **29**, 15–21 (2013).
109. Imakaev, M. V., Fudenberg, G. & Mirny, L. A. Modeling chromosomes: beyond pretty pictures. *FEBS Lett.* **589**, 3031–3036 (2015).

Acknowledgements

We thank W. Pear, J. Shi, N. Zolotarev, L. Paruzzo and C. Antony for their helpful discussions and technical advice. We are grateful to K. Lupo for providing critical technical support. We also thank S. Berger for the generous support of the Penn Epigenetics Institute. This work was supported by a Cancer Prevention and Research Institute of Texas grant RR210018 (to G.N.), National Institutes of Health (NIH) grants U01DK112217, R01HL145754, R0AI168240, U01DK127768 and R01AI168136 (to G.V.); and NIH grants U01DK123594, R01CA248041 and R01CA230800 (to R.B.F.).

Author contributions

Conceptualization: Y.Z. and R.B.F. Methodology: Y.Z., A.J., G.V. and R.B.F. Investigation: Y.Z., N.B., R.G., G.V. and R.B.F. Formal analysis: Y.Z., N.B., T.F., S.Y. and R.B.F. Resources and reagents: R.G., J.A., G.N., G.V. and R.B.F. Writing original draft: Y.Z. and R.B.F. Writing review and editing: Y.Z., T.F., N.B., R.G., G.V. and R.B.F. Funding acquisition: R.B.F. and G.V. Supervision: R.B.F. and G.V.

Competing interests

The authors declare no competing interests.

Additional information

Extended data is available for this paper at https://doi.org/10.1038/s41556-025-01827-2.

Supplementary information The online version contains supplementary material available at https://doi.org/10.1038/s41556-025-01827-2.

Correspondence and requests for materials should be addressed to Golnaz Vahedi or Robert B. Faryabi.

Peer review information *Nature Cell Biology* thanks the anonymous reviewers for their contribution to the peer review of this work.

https://doi.org/10.1038/s41556-025-01827-2

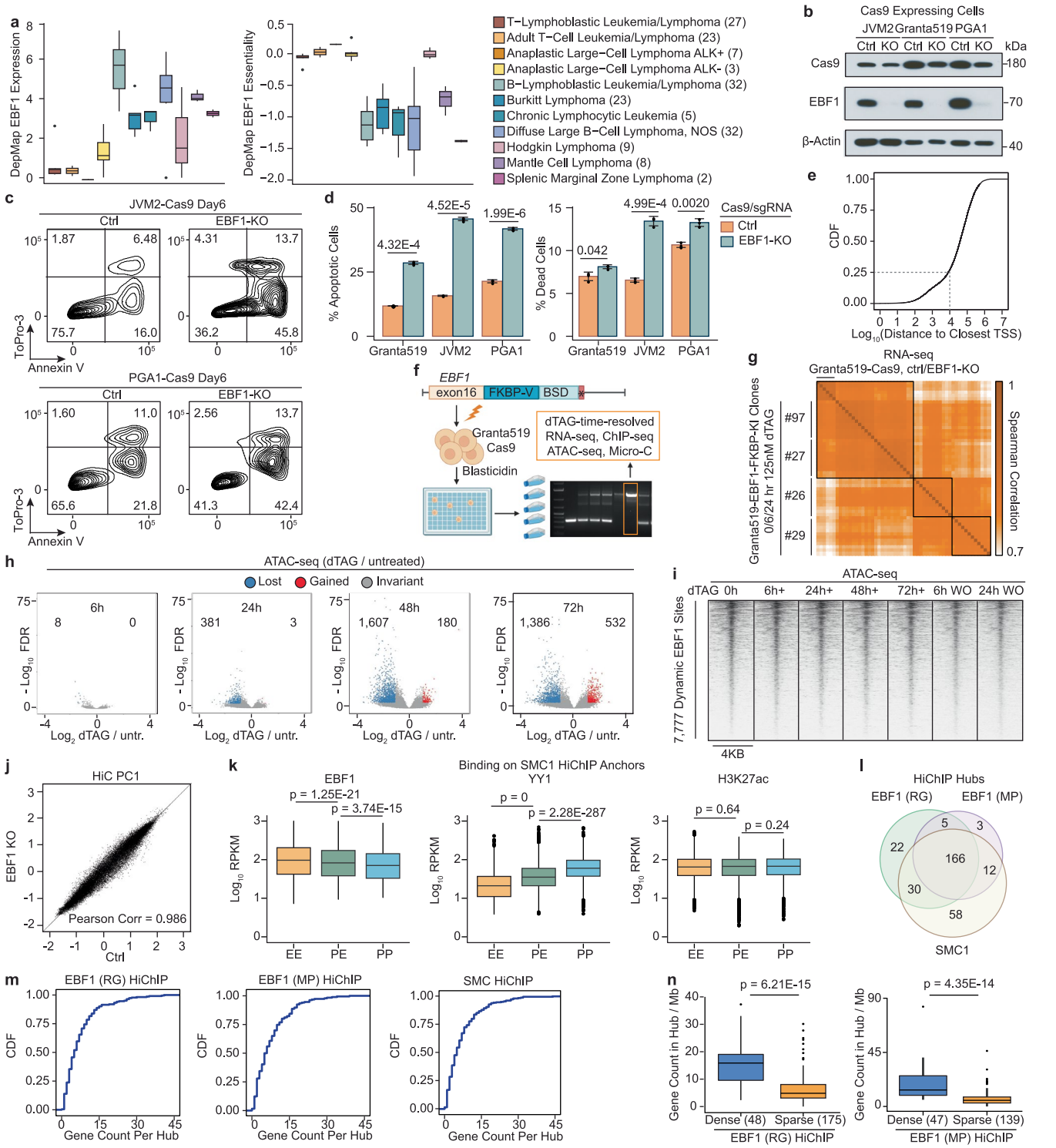

Extended Data Fig. 1 | See next page for caption.

https://doi.org/10.1038/s41556-025-01827-2

Extended Data Fig. 1 | EBF1 is required for MCL growth but not for maintenance of chromatin accessibility or compartments. a, Box-and-whisker plots depicting higher expression (left) and essentiality (right) of EBF1 in Non-Hodgkin B lymphomas compared to T cell leukaemia/lymphoma from DepMap. The number of cell lines are indicated in parentheses. Box-and-whisker plots: centre line, median; box limits, upper (75th) and lower (25th) percentiles; whiskers, 1.5 interquartile range. **b**, Western blotting of EBF1 in Cas9-expressing JVM-2, Granta519 and PGA-1 MCL showing efficient depletion of EBF1 three days after transfection of sgRNA targeting EBF1. β-actin is loading control. **c**, **d**, Flow cytometry plots (**c**) and quantification (**d**) of cell apoptosis and death measured by Annexin V and ToPro-3 staining. Ctrl and EBF1-KO Cas9-expressing MCL cells were sorted three days post lentiviral transduction and cultured for three days. See Supplementary Fig. 1 for gating strategy. Data represent mean ± S.D. of 3 replicates per condition. P value: two-sided t-test. **e**, Cumulative distribution plot (CDF) of distances between each reproducible EBF1 peak to the closest expressed gene TSS in Granta519 showing > 75% EBF1 peaks are located 10 kb away from TSS. **f**, Schematics of knocking in $FKBP^{F36V}$ domain at the stop codon of endogenous EBF1 gene in Granta519-Cas9 cells. Single cell clones were selected with blasticidin and successful insertion of the $FKBP^{F36V}$ cassette was validated with genomic DNA PCR. Clones with efficient EBF1 degradation after $dTAG^{V}$-1 treatment (referred to as dTAG) are used. **g**, Hierarchical clustering of normalized reads (RPKM) from Ctrl and EBF1-KO Granta519-Cas9, and EBF1-FKBP-KI clones 26, 27, 29, 97 with 0, 6, 24-h 125 nM dTAG treatment showing higher similarity of clones 27 and 97 with Granta519-Cas9 transcriptome. **h**, Volcano plot showing ATAC-seq signal fold enrichment (x axis) versus false discovery rate (FDR) (y axis) in Granta519-EBF1-FKBP-KI clone 27 treated with 125 nM dTAG for 6, 24, 48, 72 h compared with untreated cells. Each point depicts an accessible element, colour coded by blue, red, and black based on significantly decreased, increased, or unchanged accessibility in treated cells, respectively. Significance cutoff: FDR < 1E-5 and Log2(fold change) => 1. **i**, Heatmaps displaying overall unchanged normalized accessibility levels at dynamic EBF1-binding sites. Each column of ATAC-seq signals is centred on bona fide EBF1-bound elements per Fig. 1d ± 2 Kb flanking sequences with 50 bp resolution. **j**, Scatterplot of PC1 values of Hi-C contact matrices in Ctrl and EBF1-KO Granta519-Cas9 cells showing largely invariable A/B compartments. **k**, Box-and-whisker plots of EBF1 (left), YY1 (middle) and H3K27ac (right) loading at the promoters (P) and enhancers (E) interacting with significant long-range DNA loops of SMC1 HiChIP in Granta519. EBF1 preferentially binds enhancers, while YY1 preferentially binds promoters. H3K27ac is negative control. EE: n = 11,818; PE: n = 10,739; PP: n = 3,806. Box-and-whisker plots: see panel **a**. FWER-adjusted p values: two-side Wilcoxon rank-sum test. **l**, Venn diagram comparing overlapping of the genomic coordinates of enhancer–promoter hubs in Granta519 SMC1 and EBF1 (RG and MP) HiChIP showing high concordance of hubs identified by three assays. **m**, Cumulative distribution plots showing expressed genes count in each enhancer–promoter hub defined by EBF1 (RG and MP) and SMC1 HiChIP. **n**, Box-and-whisker plots showing higher number of genes per megabase in gene-dense compared to gene-sparse hubs defined by EBF1 HiChIP using RG (left) and MP (right) antibodies. The number of hubs in each group is listed in parentheses. Box-and-whisker plots: see panel **a**. P values: two-sided Wilcoxon rank-sum test. Source numerical data and unprocessed blots are available in Source data.

https://doi.org/10.1038/s41556-025-01827-2

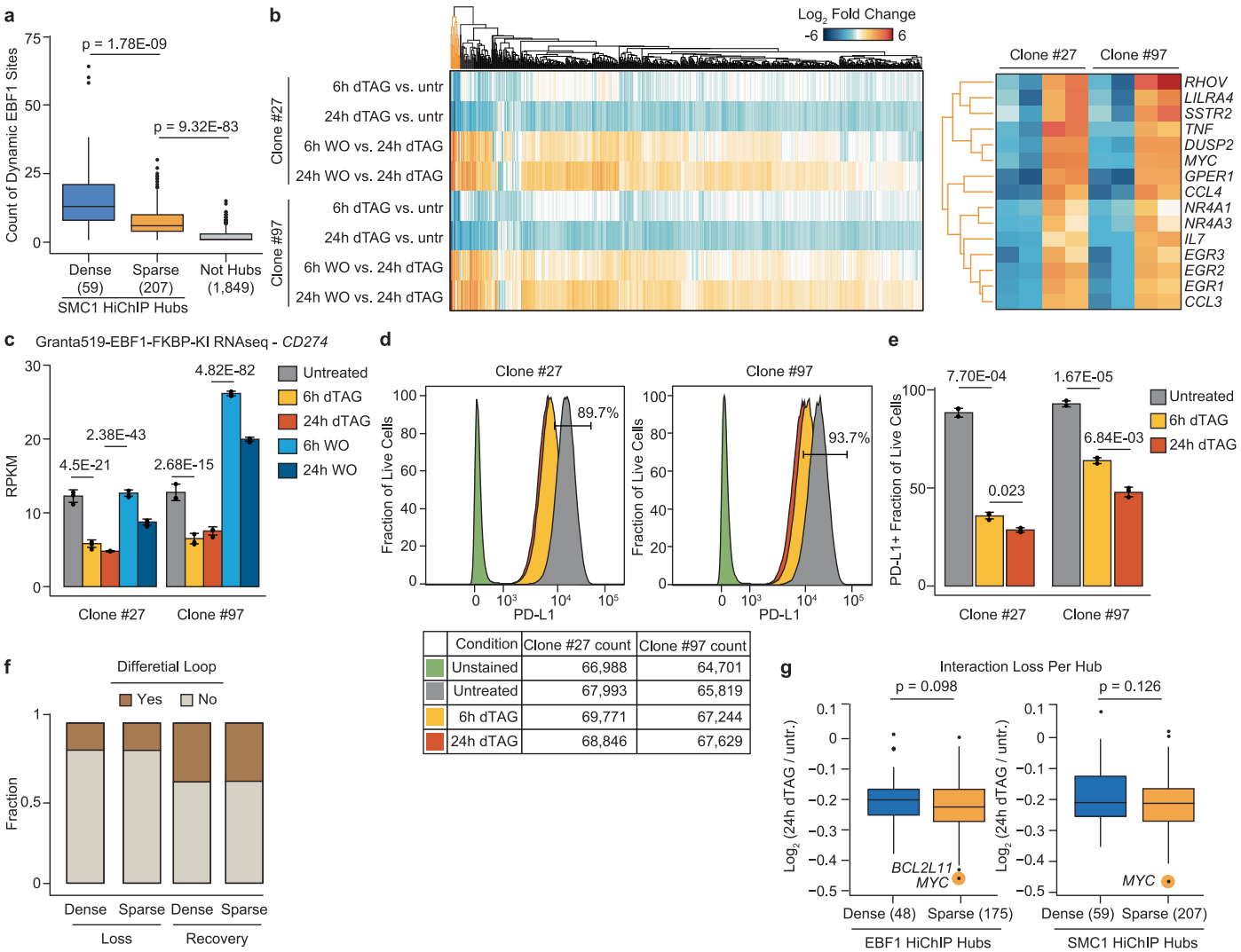

	Condition	Clone #27 count	Clone #97 count
	Unstained	66,988	64,701
	Untreated	67,993	65,819
	6h dTAG	69,771	67,244
	24h dTAG	68,846	67,629

Extended Data Fig. 2 | EBF1 rapidly alters expression of *CD274*, a gene located in a gene-sparse hub. a, Box-and-whisker plots comparing number of EBF1-binding sites in gene-dense, gene-sparse and non-hub regions, as determined with SMC1 HiChIP. The number of hubs in each group is listed in parentheses. Box-and-whisker plots: centre line, median; box limits, upper (75th) and lower (25th) percentiles; whiskers, 1.5 interquartile range. FWER-adjusted p values: two-sided Wilcoxon rank-sum test. **b**, Left: Hierarchical clustering of Log2(fold change) between indicated conditions showing high concordance of differentially expressed genes in clones 27 and 97. Right: Zoom-in of the gene cluster highlighted in yellow in the left panel. **c**, Barplots of normalized RNA-seq reads showing significant *CD274* (encoding PD-L1) down- and upregulation 6 and 24 h after dTAG treatment and washout, respectively, in Granta519-EBF1-FKBP-KI clones 27 and 97. Data represent mean ± S.D. of 3 replicates per condition. FDR from DESeq2. **d**, **e**, Flow cytometry plots (**d**) and quantification (**e**) of PD-L1-positive live cells in clones 27 and 97 showing downregulation of PD-L1 after EBF1 degradation. Lower panel of (**d**) indicates total live cell counts per condition by L/D aqua staining showing cell viability is unaffected by dTAG treatment in 24 h. See Supplementary Figs. 2 and 3 for gating strategy. Data represent mean ± S.D. of 3 replicates per condition. P values: two-sided t-test. **f**, Barplots showing the proportion of enhancer–promoter Micro-C interactions with more than 2-fold interaction frequency changes in gene-dense and gene-sparse hubs after dTAG treatment and washout. **g**, Box-and-whisker plots showing significantly stronger loss of Micro-C interactions among enhancers and promoters 24 h after dTAG treatment in gene-sparse compared to gene-dense hubs as defined by EBF1 (left) and SMC1 (right) HiChIP. Each dot represents the average Log2(fold change) of 24 h washout over 24 h dTAG of interactions in each hub. The number of hubs in each group is listed in parentheses. Box-and-whisker plots: see panel **a**. P values: two-sided Wilcoxon rank-sum test. Source numerical data are available in Source data.

https://doi.org/10.1038/s41556-025-01827-2

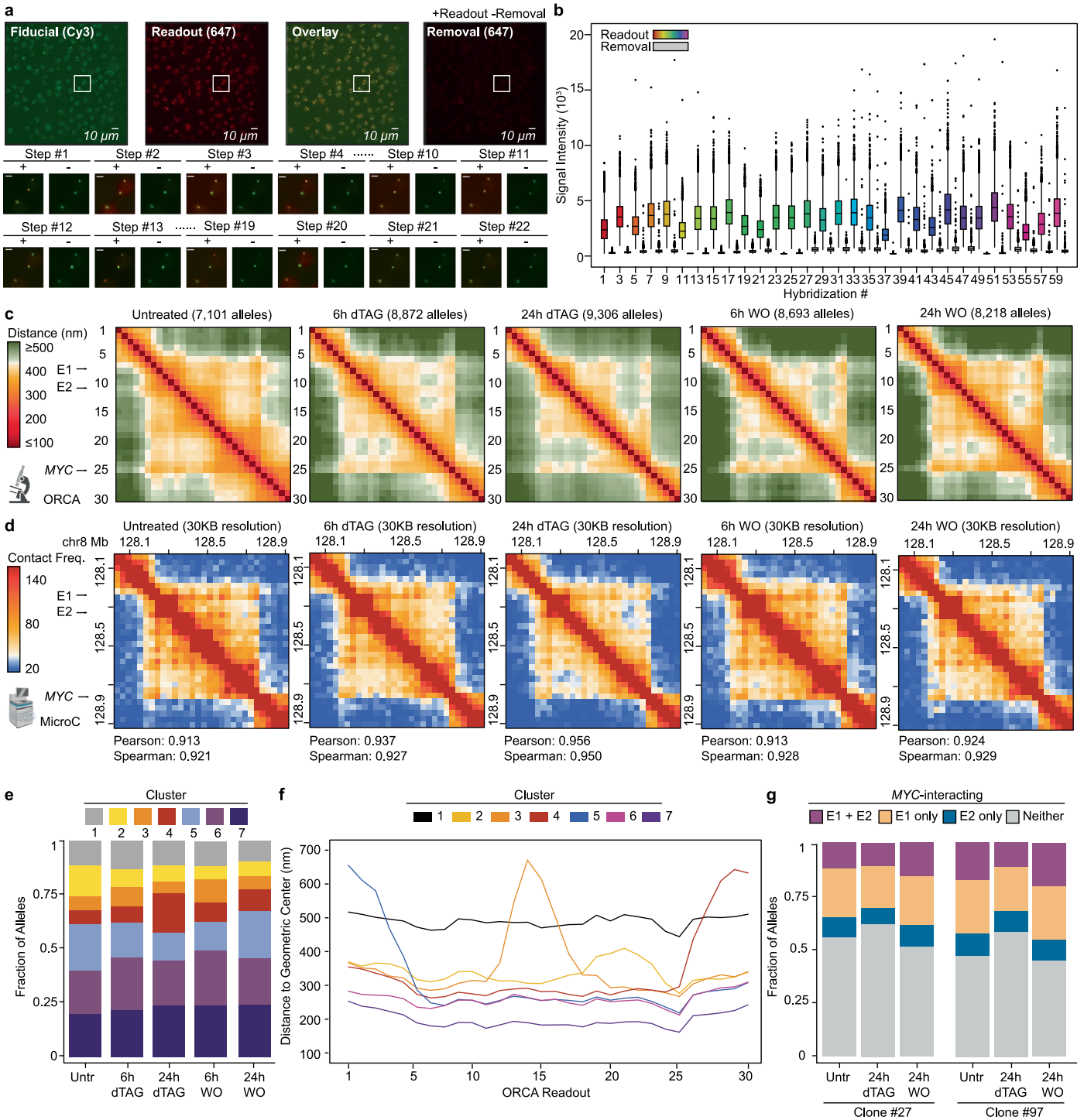

Extended Data Fig. 3 | High quality ORCA chromatin traces show EBF1-dependency of common topological conformations at the *MYC* locus. a, Top: example images of nuclei on a field of view of the hybridization and subsequent removal of the first readout. Bottom: zoomed-in images show the process of hybridization and removal at the indicated steps for example alleles showing consistent signals throughout the experiment. Scale bars on zoomed-in images represent 3 µm. **b**, Box-and-whisker plots of signal intensities (column h in ChrTracer 3 output) at each hybridization and removal of 5,829 unfiltered traces in Granta519 clone 27 24-h dTAG-treated cells indicating strong signal-to-noise ratio. Box-and-whisker plots: centre line, median; box limits, upper (75th) and lower (25th) percentiles; whiskers, 1.5 interquartile range. **c**, Time-course ORCA pairwise distance maps showing gradual increase and decrease of pairwise distances at the *MYC* locus after dTAG treatment and washout. Each point represents the median of pairwise distances between two steps across all alleles. Each condition combines the alleles from clones 27 and 97. Alleles are not imputed, and missing values are excluded from the calculations. **d**, Time-course Micro-C interaction frequency maps of clone 27 at the *MYC* locus at 30 kb resolution to match with the step size of ORCA. Pearson and Spearman correlations of each condition are calculated between vectorized Micro-C and ORCA maps in Fig. 3d. **e**, Barplots showing the fraction of alleles in each of the *MYC* locus common topological conformations per condition. **f**, Distances of each segment to the geometric centres of the traces. The median across all alleles per common topological conformations in Fig. 3f are calculated and plotted for each segment of the *MYC* ORCA experiment. **g**, Barplots showing reproducibility of changes in fraction of alleles with *MYC*-E1-E2, only *MYC*-E1, only *MYC*-E2 or no *MYC* promoter–enhancer interaction (Neither) per condition in clones 27 and 97. Source numerical data are available in Source data.

https://doi.org/10.1038/s41556-025-01827-2

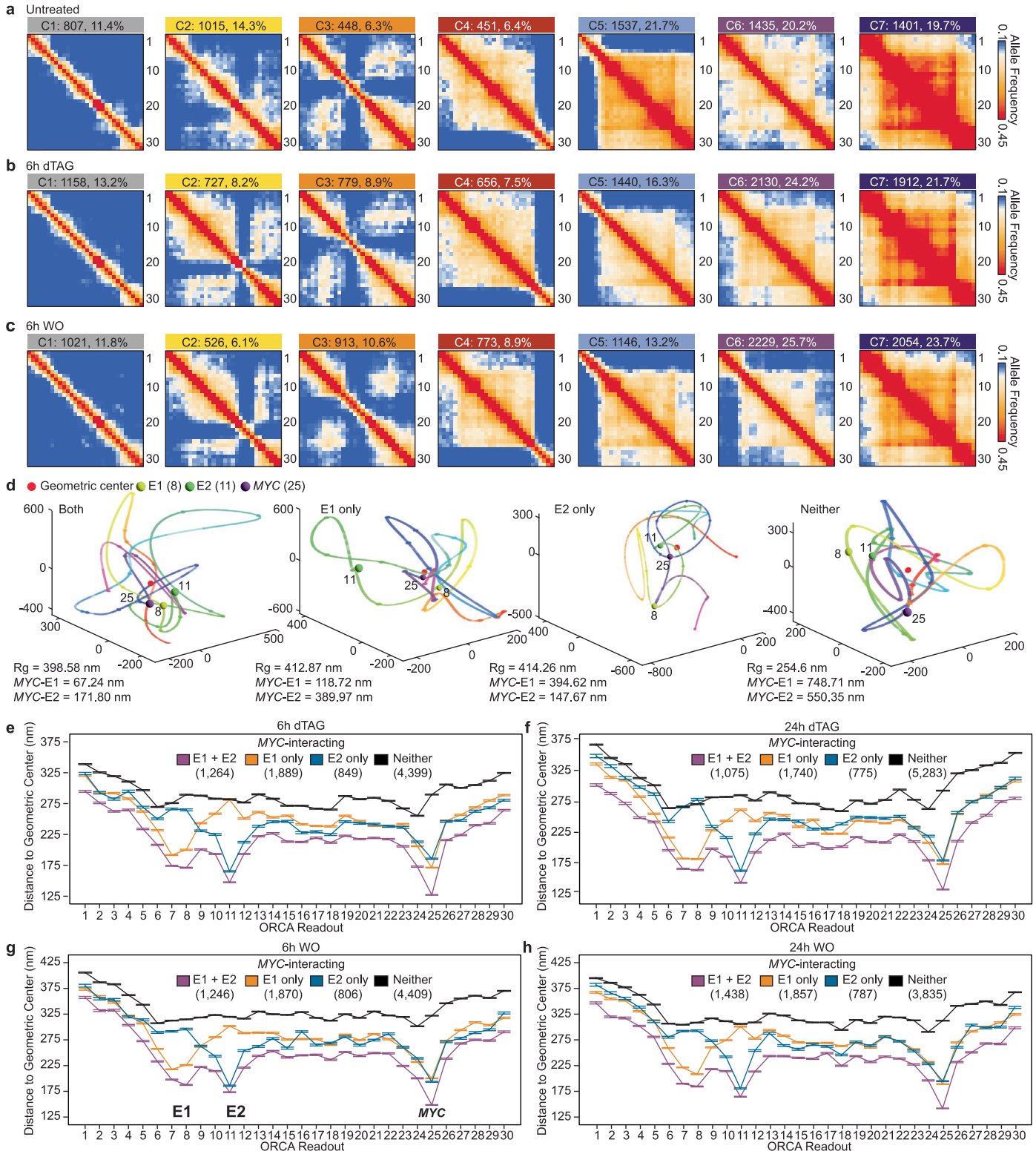

Extended Data Fig. 4 | Time-course ORCA data in MCL show interaction of the *MYC* promoter and super-enhancers at the local geometric centres. a–**c**, Allele frequency maps of traces for each of the 7 common topological conformations of the *MYC* locus in untreated (**a**), 6-h dTAG-treated (**b**) and 6-h dTAG washout (**c**) showing reproducibility of the observed conformations. Clustering and calculation of frequencies are performed on pairwise distances matrices of imputed alleles. **d**, Example reconstructed chromatin traces for alleles with *MYC*-E1-E2 three-way interaction, *MYC*-E1 interaction, *MYC*-E2 interaction and no interaction emphasizing the central positioning of interacting elements. Note that the allele with no *MYC*, E1, E2 interactions has the smallest radius of gyration among the examples. **e**–**h**, Distances of each segment to the geometric centres of the traces with *MYC*-E1-E2, only *MYC*-E1, only *MYC*-E2 or no *MYC* promoter–enhancer interaction (Neither). The median values of stratified alleles are calculated and plotted for each segment of the ORCA experiment in 6-h dTAG-treated (**e**), 24-h dTAG-treated (**f**), 6-h dTAG washout (**g**) and 24-h dTAG washout (**h**) cells. Number of alleles in each category is indicated in parentheses. Each point represents the median centrality calculated from 500 randomly sample alleles with a total of 1,000 rounds of random sampling per condition. Error bars show 95% confidence interval from bootstrapping. Source numerical are available in Source data.

https://doi.org/10.1038/s41556-025-01827-2

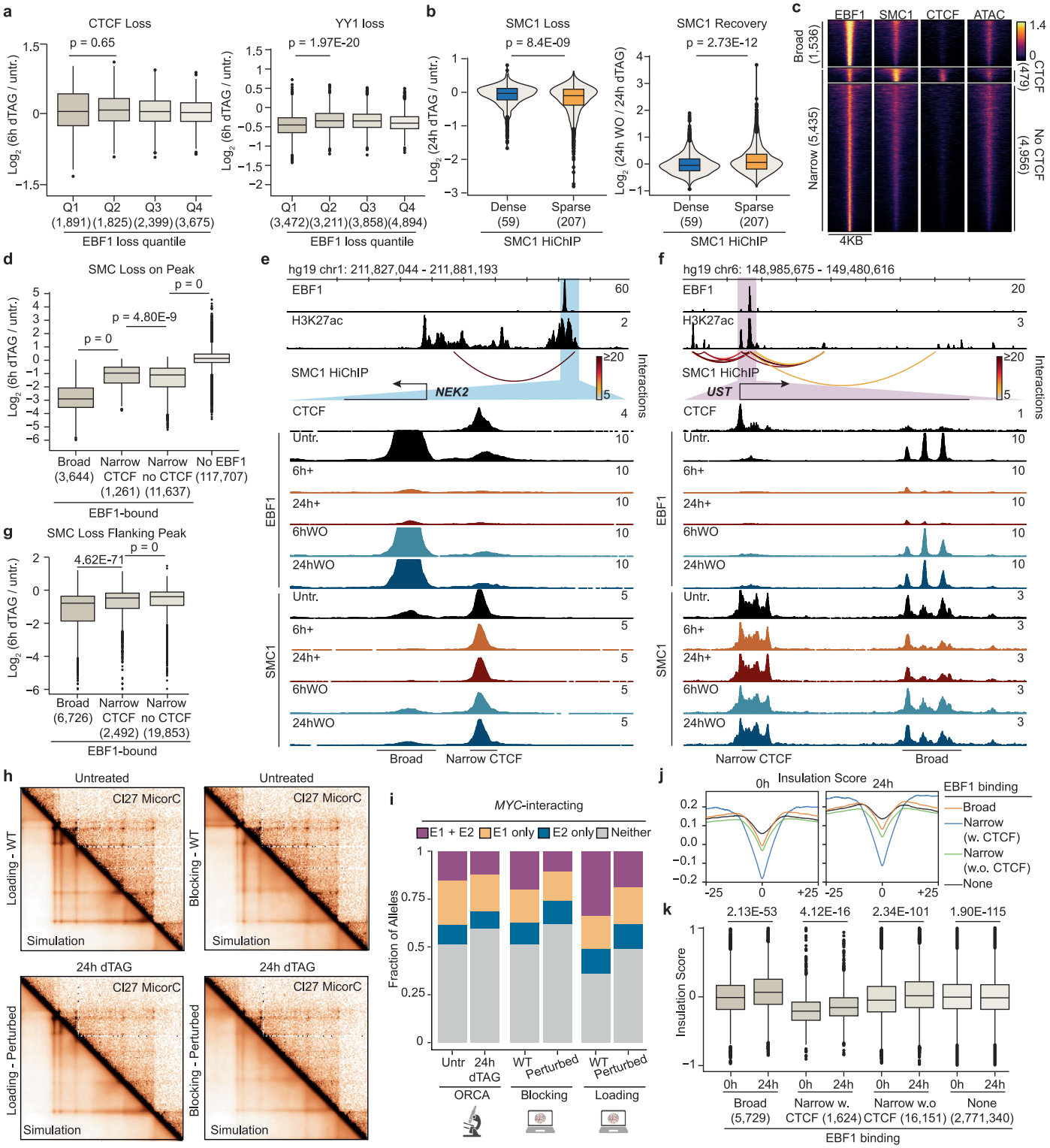

Extended Data Fig. 5 | See next page for caption.

https://doi.org/10.1038/s41556-025-01827-2

Extended Data Fig. 5 | EBF1 changes SMC1 but not CTCF and YY1 chromatin binding in MCL. a, Box-and-whisker plots showing limited correlation between CTCF (left) and YY1 (right) ChIP-seq signals in 6 h dTAG treatment (left) and washout (right) per quartile of EBF1 loading changes 6 h after dTAG treatment. The number of binding sites in each category is listed in parentheses. Box-and-whisker plots: centre line, median; box limits, upper (75th) and lower (25th) percentiles; whiskers, 1.5 interquartile range. P values: two-sided Wilcoxon rank-sum test. **b**, Box-and-whisker and violin plots comparing differential SMC1 ChIP-seq signals in 24 h dTAG treatment (left) and washout (right) at SMC1 peaks located in gene-sparse and gene-dense hubs. The number of hubs in each category is listed in parentheses. Box-and-whisker plots: see panel **a**. P values: two-sided Wilcoxon rank-sum test. **c**, Heatmaps showing broad and focal EBF1-binding sites with a small subset co-occupied by CTCF. Clusters are generated and plotted with deepTools. **d**, Box-and-whisker plots showing stronger loss of SMC1 levels at broad EBF1-binding sites 6 h after dTAG treatment. EBF1-binding sites as grouped per (**c**). The number of binding sites in each category is listed in parentheses. Box-and-whisker plots: see panel **a**. FWER-adjusted p values: two-sided Wilcoxon rank-sum test. **e**, **f**, Top three genomic tracks showing EBF1 and H3K27ac ChIP-seq as well as SMC1 HiChiP at *NEK2* (**e**) and *UST* (**f**) loci in untreated cells showing examples of broad and narrow EBF1-binding sites. Lower genomic tracks showing zoomed-in EBF1, SMC1, and CTCF biding sites at *NEK2* (**e**) and *UST* (**f**) loci in the noted conditions demonstrating marked EBF1-dependency of SMC1 levels at the broad compared to narrow EBF1-binding sties, and no change at the CTCF sites. **g**, Box-and-whisker plots showing significant reduction in SMC1 levels at the broad EBF1-binding sites compared to narrow EBF1-binding sites with or without CTCF. EBF1 peaks ±1,500 bp flanking sequences are considered. The number of binding sites in each category is listed in parentheses. Box-and-whisker plots: see panel **a**. FWER-adjusted p values: two-sided Wilcoxon rank-sum test. **h**, Side-by-side comparison of Micro-C interaction maps from Fig. 3d and polymer simulation interaction frequency maps under loop-extrusion factor loading (left) and blocking (right) models from Fig. 5e, f in EBF1 wild-type (top row) and EBF1-degraded (perturbed) (bottom row) conditions. **i**, Barplots showing fraction of traced chromatins with *MYC* interacting with E1, E2, both E1 and E2 (E1 + E2) or neither in Granta519 ORCA data and simulated polymers with loop-extrusion factor loading and blocking models. **j**, **k**, Pileup plots (**j**) and Box-and-whisker (**k**) plots showing significant reduction in insulation potential at broad EBF1-binding sites 24 h after dTAG treatment compared to no EBF1, narrow EBF1 with CTCF, and narrow EBF1 without CTCF sites. The number of genomic bins in each category is listed in parentheses. Box-and-whisker plots: see panel **a**. FWER-adjusted p values: two-sided Wilcoxon rank-sum test. Source numerical data are available in Source data.

https://doi.org/10.1038/s41556-025-01827-2

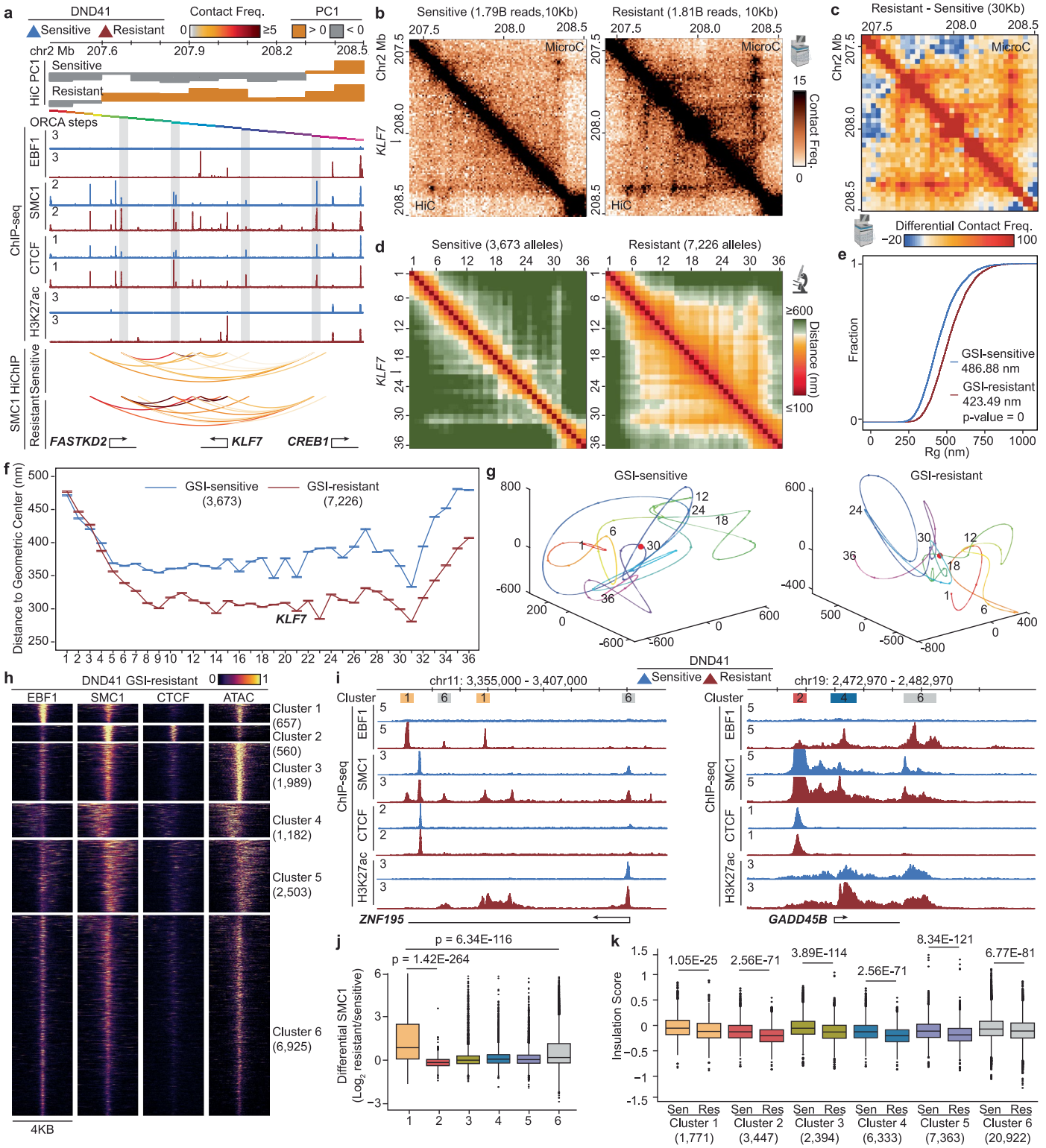

Extended Data Fig. 6 | See next page for caption.

https://doi.org/10.1038/s41556-025-01827-2

Extended Data Fig. 6 | EBF1 binds and activates *KLF7* promoter without changing its local radial positioning in GSI-resistant T-ALL. a, ChIP-seq tracks showing gain of active histone marks H3K27ac, EBF1, CTCF and SMC1 at *KLF7* locus in GSI-resistant DND41. Normalized SMC1 HiChIP arches showing gain of interactions in GSI-resistant DND41. The PC1 values of Hi-C contact correlation matrices in GSI-sensitive and GSI-resistant cells showing shift from B (<0) to A (>0) compartment. Rainbow-coloured bars indicate the 36 steps of ORCA experiments. Bottom track indicates the positions of expressed genes. **b**, Normalized Micro-C (top) and Hi-C (bottom) interaction frequency maps showing gain of interactions at the *KLF7* locus in GSI-resistant (right) compared to GSI-sensitive (left) DND41. **c**, Differential (GSI-resistant minus GSI-sensitive) normalized Micro-C interaction maps with 30 kb resolution matching ORCA at the *KLF7* locus showing gain of stripes in GSI-resistant DND41. **d**, ORCA pairwise distance maps of *KLF7* chromatin traces in GSI-sensitive (left) and GSI-resistant (right) DND41. Each point represents the median of pairwise distances between two segments across all alleles. Alleles are not imputed, and missing values are excluded from the calculation. **e**, Cumulative distributions of radius of gyration of *KLF7* chromatin traces in GSI-sensitive and GSI-resistant DND41 showing overall compaction of the *KLF7* locus in GSI-resistant cells. P value: two-sided Kolmogorov–Smirnov test. **f**, Distances of each segment to the geometric centres of the chromatin traces of *KLF7* locus in GSI-sensitive and GSI-resistant DND41. The median values of chromatin traces are calculated and plotted for each ORCA segment in GSI-sensitive and GSI-resistant cells. The number of alleles in each condition is indicated in parentheses. Error bars show 95% confidence interval from bootstrapping. Note lack of preferential positioning of the *KLF7* promoter (step 21) at the geometric centres of alleles in GSI resistance. **g**, Example reconstructed chromatin traces for alleles in GSI-sensitive (left) and GSI-resistant (right) *KLF7* emphasizing lack of central positioning of the gene promoter. **h**, Heatmaps showing broad and focal EBF1-binding sites in GSI-resistant DND41 with a small subset co-occupied by CTCF. Number of binding sites in each category is indicated in parentheses. Clusters are generated and plotted with deepTools. **i**, Genome tracks of EBF1, SMC1, CTCF and H3K27ac ChIP-seq in GSI-sensitive (blue) and GSI-resistant (red) DND41 at *ZNF195* (left) and *GADD45B* (right) loci showing examples of EBF1-bound elements for clusters noted in (**h**). **j**, Box-and-whisker plots showing Log2(fold change) of GSI-resistant vs GSI-sensitive SMC1 loading at each of the six clusters of EBF1-binding sites in (**h**). The number of binding sites as in panel **h**. Box-and-whisker plots: centre line, median; box limits, upper (75th) and lower (25th) percentiles; whiskers, 1.5 interquartile range. FWER-adjusted p values: two-sided Wilcoxon rank-sum test. **k**, Box-and-whisker plots showing gain of insulation potentials in GSI resistance at each of the six clusters of EBF1-binding sites per (**h**). The number of genomic bins in each category is listed in parentheses. Box-and-whisker plots: see panel **j**. FWER-adjusted p values: two-sided Wilcoxon rank-sum test. Source numerical data are available in Source data.

https://doi.org/10.1038/s41556-025-01827-2

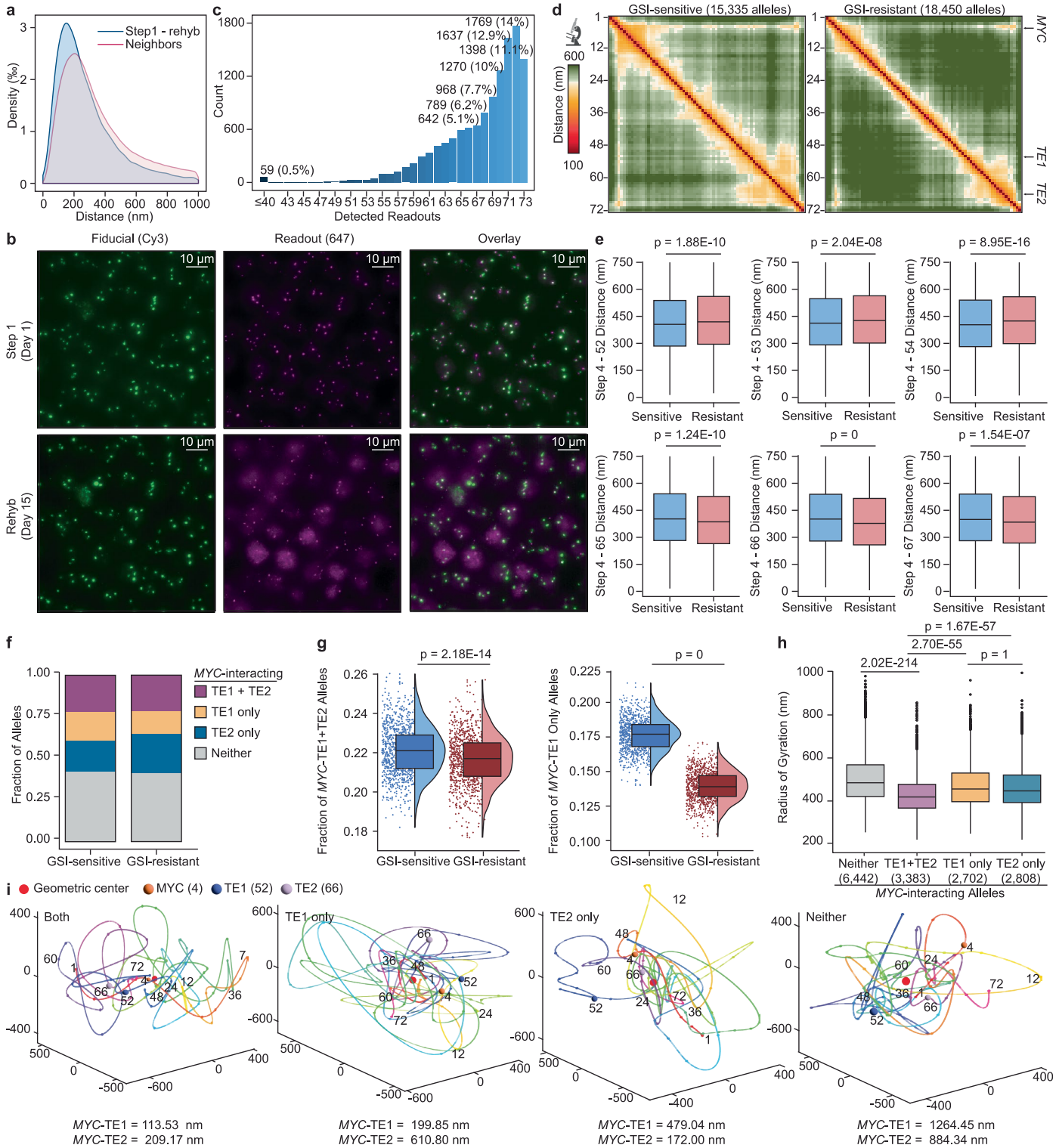

Extended Data Fig. 7 | See next page for caption.

https://doi.org/10.1038/s41556-025-01827-2

Extended Data Fig. 7 | High-quality 72-step tracing of the *MYC* locus in DND41 shows EBF1-dependency of *MYC* three-way interactions with its super-enhancers. a, Distributions of distances between all neighbouring steps (red), and between step 1 and step 73 which is the rehybridization of readout 1 at the end of 15-day ORCA experiment in GSI-sensitive DND41 (blue) showing intact and immobile chromatin during the experiment. **b**, Example field of view showing comparable signal levels in fiducial and readout channels at step 1 and 73 (that is rehybridization of readout 1). **c**, Barplots showing distribution of allele counts with more than half of the readouts detected including rehybridization. **d**, ORCA pairwise distance maps of *MYC* chromatin traces in GSI-sensitive (left) and GSI-resistant (right) DND41. Each point represents the median of pairwise distances between two segments across all alleles. Alleles are not imputed, and missing values are excluded from the calculation. **e**, Box-and-whisker plots showing increased pairwise distances between *MYC* (step 4) and TE1 (steps 52–54), and decreased pairwise distances between *MYC* (step 4) and TE2 (steps 65–67) in $n = 18{,}450$ GSI-resistant DND41 alleles compared to $n = 15{,}335$ GSI-sensitive alleles. Box-and-whisker plots: centre line, median; box limits, upper (75th) and lower (25th) percentiles; whiskers, 1.5 interquartile range. P values: two-sided Wilcoxon rank-sum test. **f**, Barplots showing fraction of alleles with *MYC* interacting with TE1, TE2, both TE1 and TE2 (TE1 + TE2) or neither in GSI-sensitive and GSI-resistant DND41. **g**, Box-and-whisker and violin plots showing decrease in allele frequency with *MYC*–TE1-TE2 (left) and *MYC*-TE1 (right) interactions in GSI-resistant DND41. Each point represents the allele frequencies calculated from 1,000 randomly sampled alleles with a total of 1,000 rounds of random sampling per condition. Box-and-whisker plots: see panel **e**. FWER-adjusted p values: two-sided Wilcoxon rank-sum test. **h**, Box-and-whisker plots showing distributions of radius of gyration of alleles with *MYC*-TE1-TE2, only *MYC*-TE1, only *MYC*-TE2 or no *MYC* promoter–enhancer interaction (Neither) in GSI-sensitive DND41. The number of alleles in each category is indicated in parentheses. Box-and-whisker plots: see panel **e**. FWER-adjusted p values: two-sided Wilcoxon rank-sum test. **i**, Example reconstructed chromatin traces for alleles with *MYC*-TE1-TE2 three-way or only *MYC*-TE1 pairwise interactions from GSI-sensitive DND41, and only *MYC*-TE2 interaction or no promoter–enhancer interactions (Neither) from GSI-resistant DND41 emphasizing the central positioning of interacting elements. Source numerical data are available in Source data.

https://doi.org/10.1038/s41556-025-01827-2

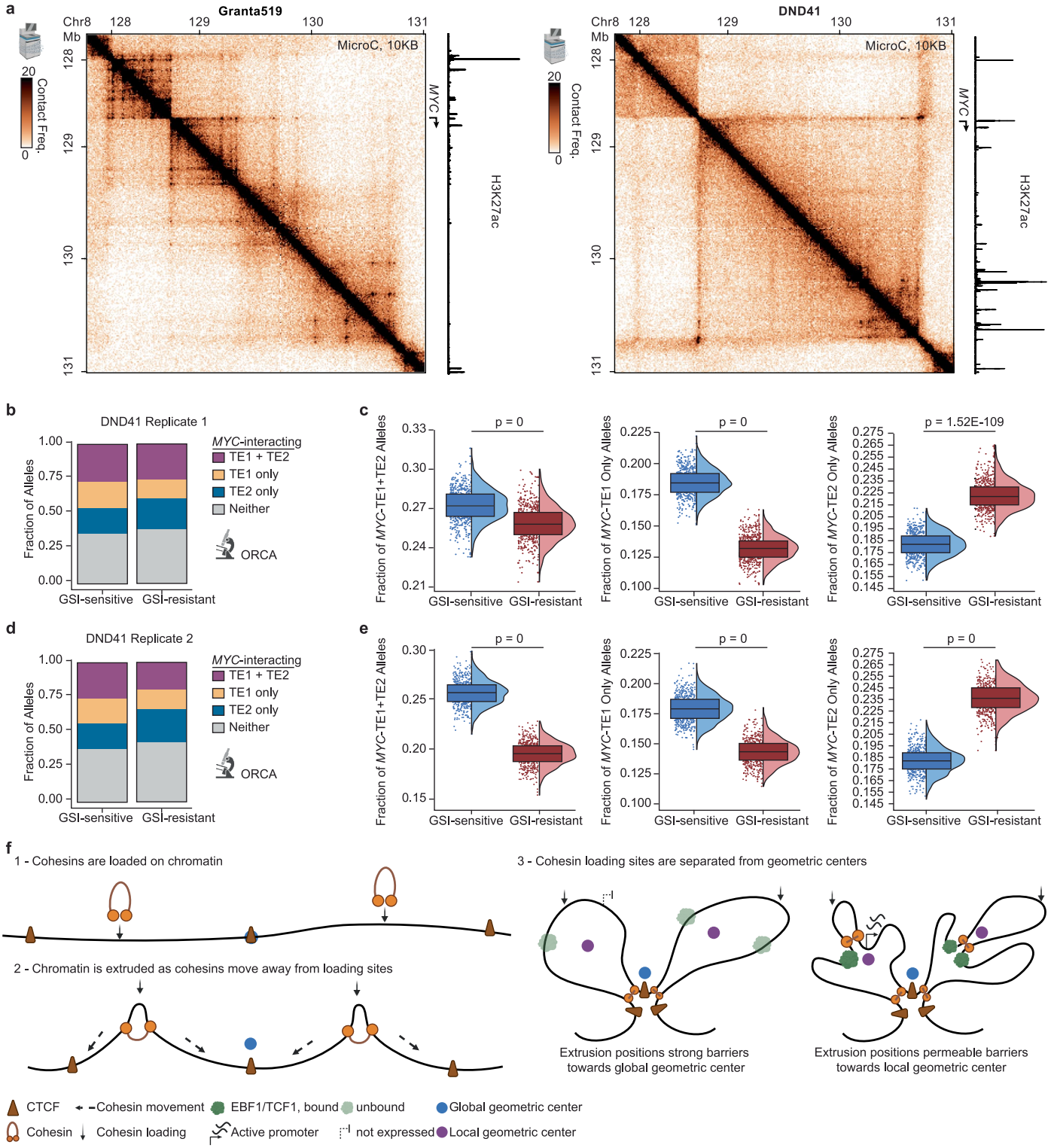

Extended Data Fig. 8 | Model showing separation of loop-extrusion factor loading sites and proximity of extrusion barriers to local geometric centres of folded chromatin. a, H3K27ac ChIP-seq tracks and Micro-C normalized interaction maps at the 3 Mb region flanking the *MYC* promoter in MCL Granta519 and T-ALL DND41 cells depicting lineage-restricted chromatin activity and structures. **b**, Barplots showing fraction of alleles with *MYC* interacting with TE1, TE2, both TE1 and TE2 (TE1 + TE2) or neither in GSI-sensitive and GSI-resistant DND41 biological replicate #1. **c**, Box-and-whisker and violin plots showing decrease in allele frequency with *MYC*-TE1-TE2 (left), decrease in allele frequency with *MYC*-TE1 (middle) interactions and increase in allele frequency with only *MYC*-TE2 (right) interaction in GSI-resistant DND41 biological replicate #1. Each point represents the allele frequencies calculated from 1,000 randomly sampled alleles with a total of 1,000 rounds of random sampling per condition. FWER-adjusted p values: two-sided Wilcoxon rank-sum test. **d**, **e**, same as b, c in DND41 biological replicate #2. **f**, Schematics showing: 1- unfolded chromatin with three strong loop-extrusion barriers (that is CTCF-bound elements), and two sites of loop-extrusion factor loading (that is cohesin); 2- chromatin is extruded as cohesin molecules move along the chromatin away from their loading sites; 3-left- loop extrusion is blocked by CTCF form two segregated domains and positions strong CTCF-bound elements close to the global geometric centre of entire chromatin; 3-right- Loop extrusion is blocked by permeable barriers (for example EBF1-bound elements) positions these sites close to the local geometric centres of two segregated domains. Source numerical data are available in Source data.

https://doi.org/10.1038/s41556-025-01827-2

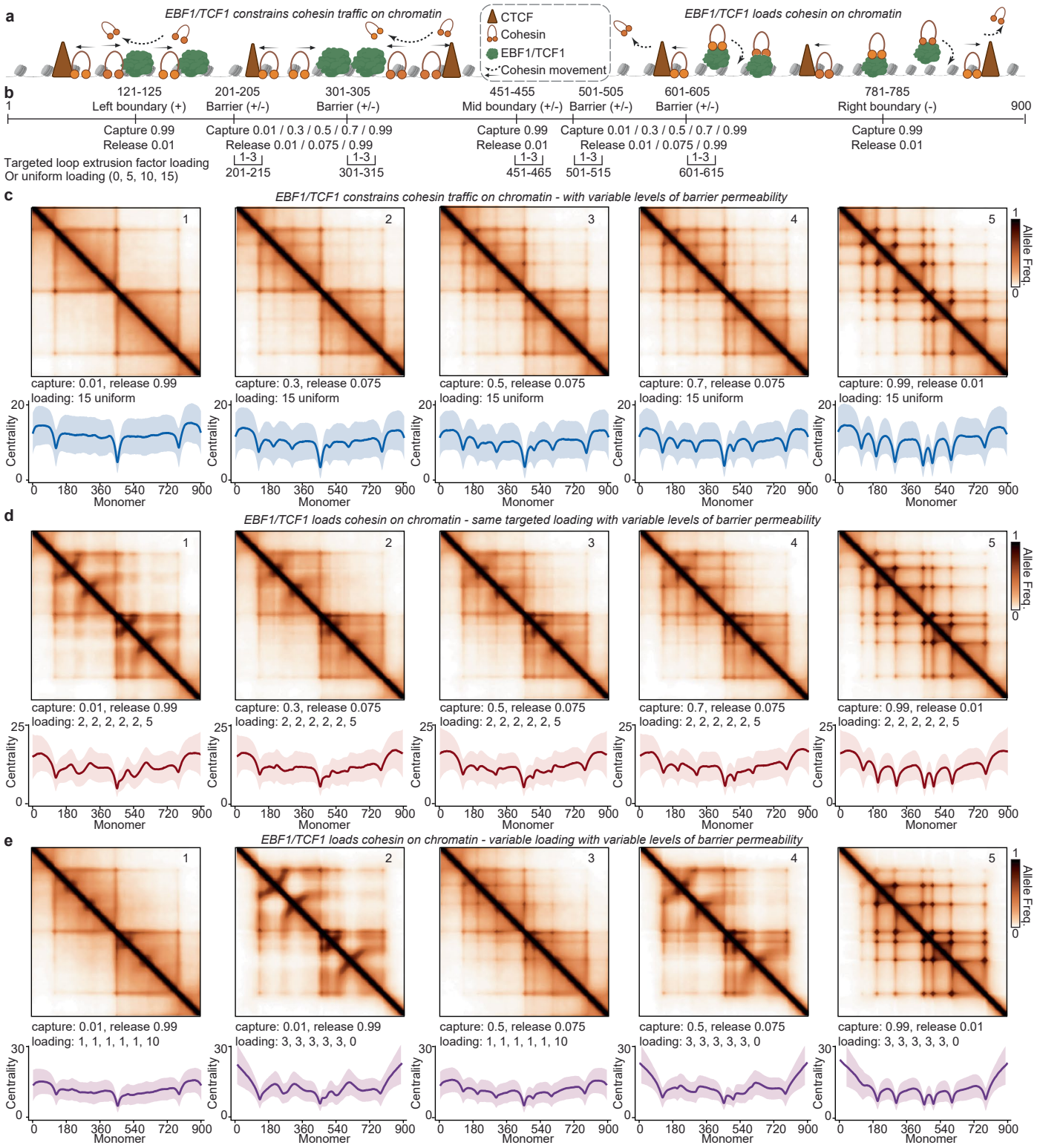

Extended Data Fig. 9 | See next page for caption.

https://doi.org/10.1038/s41556-025-01827-2

Extended Data Fig. 9 | Extruder's permeable barriers, but not loaders, position their bound segments to the locus geometric centres. a, Left: schematic depicting transcription factors (for example EBF1 and TCF1) serving as permeable barriers to loop-extrusion factor (that is cohesin) movement on chromatin. Right: schematic depicting transcription factors (for example EBF1 and TCF1) serving as loaders of loop-extrusion factor (that is cohesin) on chromatin. **b**, Schematic depicting the design of polymer simulation. For each simulated scenario, 10,000 polymers consisting of 900 monomers were generated. Loop-extrusion factors (LEFs) were either uniformly loaded across the polymer or specifically loaded at selected ranges of monomers. A total of 15 LEFs were maintained across all scenarios. The strength of barriers was determined by LEF capture/release probabilities. Strong barriers (0.99 capture, 0.01 release) simulating CTCF-bound boundaries were placed at monomer 121-125 with forward orientation, at 781-785 with reverse orientation, and at monomer 451-455 with both orientations to mimic CTCF motifs. Intra-TAD elements, simulated with various degrees of barrier strength, were designated at 201-205, 301-305, 501-505 and 601-605 monomers. **c**, Stronger barriers are placed closer to the local geometric centres of simulated polymers with all uniformly loaded LEFs. Left to right: allele frequency maps (top row, median across all polymers) and centrality profiles (bottom row, median ± SD) of simulated polymers with low to high capture probability and high to low release probabilities depicting increasingly stronger intra-TAD barriers. Note that when no intra-TAD barrier is present (sub-panel 1), uniformly loaded LEFs are only blocked at the left/mid/right strong barriers forming TAD-like structures and these three regions were closest to the geometric centres of the polymers. As intra-TAD barriers become stronger (sub-panel 2-4), they more frequently block LEFs, forming stripes and sub-TADs similar to Micro-C experimental data and on average decrease their distances to the polymeric geometric centres similar to ORCA experimental data. When barriers become impermeable (sub-panel 5), unusually intense point-to-point contacts occur, and all barriers collapse at the geometric centres. **d**, Stronger barriers neutralize the separation of polymeric geometric centres by targeted loading of LEFs. Left to right: allele frequency maps (top row, median across all polymers) and centrality profiles (bottom row, median ± SD) of simulated polymers with the same barrier strength as in (**c**), but with 2 LEFs loaded at each designated regions in (**b**) and 5 uniformly loaded LEFs. Note that when no intra-TAD barrier is present (sub-panel 1), LEF loading sites exhibit jet-like features on allele frequency map, and are separated from the polymeric geometric centres. As the barriers become stronger near LEF loading sites (sub-panel 2-4), jet-like features are attenuated and stripes and sub-TADs become more prominent. When barriers become impermeable (sub-panel 5), polymers become similar to the matching scenario in (**c**). **e**, More LEFs lead to further separation of targeted loading regions from the polymeric geometric centres. Left to right: when no intra-TAD barrier is present and LEFs are reduced to 1 at targeted regions (sub-panel 1), jet-like features are still present compared to (**c**), but less prominent compared to (**d**). On the contrary, increasing LEFs to 3 at each targeted loading region and reducing uniformly loaded LEF to 0 (sub-panel 2) eliminates intra-TAD interactions, accentuates jet-like features, and increases separation of LEF-loaded regions from the polymeric geometric centres. Similar observations can be made when permeable (sub-panel 3, 4) barriers exist near preferentially loading sites with 1 or 3 LEFs per site. When barriers become impermeable (sub-panel 5), polymers become similar to the matching scenarios in (**c**) and (**d**). Note that when uniformly loaded LEFs are absent (sub-panel 2, 4, 5), LEFs are constrained within the left/right strong boundaries, resulting in lack of interactions at the two ends of the polymers on allele frequency maps and these regions are placed furthest from the polymeric geometric centres. Top row: allele frequency maps, median across all polymers. Bottom row: centrality profiles, median ± SD.

nature portfolio

Corresponding author(s): Robert Faryabi
Last updated by author(s): 10/12/2025

Reporting Summary

Nature Portfolio wishes to improve the reproducibility of the work that we publish. This form provides structure for consistency and transparency in reporting. For further information on Nature Portfolio policies, see our Editorial Policies and the Editorial Policy Checklist.

Statistics

For all statistical analyses, confirm that the following items are present in the figure legend, table legend, main text, or Methods section.

n/a	Confirmed
☐	☒ The exact sample size (*n*) for each experimental group/condition, given as a discrete number and unit of measurement
☐	☒ A statement on whether measurements were taken from distinct samples or whether the same sample was measured repeatedly
☐	☒ The statistical test(s) used AND whether they are one- or two-sided *Only common tests should be described solely by name; describe more complex techniques in the Methods section.*
☒	☐ A description of all covariates tested
☐	☒ A description of any assumptions or corrections, such as tests of normality and adjustment for multiple comparisons
☐	☒ A full description of the statistical parameters including central tendency (e.g. means) or other basic estimates (e.g. regression coefficient) AND variation (e.g. standard deviation) or associated estimates of uncertainty (e.g. confidence intervals)
☐	☒ For null hypothesis testing, the test statistic (e.g. *F*, *t*, *r*) with confidence intervals, effect sizes, degrees of freedom and *P* value noted *Give P values as exact values whenever suitable.*
☒	☐ For Bayesian analysis, information on the choice of priors and Markov chain Monte Carlo settings
☐	☒ For hierarchical and complex designs, identification of the appropriate level for tests and full reporting of outcomes
☐	☒ Estimates of effect sizes (e.g. Cohen's *d*, Pearson's *r*), indicating how they were calculated

Our web collection on statistics for biologists contains articles on many of the points above.

Software and code

Policy information about availability of computer code

Data collection

Data collection was done with experimental procedures and does not involve code.

Data analysis

QUANTIFICATION AND STATISTICAL ANALYSIS

The statistical significance of differences between measurements was determined by Wilcoxon rank sum test using R (version 3.6.1) wilcox.test function and FWER-adjusted for more than one test, unless otherwise stated. Statistical details of experiments can be found in figure legends. No statistical method was used to predetermine sample size. No data were excluded from the analyses. The experiments were not randomized. The Investigators were blinded to allocation during ORCA data analysis. Visualizations were done with R.

Definition of regulatory elements

The following definitions of regulatory elements were used throughout the manuscript. Promoters: promoters were defined as ± 2.5 kilobases (Kb) from the transcription start site (TSS) of each expressed gene. Enhancers: enhancers were defined as H3K27ac peaks excluding the ones overlapping with promoters.

Gene annotation

A total of 2,828,317 Ensembl transcripts in GRCh37.75 assembly were downloaded in gtf format. For each Ensembl gene id (ENSG), the longest transcript (ENST) was used to assign a unique transcriptional start site and gene position. After exclusion of genes annotated as rRNA or on chromosome M, 57,209 gene annotations were used in RNA-seq analysis.

ATAC-seq data analysis

Alignment

Reads from ATAC-seq experiments were trimmed with Trim Galore (version 0.4.1) with parameters -q 15 --phred33 --gzip --stringency 5 -e 0.1 --length 20. Trimmed reads were aligned to the Ensembl GRCh37.75 primary assembly including chromosomes 1-22, chrX, chrY, chrM and contigs using BWA (version 0.7.13)94 with parameters bwa aln -q 5 -l 32 -k 2 -t 6. Paired-end reads were grouped with bwa sampe -P -o 1000000. Reads mapped to contigs, ENCODE blacklist and marked as duplicates by Picard (version 2.1.0) were discarded and the remaining reads were used in downstream analyses and visualization.

Peak calling and Differential accessibility analysis

Peaks in each aligned replicate were identified using MACS2 (version 2.0.9)95 with parameters --nomodel --nolambda --format=BAM -g hs -p 1E-5 --bw=300 --keep-dup=1. All peaks from replicates of each experiment were combined using bedtools 'merge' function and the union of peaks was quantified over each aligned bam file using bedtools 'coverage' and normalized to RPKM. Differential accessibility analysis was performed using DEseq296 with parameters test = "Wald", betaPrior = F, fitType = "parametric". For comparison of time-course EBF1 degradation and restoration, significance cutoff was abs(Log2(fold change)) > 1 and FDR < 1E-3.

ChIP-seq data analysis

Reads from ChIP-seq experiments were aligned with the same procedure as ATAC-seq above. For Granta519 EBF1 ChIPseq, peaks of each library were identified using MACS2 (version 2.0.9)95- with parameters -p 1E-3 -g hs --nomodel --shiftsize=0.5*fragment_length --format=BAM --bw=300 --keep-dup=1 and with corresponding input control. 25,227 reproducible EBF1 ChIP-seq peaks identified in libraries of both replicates of both antibodies were used in downstream analyses. For comparing protein loading, reproducible EBF1-bound regions were quantified on each ChIP-seq bam files using bedtools 'coverage' and normalized to RPKM and averaged between the two replicates of each antibody. Clustering of reproducible EBF1-bound regions (Fig. 1A) was performed with R function hclust(dc, method="average", members=NULL) and hc_tree <- cutree(hc, k = 15) and visualized with 'pheatmap'. Dynamic EBF1 peaks were filtered as reproducible EBF1 peaks > 1 averaged RPKM in untreated Granta519-EBF1-FKBP-KI clone 27. 7,777 peaks with Log2(fold change) < -1 of averaged RPKM between 6h and 24h dTAG-treated versus untreated and Log2(fold change) > 1 of averaged RPKM between 6h and 24h washout versus 24h dTAG-treated were defined as dynamic EBF1 peaks. SMC1, CTCF and YY1 ChIP-seq libraries were individually quantified on EBF1 peaks using bedtools 'coverage' and normalized to RPKM and averaged between the two replicates per condition, and Log2 fold changes were calculated as above.

For tag density plots, aligned bam files of the two replicates of each condition were merged using samtools (version 1.3)97 'cat' command. For each merged library, fragment length was estimated with HOMER 'makeTagDirectory'. HOMER 'annotatePeaks.pl' was used on merged libraries and visualized with R function 'pheatmap'. For merged libraries genome tracks, bedgraph of reads normalized to reads per million (RPM) were generated with bedtools 'genomecov'. Selected genomic loci were visualized with R package Sushi (version 1.18.0)98 function 'plotBedgraph'. Genome-wide uploadable bigWig files were generated with UCSC tools (version 329)99 'bedGraphToBigWig'.

Hi-C, SMC1 HiChIP and Micro-C analysis

Alignment and significant interaction calling

Raw reads for Granta519-Cas9 Ctrl and EBF1 KO Hi-C, Granta519-EBF1-FKBP-KI clones 27 and 97 time-course MicroC, and DND41 parental and GSI-resistant Micro-C samples were processed with Juicer (version 1.5.6)100 with parameters -g hg19 -s none. To generate contact maps of 30 Kb resolution in comparison with ORCA data, juicer_tools.1.7.6 'pre' command was used on merged_nodups.txt with -r 2500000, 1000000, 500000, 250000, 100000, 50000, 30000, 25000, 10000, 5000 to generate the final .hic files. Normalized contact matrices were extracted using juicer_tools.1.7.6 'dump' command with 'observed VC_SQRT BP 30000' for chromosome 8 (MYC) and chromosome 2 (ZEB2 and KLF7) for plotting contact maps with R 'pheatmap' (Figs. 3, 6 and 7). Each .hic file was also converted to .mcool files using 'hic2cool convert' to maintain VC_SQRT normalization for quantification in Fig. 2.

Raw reads for each HiChIP sample were processed with HiC-Pro (version v2.5.0)101 to obtain putative interactions with default parameters except LIGATION_SITE = GATCGATC and GENOME_FRAGMENT generated for MboI restriction enzyme. Valid pairs (VI), self-circle (SC) and dangling-end (DE) interactions in cis were used as input for significant interaction calling in '.bedpe' format. Mango (version 1.2.0)102 step 4 identified putative significant interaction anchors by MACS peak calling with MACS_qvalue = 0.05 and MACS_shiftsize = 75. Mango step 5 identified significant interactions with default parameters except maxinteractingdist = 2000000 and MHT = found. Only significant interactions with PETs >= 5 were used in the following analyses.

TAD boundary analysis

Raw reads for Granta519-Cas9 ctrl and EBF1 KO Hi-C samples were processed with open2c distiller-nf (version v0.3.4)103 to generate mcool files. Boundaries were identified in Python (version 3.9.13) using cooltools104 with window sizes of 50000,100000 and filtered with boundary strength > 0.5 with both window sizes. Boundaries in control conditions with EBF1 < 2.5 Kb are considered EBF1-bound. Pileup of EBF1-bound or EBF1-unbound boundaries in ctrl and EBF1 KO HiC were calculated with cooltools.pileup and visualized with matplotlib.pyplot (Fig. 1E).

Long-range regulatory loops

Long-range regulatory loops were defined using SMC1 and EBF1 HiChIP significant interactions. Significant interactions with EBF1, SMC1, CTCF, YY1 or H3K27ac ChIP-seq signal on both loop anchors were further classified into enhancer-enhancer (EE), enhancer-promoter (EP) promoter-promoter (PP), CTCF-CTCF and other interactions based on the presence of enhancers, promoters and CTCF peaks at the summit of the two anchors +/- 5 Kb. Normalized interactions at selected loci were visualized with R package Sushi98 (version 1.18.0) function 'plotBedpe'.

Differential compartment calling

A/B compartments detected at 50 Kb resolution was tested. Hi-C processed data was converted into the HOMER (v4.11)19 'HiCSummary'

format. Subsequently, the Hi-C data was processed with HOMER command 'makeTagDirectories' with parameters -format 'HiCSummary'. To identify compartment regions across the genome, HOMER runHiCpca.pl command was used on each condition with H3K27ac ChIP-seq as reference to ensure sign consistency via the -active option. To concatenate PC values from each condition, HOMER annotatePeaks.pl was used with the -noblanks and -bedGraph options. Scatterplot of the PC values from EBF1 Ctrl and KO conditions were plotted.

Hub analysis

Hubs were defined as previously described as "3D clique"27. Briefly, an undirected graph of regulatory interactions was constructed for each HiChIP where each vertex was an enhancer, or a promoter and each edge was a significant enhancer-enhancer, enhancer-promoter, or promoter-promoter interaction. Clusters of interacting enhancers and/or promoters were defined by spectral clustering105 of the regulatory graph interactions using cluster_louvain function in igraph R package with default parameters. Connectivity of an enhancer-promoter cluster was defined as the number of edges connecting vertices within the cluster. The connectivity of clusters was ranked in ascending order and plotted against the rank. Enhancer-promoter hubs were defined as clusters of enhancers and promoters with connectivity greater than the cutoff set as the elbow of the cumulative connectivity curve, which is shown as a tangent line in Fig. 1F. Hubs with > 10 or <= 10 expressed genes (defined in the following section) are considered gene-dense or gene-sparse hubs, respectively. Pairwise interactions between enhancers and promoters in hubs were quantified in Granta519-EBF1-FKBP-KI clone 27 time-course Micro-C .mcool files with VC_SQRT normalization using cooltools104. Interactions with Log2(fold change) < -0.5 between 6h or 24h dTAG-treated versus untreated and Log2(fold change) > 0.5 between 6h or 24h washout versus 24h dTAG-treated were defined as differential loops. Pileup plots of differential loops on Granta519-EBF1-FKBP-KI clone 27 time-course Micro-C were generated with R package GENOVA (version 1.0.1)106 APA and 'visualise' functions (Fig. 2G).

RNA-seq data analysis

RNA-seq data was aligned to Ensembl GRCh37.75 primary assembly including chromosomes 1-22, chrX, chrY, chrM and contigs using STAR (version 2.5)107 with parameters --outFilterIntronMotifs RemoveNoncanonicalUnannotated --alignIntronMax 100000 --outSAMstrandField intronMotif --outSAMunmapped Within --chimSegmentMin 25 --chimJunctionOverhangMin 25. Strand-specific read counts were quantified using Subread (version 1.5.1) 'featureCounts' with parameters -t exon -g gene_id -s 1 -T 6 and used as input to differential gene expression analysis. Read counts were normalized to reads per million per kilobase (RPKM) for each gene. For Granta519-Cas9 ctrl and EBF1 KO samples, expressed genes were determined as genes with > 1 RPKM in at least 3 of the individual libraries. For Granta519-EBF1-FKBP-KI clones 27 and 97, expressed genes were determined as genes with > 1 average RPKM of the triplicates per condition in at least 3 conditions per clone. Pairwise differential gene expression analysis was performed using DEseq296 with parameters test = "Wald", betaPrior = F, fitType = "parametric". Significance cutoff was abs(Log2(fold change)) > 0.5 and FDR < 0.05. Expressed genes in gene-dense and gene-sparse hubs were ranked by averaged RPKM and the top 500 genes of each category were used to conduct Gene Ontology (GO) enrichment analysis. GO sets only enriched in gene-dense or gene-sparse hubs with FDR < 1E-7 were visualized in R (Figs. 1K and 1L).

ORCA data analysis

ChrTracer3, QC and imputation

Raw images were exported as individual .tiff per FOV, step, z-plane and channel using Vutara SRX (No hardware version 7.1.38). Tiff files for each readout were compiled as ConvZscan.dax and ConvZscan.inf files using MATLAB as input for ChrTracer331. ChrTracer3 was followed stepwise for drift correction, spot selection, and spot fitting using default parameters except changing the pixel to nm conversion for xy and z planes. Traces identified in all FOV per experiment were concatenated and further analyzed in R and MATLAB. For each trace, the number of registered steps and brightness (column "h" in ChrTracer3 output table) were used for quality control. For 30-step walks, traces with less or equal to 5 missing steps were kept. For 36-step walks, the cutoff was 6 missing steps and for 72-step walks the cutoff was 15.

Distance and contact frequency

Granta519-EBF1-FKBP-KI MYC locus: pairwise distances were calculated on unimputed traces per condition (untreated, 6h dTAG, 24h dTAG, 6h washout, 24h washout) per biological replicate (clone 27 and clone 97). Using the median distance of all neighboring steps (i.e. step 1 to 2, 2 to 3, … 29 to 30) as cutoff, the contact frequency vectors of unimputed traces were generated and the Pearson correlations were calculated. After confirmation of >95% correlation between the two replicates, the traces were combined for downstream analyses. More details can be found in Table S6. The median distances across combined traces excluding missing values were used to plot the final distance map per condition (Fig. S3). The neighboring step cutoff was recalculated with combined traces and used to generate contact frequency maps (Fig. 3) and compare enhancer-promoter contact frequencies (Fig. 4). Interaction between MYC and super-enhancer E1 was defined as distances between either step 25-7 or 25-8 smaller than cutoffs per condition. MYC to super-enhancer E2 interaction was defined as distance between step 25-11 smaller than cutoffs per condition. For E1, equally spaced bins were [1-18, 2-19, …, 8-25, …,13-30] or [2-18 (for padding), 1-19, 2-20, …, 7-25, …, 12-30] (Fig. 4B). For E2, equally spaced bins were [4-18, 5-19, …, 11-25, …, 16-30] (Fig. 4C). Control regions were defined as [6-23, 7-24, 9-26] or [7-23, 8-24, 10-26] for MYC-to-E1 and [10-23, 11-24, 13-26] for MYC-to-E2 and the contact frequencies were averaged with missing values removed (Figs. 4D and 4E). Error bars in Fig. 4 were 95% confidence intervals of contact frequencies calculated from 1,000 sets of 500 randomly sampled alleles.

DND41 KLF7 and ZEB2 loci: pairwise distances were calculated on unimputed traces per condition (GSI-sensitive, GSI-resistant). The median distances across combined traces excluding missing values were used to plot the final distance map per condition (Figs. 6 and S6). 250 nm was used as cutoff for determining pairwise interaction.

DND41 MYC locus: pairwise distances were calculated on unimputed traces per condition (GSI-sensitive, GSI-resistant) in two biological replicates and combined. The median distances across combined traces excluding missing values were used to plot the final distance map per condition (Fig. S7). The contact frequency matrices were generated using the median distance of all neighboring steps per condition as cutoffs per condition. MYC and super-enhancer TE1 was defined as interacting whenever any distance between step 4 to steps 52, 53, or 54 was smaller than the condition's cutoff. MYC and super-enhancer TE2 was defined as interacting whenever any distance between step 4 to steps 65, 66, or 67 was smaller than the condition's cutoff. Error bars in Fig. 7 were 95% confidence intervals of contact frequencies calculated from 1,000 sets of 1,000 randomly sampled alleles.

Clustering and radius of gyration

Granta519 EBF1-FKBP-KI MYC locus: Filtered, imputed alleles from all conditions and replicates were combined and the pairwise distance vectors were calculated as input to K-means clustering using R 'kmeans' function with centers = 10 and iter.max = 20. The neighboring step cutoff was recalculated with combined traces and used to generate contact matrices for each K. Contact maps of each K were manually inspected and arranged as in Fig. 3F. K-means clustering was then conducted on each condition and manually inspected to be arranged in the same order as Fig. 3F. Stratification of whether the allele has E1, E2 and MYC interactions were determined as described above using the unimputed values of the allele. Error bars in Figs 4H and S4E-H were confidence intervals calculated from 1000 sets of 500 randomly sampled alleles. Imputed alleles from all conditions were used for radius of gyration calculation per definition in Fig. 4F.

Polymer Simulations

Simulation of loop extrusion was performed using Open2C's polychrom Python library (v0.1.1)108 with slight modifications. The simulation framework is divided into two steps: a 1-dimensional step and a 3-dimensional step. The 1-dimensional step tracks the movement of c × 2 cohesin legs/anchors (c = the number of cohesins) across a polymer comprised of N monomers, where each monomer represents a genomic region of length M. The length in base pairs represented by the polymer can then be calculated as L=N × M. A predefined number of cohesins c can each be either randomly loaded onto any monomer with a uniform probability distribution ('random loading'), or loaded onto a specific region / sequence of monomers with uniform probability from which it will extrude ('targeted loading'), these behaviors constitute the modified portion of the polychrom package. Targeted loading was primarily used in the loading scenario to simulate EBF1's loading of cohesin at specific locations, while random loading was utilized in the blocking scenario. At each 1D step, the two anchors of the cohesin can take 4 possible actions: (1) unimpeded cohesin movement, which is defined as translocation of the anchors at positions x_1 and x_2 to their adjacent monomers x_1 - 1 and x_2+ 1 followed by forming a synthetic chemical bond between monomors occupied by the anchors, (2) unload the entire cohesin, including both anchors, from the polymer with probability 1/l where l is the average number of monomers traversed ('lifetime') and load another cohesin in the same manner, (3) become blocked by a blocking element (i.e. CTCF or EBF1 as a blocker) at a monomer with probability p_b, which may then release the anchor with probability p_r at subsequent steps, or (4) become stalled against another cohesin anchor, in which case extrusion is also halted, but the lifetime l of the cohesin is reduced by one-tenth (i.e. l_stalled = 0.1 × l). The 3-dimensional step reads the cohesin positions produced by the 1-dimensional step and maps them onto a polymer in 3D space created with OpenMM. The polymer was considered as a self-avoiding walk (SAW) grown on a cubic lattice, and undergoes energy minimization followed by subsequent steps of cohesin movement as defined above. All thermodynamic and integration parameters were kept as the defaults provided by the polychrom library. The full list of altered simulation parameters distinguishing loading from blocking scenarios can be found in Table S7. The outputs of the 3-dimensional steps are the (x,y,z) coordinates of each monomer in the ensemble of simulated polymers, which are used in subsequent analyses to calculate distances and interaction frequencies in Fig. 5.

For manuscripts utilizing custom algorithms or software that are central to the research but not yet described in published literature, software must be made available to editors and reviewers. We strongly encourage code deposition in a community repository (e.g. GitHub). See the Nature Portfolio guidelines for submitting code & software for further information.

Data

Policy information about availability of data

All manuscripts must include a data availability statement. This statement should provide the following information, where applicable:

- Accession codes, unique identifiers, or web links for publicly available datasets
- A description of any restrictions on data availability
- For clinical datasets or third party data, please ensure that the statement adheres to our policy

155 genome-wide sequencing experiments reported in this study are made available at the GEO session GSE293368. Optical chromatin processed data will be available at OLIVE, a data portal that we developed for interactive querying and exploration of chromatin traces.

Research involving human participants, their data, or biological material

Policy information about studies with human participants or human data. See also policy information about sex, gender (identity/presentation), and sexual orientation and race, ethnicity and racism.

Reporting on sex and gender	N/A
Reporting on race, ethnicity, or other socially relevant groupings	N/A
Population characteristics	N/A
Recruitment	N/A
Ethics oversight	N/A

Note that full information on the approval of the study protocol must also be provided in the manuscript.

Field-specific reporting

Please select the one below that is the best fit for your research. If you are not sure, read the appropriate sections before making your selection.

☒ Life sciences ☐ Behavioural & social sciences ☐ Ecological, evolutionary & environmental sciences

For a reference copy of the document with all sections, see nature.com/documents/nr-reporting-summary-flat.pdf

Life sciences study design

All studies must disclose on these points even when the disclosure is negative.

Sample size	The sample sizes of two biological replicates demonstrated the differences between experimental groups and were reproducible and significant, No statistical method was used to determine sample size. Experimental design ensures comparing two conditions, while all other variable are invariants, hence description of all covariates is not applicable to the studies.
Data exclusions	No data were excluded from the analyses.
Replication	2-5 independent experiments were performed on distinct single-cell clones of each genotype. All attempts at replication were successful.
Randomization	No experiment in this study required randomization.
Blinding	No experiment in this study required blinding because the case and control (e.g. WT and KO) are known. The Investigators were blinded to allocation during ORCA data analysis.

Reporting for specific materials, systems and methods

We require information from authors about some types of materials, experimental systems and methods used in many studies. Here, indicate whether each material, system or method listed is relevant to your study. If you are not sure if a list item applies to your research, read the appropriate section before selecting a response.

Materials & experimental systems

n/a	Involved in the study
☐	☒ Antibodies
☐	☒ Eukaryotic cell lines
☒	☐ Palaeontology and archaeology
☒	☐ Animals and other organisms
☒	☐ Clinical data
☒	☐ Dual use research of concern
☒	☐ Plants

Methods

n/a	Involved in the study
☐	☒ ChIP-seq
☐	☒ Flow cytometry
☒	☐ MRI-based neuroimaging

Antibodies

Antibodies used	H3K27ac (Active Motif cat# 39133), H3K4me1 (Abcam cat# ab8895), H3K27me3 (CST cat# 9733),polyclonal anti-EBF1 (1C) antibody, which recognizes an N-terminal EBF1 peptide (RG), commercial EBF1 antibody (Millipore cat# AB10523), SMC1a (Bethyl, cat# A300-055A), YY1 (Active motif cat# 61779), CTCF (EMD Millipore cat# 07-729)
Validation	H3K27ac: https://www.activemotif.com/catalog/details/39133/histone-h3-acetyl-lys27-antibody-pab H3K4me1: https://www.abcam.com/en-us/products/primary-antibodies/histone-h3-mono-methyl-k4-antibody-chip-grade-ab8895?srsltid=AfmBOor5gzGG69Wjkc-0sLy3KuEy9Rqt1xOc6pxK_Np3OBH3yNzdw6TU H3K27me3: https://www.cellsignal.com/products/primary-antibodies/tri-methyl-histone-h3-lys27-c36b11-rabbit-mab/9733?srsltid=AfmBOor-QBFcVGIW4rUZMAXxXXMnF45t0quZuIJthGOvpBNzc_SS167j polyclonal anti-EBF1 (1C) antibody: https://www.cell.com/immunity/fulltext/S1074-7613(16)30059-0 commercial EBF1 antibody: https://www.sigmaaldrich.com/US/en/product/mm/ab10523?emdredirect=1 SMC1a: https://www.fortislife.com/products/primary-antibodies/rabbit-anti-smc1-antibody/BETHYL-A300-055 YY1: https://www.activemotif.com/catalog/details/61779/yy1-antibody-pab-1 CTCF: https://www.sigmaaldrich.com/US/en/product/mm/07729

Eukaryotic cell lines

Policy information about cell lines and Sex and Gender in Research

Cell line source(s)	DND41, JVM-2 and PGA-1 were purchased from Leibniz-Institute DSMZ-German Collection of Microorganisms and Cell Lines (DSMZ, cat# ACC525, ACC12, ACC766). HEK293T (CRL-11268) was purchased from ATCC. Granta519 was from the Broad

Novartis Cancer Cell Line encyclopedia63. DND41, JVM-2 and PGA-1 were cultured in RPMI 1640 (Corning, cat# 10-040-CM) supplemented with 10% fetal bovine serum (Hyclone, cat# SH30070.03), 2 mM L-glutamine (Corning, cat# 25-005-CI), 100 U/mL and 100 µg/mL penicillin/streptomycin (Corning, cat# 30-002-CI), 100 mM nonessential amino acids (Gibco, cat# 11140-050), 1 mM sodium pyruvate (Gibco, cat#11360-070) and 0.1 mM of 2-mercaptoethanol (Sigma, cat# M3148). HEK293T and Granta519 were cultured in DMEM (Corning, cat# 10-013-CV) supplemented with 10% fetal bovine serum (Hyclone, cat# SH30070.03) and 100 U/mL and 100 µg/mL penicillin/streptomycin (Corning, cat# 30-002-CI). GSI-resistant DND41 cells were generated as previously described72. All cell lines, including the cell lines described below, were grown at 37 C and 5% CO2 and were used at a low passage number (<12) and subjected to regular mycoplasma tests and short tandem repeat (STR) profiling.

Authentication: Genomic DNA was extracted from cells and subjected to STR testing. Results are available upon request.

Mycoplasma contamination: Mycoplasma testing was performed with MYCOALERT DETECTION KIT- 100 TESTS (Lonza LT07-318)

Commonly misidentified lines (See ICLAC register): N/A

Plants

Seed stocks: N/A

Novel plant genotypes: N/A

Authentication: N/A

ChIP-seq

Data deposition

☒ Confirm that both raw and final processed data have been deposited in a public database such as GEO.

☒ Confirm that you have deposited or provided access to graph files (e.g. BED files) for the called peaks.

Data access links
May remain private before publication.

GEO session GSE293368 (access token: yrengkyibvejxoz)

Files in database submission

ATACseq:
s01_240417_Granta519cl27_6hWO_ATAC_rep1_S1.filt.srt.nodup.noBlack.bam.bw
s01_240417_Granta519cl27_6hWO_ATAC_rep1_S1_R1.fastq.gz
s01_240417_Granta519cl27_6hWO_ATAC_rep1_S1_R2.fastq.gz
s02_240417_Granta519cl27_6hWO_ATAC_rep2_S2.filt.srt.nodup.noBlack.bam.bw
s02_240417_Granta519cl27_6hWO_ATAC_rep2_S2_R1.fastq.gz
s02_240417_Granta519cl27_6hWO_ATAC_rep2_S2_R2.fastq.gz
s03_240417_Granta519cl27_6hWO_ATAC_rep3_S3.filt.srt.nodup.noBlack.bam.bw
s03_240417_Granta519cl27_6hWO_ATAC_rep3_S3_R1.fastq.gz
s03_240417_Granta519cl27_6hWO_ATAC_rep3_S3_R2.fastq.gz
s07_240417_Granta519cl27_24hWO_ATAC_rep1_S7.filt.srt.nodup.noBlack.bam.bw
s07_240417_Granta519cl27_24hWO_ATAC_rep1_S7_R1.fastq.gz
s07_240417_Granta519cl27_24hWO_ATAC_rep1_S7_R2.fastq.gz
s08_240417_Granta519cl27_24hWO_ATAC_rep2_S8.filt.srt.nodup.noBlack.bam.bw
s08_240417_Granta519cl27_24hWO_ATAC_rep2_S8_R1.fastq.gz
s08_240417_Granta519cl27_24hWO_ATAC_rep2_S8_R2.fastq.gz
s09_240417_Granta519cl27_24hWO_ATAC_rep3_S9.filt.srt.nodup.noBlack.bam.bw
s09_240417_Granta519cl27_24hWO_ATAC_rep3_S9_R1.fastq.gz
s09_240417_Granta519cl27_24hWO_ATAC_rep3_S9_R2.fastq.gz
s25_221120_Granta519EBF1KI_cl27_0hr_ATACseq_rep1_S25.filt.srt.nodup.noBlack.bam.bw
s25_221120_Granta519EBF1KI_cl27_0hr_ATACseq_rep1_S25_R1.fastq.gz
s25_221120_Granta519EBF1KI_cl27_0hr_ATACseq_rep1_S25_R2.fastq.gz
s26_221120_Granta519EBF1KI_cl27_0hr_ATACseq_rep2_S26.filt.srt.nodup.noBlack.bam.bw
s26_221120_Granta519EBF1KI_cl27_0hr_ATACseq_rep2_S26_R1.fastq.gz
s26_221120_Granta519EBF1KI_cl27_0hr_ATACseq_rep2_S26_R2.fastq.gz
s27_221120_Granta519EBF1KI_cl27_0hr_ATACseq_rep3_S27.filt.srt.nodup.noBlack.bam.bw
s27_221120_Granta519EBF1KI_cl27_0hr_ATACseq_rep3_S27_R1.fastq.gz
s27_221120_Granta519EBF1KI_cl27_0hr_ATACseq_rep3_S27_R2.fastq.gz
s28_221120_Granta519EBF1KI_cl27_6hr_ATACseq_rep1_S28.filt.srt.nodup.noBlack.bam.bw
s28_221120_Granta519EBF1KI_cl27_6hr_ATACseq_rep1_S28_R1.fastq.gz
s28_221120_Granta519EBF1KI_cl27_6hr_ATACseq_rep1_S28_R2.fastq.gz

s29_221120_Granta519EBF1KI_cl27_6hr_ATACseq_rep2_S29.filt.srt.nodup.noBlack.bam.bw
s29_221120_Granta519EBF1KI_cl27_6hr_ATACseq_rep2_S29_R1.fastq.gz
s29_221120_Granta519EBF1KI_cl27_6hr_ATACseq_rep2_S29_R2.fastq.gz
s30_221120_Granta519EBF1KI_cl27_6hr_ATACseq_rep3_S30.filt.srt.nodup.noBlack.bam.bw
s30_221120_Granta519EBF1KI_cl27_6hr_ATACseq_rep3_S30_R1.fastq.gz
s30_221120_Granta519EBF1KI_cl27_6hr_ATACseq_rep3_S30_R2.fastq.gz
s31_221120_Granta519EBF1KI_cl27_8hr_ATACseq_rep1_S31.filt.srt.nodup.noBlack.bam.bw
s31_221120_Granta519EBF1KI_cl27_8hr_ATACseq_rep1_S31_R1.fastq.gz
s31_221120_Granta519EBF1KI_cl27_8hr_ATACseq_rep1_S31_R2.fastq.gz
s32_221120_Granta519EBF1KI_cl27_8hr_ATACseq_rep2_S32.filt.srt.nodup.noBlack.bam.bw
s32_221120_Granta519EBF1KI_cl27_8hr_ATACseq_rep2_S32_R1.fastq.gz
s32_221120_Granta519EBF1KI_cl27_8hr_ATACseq_rep2_S32_R2.fastq.gz
s33_221120_Granta519EBF1KI_cl27_8hr_ATACseq_rep3_S33.filt.srt.nodup.noBlack.bam.bw
s33_221120_Granta519EBF1KI_cl27_8hr_ATACseq_rep3_S33_R1.fastq.gz
s33_221120_Granta519EBF1KI_cl27_8hr_ATACseq_rep3_S33_R2.fastq.gz
s34_221120_Granta519EBF1KI_cl27_24hr_ATACseq_rep1_S34.filt.srt.nodup.noBlack.bam.bw
s34_221120_Granta519EBF1KI_cl27_24hr_ATACseq_rep1_S34_R1.fastq.gz
s34_221120_Granta519EBF1KI_cl27_24hr_ATACseq_rep1_S34_R2.fastq.gz
s35_221120_Granta519EBF1KI_cl27_24hr_ATACseq_rep2_S35.filt.srt.nodup.noBlack.bam.bw
s35_221120_Granta519EBF1KI_cl27_24hr_ATACseq_rep2_S35_R1.fastq.gz
s35_221120_Granta519EBF1KI_cl27_24hr_ATACseq_rep2_S35_R2.fastq.gz
s36_221120_Granta519EBF1KI_cl27_24hr_ATACseq_rep3_S36.filt.srt.nodup.noBlack.bam.bw
s36_221120_Granta519EBF1KI_cl27_24hr_ATACseq_rep3_S36_R1.fastq.gz
s36_221120_Granta519EBF1KI_cl27_24hr_ATACseq_rep3_S36_R2.fastq.gz
s40_230103_Granta519EBF1KI_cl27_48hr_ATACseq_rep1_S16.filt.srt.nodup.noBlack.bam.bw
s40_230103_Granta519EBF1KI_cl27_48hr_ATACseq_rep1_S16_R1.fastq.gz
s40_230103_Granta519EBF1KI_cl27_48hr_ATACseq_rep1_S16_R2.fastq.gz
s41_230103_Granta519EBF1KI_cl27_48hr_ATACseq_rep2_S17.filt.srt.nodup.noBlack.bam.bw
s41_230103_Granta519EBF1KI_cl27_48hr_ATACseq_rep2_S17_R1.fastq.gz
s41_230103_Granta519EBF1KI_cl27_48hr_ATACseq_rep2_S17_R2.fastq.gz
s42_230103_Granta519EBF1KI_cl27_48hr_ATACseq_rep3_S18.filt.srt.nodup.noBlack.bam.bw
s42_230103_Granta519EBF1KI_cl27_48hr_ATACseq_rep3_S18_R1.fastq.gz
s42_230103_Granta519EBF1KI_cl27_48hr_ATACseq_rep3_S18_R2.fastq.gz
s43_230103_Granta519EBF1KI_cl27_72hr_ATACseq_rep1_S19.filt.srt.nodup.noBlack.bam.bw
s43_230103_Granta519EBF1KI_cl27_72hr_ATACseq_rep1_S19_R1.fastq.gz
s43_230103_Granta519EBF1KI_cl27_72hr_ATACseq_rep1_S19_R2.fastq.gz
s44_230103_Granta519EBF1KI_cl27_72hr_ATACseq_rep2_S20.filt.srt.nodup.noBlack.bam.bw
s44_230103_Granta519EBF1KI_cl27_72hr_ATACseq_rep2_S20_R1.fastq.gz
s44_230103_Granta519EBF1KI_cl27_72hr_ATACseq_rep2_S20_R2.fastq.gz
s45_230103_Granta519EBF1KI_cl27_72hr_ATACseq_rep3_S21.filt.srt.nodup.noBlack.bam.bw
s45_230103_Granta519EBF1KI_cl27_72hr_ATACseq_rep3_S21_R1.fastq.gz
s45_230103_Granta519EBF1KI_cl27_72hr_ATACseq_rep3_S21_R2.fastq.gz

ChIPseq:
s01_230103_Granta519EBF1KI_cl27_0hr_H3K27ac_ChIP_rep1_S1.filt.srt.nodup.noBlack.bam.bw
s01_230103_Granta519EBF1KI_cl27_0hr_H3K27ac_ChIP_rep1_S1_R1.fastq.gz
s01_230103_Granta519EBF1KI_cl27_0hr_H3K27ac_ChIP_rep1_S1_R2.fastq.gz
s01_240610_Granta519EBF1KI_cl27_0hr_CTCF_CHIPseq_rep1_S1.filt.srt.nodup.noBlack.bam.bw
s01_240610_Granta519EBF1KI_cl27_0hr_CTCF_CHIPseq_rep1_S1_R1.fastq.gz
s01_240610_Granta519EBF1KI_cl27_0hr_CTCF_CHIPseq_rep1_S1_R2.fastq.gz
s01_240701_Granta519cl27_0hr_YY1_ChIP_rep1_S1.filt.srt.nodup.noBlack.bam.bw
s01_240701_Granta519cl27_0hr_YY1_ChIP_rep1_S1_R1.fastq.gz
s01_240701_Granta519cl27_0hr_YY1_ChIP_rep1_S1_R2.fastq.gz
s02_230103_Granta519EBF1KI_cl27_0hr_H3K27ac_ChIP_rep2_S2.filt.srt.nodup.noBlack.bam.bw
s02_230103_Granta519EBF1KI_cl27_0hr_H3K27ac_ChIP_rep2_S2_R1.fastq.gz
s02_230103_Granta519EBF1KI_cl27_0hr_H3K27ac_ChIP_rep2_S2_R2.fastq.gz
s02_240610_Granta519EBF1KI_cl27_0hr_CTCF_CHIPseq_rep2_S2.filt.srt.nodup.noBlack.bam.bw
s02_240610_Granta519EBF1KI_cl27_0hr_CTCF_CHIPseq_rep2_S2_R1.fastq.gz
s02_240610_Granta519EBF1KI_cl27_0hr_CTCF_CHIPseq_rep2_S2_R2.fastq.gz
s02_240701_Granta519cl27_0hr_YY1_ChIP_rep2_S2.filt.srt.nodup.noBlack.bam.bw
s02_240701_Granta519cl27_0hr_YY1_ChIP_rep2_S2_R1.fastq.gz
s02_240701_Granta519cl27_0hr_YY1_ChIP_rep2_S2_R2.fastq.gz
s03_230103_Granta519EBF1KI_cl27_0hr_H3K4me1_ChIP_rep1_S3.filt.srt.nodup.noBlack.bam.bw
s03_230103_Granta519EBF1KI_cl27_0hr_H3K4me1_ChIP_rep1_S3_R1.fastq.gz
s03_230103_Granta519EBF1KI_cl27_0hr_H3K4me1_ChIP_rep1_S3_R2.fastq.gz
s03_240610_Granta519EBF1KI_cl27_6hdTAG_CTCF_CHIPseq_rep1_S3.filt.srt.nodup.noBlack.bam.bw
s03_240610_Granta519EBF1KI_cl27_6hdTAG_CTCF_CHIPseq_rep1_S3_R1.fastq.gz
s03_240610_Granta519EBF1KI_cl27_6hdTAG_CTCF_CHIPseq_rep1_S3_R2.fastq.gz
s03_240701_Granta519cl27_6hdTAG_YY1_ChIP_rep1_S3.filt.srt.nodup.noBlack.bam.bw
s03_240701_Granta519cl27_6hdTAG_YY1_ChIP_rep1_S3_R1.fastq.gz
s03_240701_Granta519cl27_6hdTAG_YY1_ChIP_rep1_S3_R2.fastq.gz
s04_230103_Granta519EBF1KI_cl27_0hr_H3K4me1_ChIP_rep2_S4.filt.srt.nodup.noBlack.bam.bw
s04_230103_Granta519EBF1KI_cl27_0hr_H3K4me1_ChIP_rep2_S4_R1.fastq.gz
s04_230103_Granta519EBF1KI_cl27_0hr_H3K4me1_ChIP_rep2_S4_R2.fastq.gz
s04_240610_Granta519EBF1KI_cl27_6hdTAG_CTCF_CHIPseq_rep2_S4.filt.srt.nodup.noBlack.bam.bw
s04_240610_Granta519EBF1KI_cl27_6hdTAG_CTCF_CHIPseq_rep2_S4_R1.fastq.gz

s04_240610_Granta519EBF1KI_cl27_6hdTAG_CTCF_CHIPseq_rep2_S4_R2.fastq.gz
s04_240701_Granta519cl27_6hdTAG_YY1_ChIP_rep2_S4.filt.srt.nodup.noBlack.bam.bw
s04_240701_Granta519cl27_6hdTAG_YY1_ChIP_rep2_S4_R1.fastq.gz
s04_240701_Granta519cl27_6hdTAG_YY1_ChIP_rep2_S4_R2.fastq.gz
s05_230103_Granta519EBF1KI_cl27_0hr_H3K27me3_ChIP_rep1_S5.filt.srt.nodup.noBlack.bam.bw
s05_230103_Granta519EBF1KI_cl27_0hr_H3K27me3_ChIP_rep1_S5_R1.fastq.gz
s05_230103_Granta519EBF1KI_cl27_0hr_H3K27me3_ChIP_rep1_S5_R2.fastq.gz
s05_240610_Granta519EBF1KI_cl27_24hdTAG_CTCF_CHIPseq_rep1_S5.filt.srt.nodup.noBlack.bam.bw
s05_240610_Granta519EBF1KI_cl27_24hdTAG_CTCF_CHIPseq_rep1_S5_R1.fastq.gz
s05_240610_Granta519EBF1KI_cl27_24hdTAG_CTCF_CHIPseq_rep1_S5_R2.fastq.gz
s05_240701_Granta519cl27_24hdTAG_YY1_ChIP_rep1_S5.filt.srt.nodup.noBlack.bam.bw
s05_240701_Granta519cl27_24hdTAG_YY1_ChIP_rep1_S5_R1.fastq.gz
s05_240701_Granta519cl27_24hdTAG_YY1_ChIP_rep1_S5_R2.fastq.gz
s06_230103_Granta519EBF1KI_cl27_0hr_H3K27me3_ChIP_rep2_S6.filt.srt.nodup.noBlack.bam.bw
s06_230103_Granta519EBF1KI_cl27_0hr_H3K27me3_ChIP_rep2_S6_R1.fastq.gz
s06_230103_Granta519EBF1KI_cl27_0hr_H3K27me3_ChIP_rep2_S6_R2.fastq.gz
s06_240610_Granta519EBF1KI_cl27_24hdTAG_CTCF_CHIPseq_rep2_S6.filt.srt.nodup.noBlack.bam.bw
s06_240610_Granta519EBF1KI_cl27_24hdTAG_CTCF_CHIPseq_rep2_S6_R1.fastq.gz
s06_240610_Granta519EBF1KI_cl27_24hdTAG_CTCF_CHIPseq_rep2_S6_R2.fastq.gz
s06_240701_Granta519cl27_24hdTAG_YY1_ChIP_rep2_S6.filt.srt.nodup.noBlack.bam.bw
s06_240701_Granta519cl27_24hdTAG_YY1_ChIP_rep2_S6_R1.fastq.gz
s06_240701_Granta519cl27_24hdTAG_YY1_ChIP_rep2_S6_R2.fastq.gz
s07_230103_Granta519EBF1KI_cl27_6hr_H3K27ac_ChIP_rep1_S7.filt.srt.nodup.noBlack.bam.bw
s07_230103_Granta519EBF1KI_cl27_6hr_H3K27ac_ChIP_rep1_S7_R1.fastq.gz
s07_230103_Granta519EBF1KI_cl27_6hr_H3K27ac_ChIP_rep1_S7_R2.fastq.gz
s07_240610_Granta519EBF1KI_cl27_6hWO_CTCF_CHIPseq_rep1_S7.filt.srt.nodup.noBlack.bam.bw
s07_240610_Granta519EBF1KI_cl27_6hWO_CTCF_CHIPseq_rep1_S7_R1.fastq.gz
s07_240610_Granta519EBF1KI_cl27_6hWO_CTCF_CHIPseq_rep1_S7_R2.fastq.gz
s07_240701_Granta519cl27_6hWO_YY1_ChIP_rep1_S7.filt.srt.nodup.noBlack.bam.bw
s07_240701_Granta519cl27_6hWO_YY1_ChIP_rep1_S7_R1.fastq.gz
s07_240701_Granta519cl27_6hWO_YY1_ChIP_rep1_S7_R2.fastq.gz
s08_230103_Granta519EBF1KI_cl27_6hr_H3K27ac_ChIP_rep2_S8.filt.srt.nodup.noBlack.bam.bw
s08_230103_Granta519EBF1KI_cl27_6hr_H3K27ac_ChIP_rep2_S8_R1.fastq.gz
s08_230103_Granta519EBF1KI_cl27_6hr_H3K27ac_ChIP_rep2_S8_R2.fastq.gz
s08_240610_Granta519EBF1KI_cl27_6hWO_CTCF_CHIPseq_rep2_S8.filt.srt.nodup.noBlack.bam.bw
s08_240610_Granta519EBF1KI_cl27_6hWO_CTCF_CHIPseq_rep2_S8_R1.fastq.gz
s08_240610_Granta519EBF1KI_cl27_6hWO_CTCF_CHIPseq_rep2_S8_R2.fastq.gz
s08_240701_Granta519cl27_6hWO_YY1_ChIP_rep2_S8.filt.srt.nodup.noBlack.bam.bw
s08_240701_Granta519cl27_6hWO_YY1_ChIP_rep2_S8_R1.fastq.gz
s08_240701_Granta519cl27_6hWO_YY1_ChIP_rep2_S8_R2.fastq.gz
s09_230103_Granta519EBF1KI_cl27_6hr_H3K4me1_ChIP_rep1_S9.filt.srt.nodup.noBlack.bam.bw
s09_230103_Granta519EBF1KI_cl27_6hr_H3K4me1_ChIP_rep1_S9_R1.fastq.gz
s09_230103_Granta519EBF1KI_cl27_6hr_H3K4me1_ChIP_rep1_S9_R2.fastq.gz
s09_240610_Granta519EBF1KI_cl27_24hWO_CTCF_CHIPseq_rep1_S9.filt.srt.nodup.noBlack.bam.bw
s09_240610_Granta519EBF1KI_cl27_24hWO_CTCF_CHIPseq_rep1_S9_R1.fastq.gz
s09_240610_Granta519EBF1KI_cl27_24hWO_CTCF_CHIPseq_rep1_S9_R2.fastq.gz
s09_240701_Granta519cl27_24hWO_YY1_ChIP_rep1_S9.filt.srt.nodup.noBlack.bam.bw
s09_240701_Granta519cl27_24hWO_YY1_ChIP_rep1_S9_R1.fastq.gz
s09_240701_Granta519cl27_24hWO_YY1_ChIP_rep1_S9_R2.fastq.gz
s10_230103_Granta519EBF1KI_cl27_6hr_H3K4me1_ChIP_rep2_S10.filt.srt.nodup.noBlack.bam.bw
s10_230103_Granta519EBF1KI_cl27_6hr_H3K4me1_ChIP_rep2_S10_R1.fastq.gz
s10_230103_Granta519EBF1KI_cl27_6hr_H3K4me1_ChIP_rep2_S10_R2.fastq.gz
s10_240610_Granta519EBF1KI_cl27_24hWO_CTCF_CHIPseq_rep2_S10.filt.srt.nodup.noBlack.bam.bw
s10_240610_Granta519EBF1KI_cl27_24hWO_CTCF_CHIPseq_rep2_S10_R1.fastq.gz
s10_240610_Granta519EBF1KI_cl27_24hWO_CTCF_CHIPseq_rep2_S10_R2.fastq.gz
s10_240701_Granta519cl27_24hWO_YY1_ChIP_rep2_S10.filt.srt.nodup.noBlack.bam.bw
s10_240701_Granta519cl27_24hWO_YY1_ChIP_rep2_S10_R1.fastq.gz
s10_240701_Granta519cl27_24hWO_YY1_ChIP_rep2_S10_R2.fastq.gz
s11_230103_Granta519EBF1KI_cl27_6hr_H3K27me3_ChIP_rep1_S11.filt.srt.nodup.noBlack.bam.bw
s11_230103_Granta519EBF1KI_cl27_6hr_H3K27me3_ChIP_rep1_S11_R1.fastq.gz
s11_230103_Granta519EBF1KI_cl27_6hr_H3K27me3_ChIP_rep1_S11_R2.fastq.gz
s12_230103_Granta519EBF1KI_cl27_6hr_H3K27me3_ChIP_rep2_S12.filt.srt.nodup.noBlack.bam.bw
s12_230103_Granta519EBF1KI_cl27_6hr_H3K27me3_ChIP_rep2_S12_R1.fastq.gz
s12_230103_Granta519EBF1KI_cl27_6hr_H3K27me3_ChIP_rep2_S12_R2.fastq.gz
s13_230103_Granta519EBF1KI_cl27_24hr_H3K27ac_ChIP_rep1_S13.filt.srt.nodup.noBlack.bam.bw
s13_230103_Granta519EBF1KI_cl27_24hr_H3K27ac_ChIP_rep1_S13_R1.fastq.gz
s13_230103_Granta519EBF1KI_cl27_24hr_H3K27ac_ChIP_rep1_S13_R2.fastq.gz
s13_240415_Granta519cl27_24hdTAGWO_EBF1_ChIP_rep1_S13.filt.srt.nodup.noBlack.bam.bw
s13_240415_Granta519cl27_24hdTAGWO_EBF1_ChIP_rep1_S13_R1.fastq.gz
s13_240415_Granta519cl27_24hdTAGWO_EBF1_ChIP_rep1_S13_R2.fastq.gz
s13_240427_Granta519cl27_6hWO_EBF1_ChIP_rep1_S13.filt.srt.nodup.noBlack.bam.bw
s13_240427_Granta519cl27_6hWO_EBF1_ChIP_rep1_S13_R1.fastq.gz
s13_240427_Granta519cl27_6hWO_EBF1_ChIP_rep1_S13_R2.fastq.gz
s14_230103_Granta519EBF1KI_cl27_24hr_H3K27ac_ChIP_rep2_S14.filt.srt.nodup.noBlack.bam.bw
s14_230103_Granta519EBF1KI_cl27_24hr_H3K27ac_ChIP_rep2_S14_R1.fastq.gz
s14_230103_Granta519EBF1KI_cl27_24hr_H3K27ac_ChIP_rep2_S14_R2.fastq.gz

s14_240415_Granta519cl27_24hdTAGWO_EBF1_ChIP_rep2_S14.filt.srt.nodup.noBlack.bam.bw
s14_240415_Granta519cl27_24hdTAGWO_EBF1_ChIP_rep2_S14_R1.fastq.gz
s14_240415_Granta519cl27_24hdTAGWO_EBF1_ChIP_rep2_S14_R2.fastq.gz
s14_240427_Granta519cl27_6hWO_EBF1_ChIP_rep2_S14.filt.srt.nodup.noBlack.bam.bw
s14_240427_Granta519cl27_6hWO_EBF1_ChIP_rep2_S14_R1.fastq.gz
s14_240427_Granta519cl27_6hWO_EBF1_ChIP_rep2_S14_R2.fastq.gz
s15_230103_Granta519EBF1KI_cl27_24hr_H3K4me1_ChIP_rep1_S15.filt.srt.nodup.noBlack.bam.bw
s15_230103_Granta519EBF1KI_cl27_24hr_H3K4me1_ChIP_rep1_S15_R1.fastq.gz
s15_230103_Granta519EBF1KI_cl27_24hr_H3K4me1_ChIP_rep1_S15_R2.fastq.gz
s15_240415_Granta519cl27_24hdTAGWO_SMC1_ChIP_rep1_S15.filt.srt.nodup.noBlack.bam.bw
s15_240415_Granta519cl27_24hdTAGWO_SMC1_ChIP_rep1_S15_R1.fastq.gz
s15_240415_Granta519cl27_24hdTAGWO_SMC1_ChIP_rep1_S15_R2.fastq.gz
s15_240427_Granta519cl27_6hWO_SMC1_ChIP_rep1_S15.filt.srt.nodup.noBlack.bam.bw
s15_240427_Granta519cl27_6hWO_SMC1_ChIP_rep1_S15_R1.fastq.gz
s15_240427_Granta519cl27_6hWO_SMC1_ChIP_rep1_S15_R2.fastq.gz
s16_230103_Granta519EBF1KI_cl27_24hr_H3K4me1_ChIP_rep2_S16.filt.srt.nodup.noBlack.bam.bw
s16_230103_Granta519EBF1KI_cl27_24hr_H3K4me1_ChIP_rep2_S16_R1.fastq.gz
s16_230103_Granta519EBF1KI_cl27_24hr_H3K4me1_ChIP_rep2_S16_R2.fastq.gz
s16_240415_Granta519cl27_24hdTAGWO_SMC1_ChIP_rep2_S16.filt.srt.nodup.noBlack.bam.bw
s16_240415_Granta519cl27_24hdTAGWO_SMC1_ChIP_rep2_S16_R1.fastq.gz
s16_240415_Granta519cl27_24hdTAGWO_SMC1_ChIP_rep2_S16_R2.fastq.gz
s16_240427_Granta519cl27_6hWO_SMC1_ChIP_rep2_S16.filt.srt.nodup.noBlack.bam.bw
s16_240427_Granta519cl27_6hWO_SMC1_ChIP_rep2_S16_R1.fastq.gz
s16_240427_Granta519cl27_6hWO_SMC1_ChIP_rep2_S16_R2.fastq.gz
s17_230103_Granta519EBF1KI_cl27_24hr_H3K27me3_ChIP_rep1_S17.filt.srt.nodup.noBlack.bam.bw
s17_230103_Granta519EBF1KI_cl27_24hr_H3K27me3_ChIP_rep1_S17_R1.fastq.gz
s17_230103_Granta519EBF1KI_cl27_24hr_H3K27me3_ChIP_rep1_S17_R2.fastq.gz
s18_230103_Granta519EBF1KI_cl27_24hr_H3K27me3_ChIP_rep2_S18.filt.srt.nodup.noBlack.bam.bw
s18_230103_Granta519EBF1KI_cl27_24hr_H3K27me3_ChIP_rep2_S18_R1.fastq.gz
s18_230103_Granta519EBF1KI_cl27_24hr_H3K27me3_ChIP_rep2_S18_R2.fastq.gz
s19_230103_Granta519EBF1KI_cl27_0hr_SMC1_ChIP_rep1_S19.filt.srt.nodup.noBlack.bam.bw
s19_230103_Granta519EBF1KI_cl27_0hr_SMC1_ChIP_rep1_S19_R1.fastq.gz
s19_230103_Granta519EBF1KI_cl27_0hr_SMC1_ChIP_rep1_S19_R2.fastq.gz
s20_230103_Granta519EBF1KI_cl27_0hr_SMC1_ChIP_rep2_S20.filt.srt.nodup.noBlack.bam.bw
s20_230103_Granta519EBF1KI_cl27_0hr_SMC1_ChIP_rep2_S20_R1.fastq.gz
s20_230103_Granta519EBF1KI_cl27_0hr_SMC1_ChIP_rep2_S20_R2.fastq.gz
s21_230103_Granta519EBF1KI_cl27_24hr_SMC1_ChIP_rep2_S21.filt.srt.nodup.noBlack.bam.bw
s21_230103_Granta519EBF1KI_cl27_24hr_SMC1_ChIP_rep2_S21_R1.fastq.gz
s21_230103_Granta519EBF1KI_cl27_24hr_SMC1_ChIP_rep2_S21_R2.fastq.gz
s22_230103_Granta519EBF1KI_cl27_6hr_SMC1_ChIP_rep2_S22.filt.srt.nodup.noBlack.bam.bw
s22_230103_Granta519EBF1KI_cl27_6hr_SMC1_ChIP_rep2_S22_R1.fastq.gz
s22_230103_Granta519EBF1KI_cl27_6hr_SMC1_ChIP_rep2_S22_R2.fastq.gz
s23_230103_Granta519EBF1KI_cl27_24hr_SMC1_ChIP_rep1_S23.filt.srt.nodup.noBlack.bam.bw
s23_230103_Granta519EBF1KI_cl27_24hr_SMC1_ChIP_rep1_S23_R1.fastq.gz
s23_230103_Granta519EBF1KI_cl27_24hr_SMC1_ChIP_rep1_S23_R2.fastq.gz
s24_230103_Granta519EBF1KI_cl27_6hr_SMC1_ChIP_rep1_S24.filt.srt.nodup.noBlack.bam.bw
s24_230103_Granta519EBF1KI_cl27_6hr_SMC1_ChIP_rep1_S24_R1.fastq.gz
s24_230103_Granta519EBF1KI_cl27_6hr_SMC1_ChIP_rep1_S24_R2.fastq.gz
s45_221207_Granta519EBF1KI_cl27_0hr_EBF1_CHIPseq_rep1_S9.filt.srt.nodup.noBlack.bam.bw
s45_221207_Granta519EBF1KI_cl27_0hr_EBF1_CHIPseq_rep1_S9_R1.fastq.gz
s45_221207_Granta519EBF1KI_cl27_0hr_EBF1_CHIPseq_rep1_S9_R2.fastq.gz
s46_221207_Granta519EBF1KI_cl27_0hr_EBF1_CHIPseq_rep2_S10.filt.srt.nodup.noBlack.bam.bw
s46_221207_Granta519EBF1KI_cl27_0hr_EBF1_CHIPseq_rep2_S10_R1.fastq.gz
s46_221207_Granta519EBF1KI_cl27_0hr_EBF1_CHIPseq_rep2_S10_R2.fastq.gz
s47_221207_Granta519EBF1KI_cl27_6hr_EBF1_CHIPseq_rep1_S11.filt.srt.nodup.noBlack.bam.bw
s47_221207_Granta519EBF1KI_cl27_6hr_EBF1_CHIPseq_rep1_S11_R1.fastq.gz
s47_221207_Granta519EBF1KI_cl27_6hr_EBF1_CHIPseq_rep1_S11_R2.fastq.gz
s48_221207_Granta519EBF1KI_cl27_6hr_EBF1_CHIPseq_rep2_S12.filt.srt.nodup.noBlack.bam.bw
s48_221207_Granta519EBF1KI_cl27_6hr_EBF1_CHIPseq_rep2_S12_R1.fastq.gz
s48_221207_Granta519EBF1KI_cl27_6hr_EBF1_CHIPseq_rep2_S12_R2.fastq.gz
s49_221207_Granta519EBF1KI_cl27_8hr_EBF1_CHIPseq_rep1_S13.filt.srt.nodup.noBlack.bam.bw
s49_221207_Granta519EBF1KI_cl27_8hr_EBF1_CHIPseq_rep1_S13_R1.fastq.gz
s49_221207_Granta519EBF1KI_cl27_8hr_EBF1_CHIPseq_rep1_S13_R2.fastq.gz
s50_221207_Granta519EBF1KI_cl27_8hr_EBF1_CHIPseq_rep2_S14.filt.srt.nodup.noBlack.bam.bw
s50_221207_Granta519EBF1KI_cl27_8hr_EBF1_CHIPseq_rep2_S14_R1.fastq.gz
s50_221207_Granta519EBF1KI_cl27_8hr_EBF1_CHIPseq_rep2_S14_R2.fastq.gz
s51_221207_Granta519EBF1KI_cl27_24hr_EBF1_CHIPseq_rep1_S15.filt.srt.nodup.noBlack.bam.bw
s51_221207_Granta519EBF1KI_cl27_24hr_EBF1_CHIPseq_rep1_S15_R1.fastq.gz
s51_221207_Granta519EBF1KI_cl27_24hr_EBF1_CHIPseq_rep1_S15_R2.fastq.gz
s52_221207_Granta519EBF1KI_cl27_24hr_EBF1_CHIPseq_rep2_S16.filt.srt.nodup.noBlack.bam.bw
s52_221207_Granta519EBF1KI_cl27_24hr_EBF1_CHIPseq_rep2_S16_R1.fastq.gz
s52_221207_Granta519EBF1KI_cl27_24hr_EBF1_CHIPseq_rep2_S16_R2.fastq.gz

HiC:
s02_210618_Granta519Cas9_ctrl_Arima_HiC_nova_inter30.hic
s02_210618_Granta519Cas9_ctrl_Arima_HiC_nova_S2_R1_001.fastq.gz

s02_210618_Granta519Cas9_ctrl_Arima_HiC_nova_S2_R2_001.fastq.gz
s03_210618_Granta519Cas9_EBF1g7_Arima_HiC_nova_inter30.hic
s03_210618_Granta519Cas9_EBF1g7_Arima_HiC_nova_S3_R1_001.fastq.gz
s03_210618_Granta519Cas9_EBF1g7_Arima_HiC_nova_S3_R2_001.fastq.gz

HiChIP:
S01_210917_Granta519Cas9_EBF1_RG_HiCHIP_Nova_hicpro.hic
S01_210917_Granta519Cas9_EBF1_RG_HiCHIP_Nova_S1_R1_001.fastq.gz
S01_210917_Granta519Cas9_EBF1_RG_HiCHIP_Nova_S1_R2_001.fastq.gz
S01_211207_Granta519Cas9_SMC1_HiChIP_Nova_hicpro.hic
S01_211207_Granta519Cas9_SMC1_HiChIP_Nova_S1_R1_001.fastq.gz
S01_211207_Granta519Cas9_SMC1_HiChIP_Nova_S1_R2_001.fastq.gz
S02_210917_Granta519Cas9_EBF1_MP_HiCHIP_Nova_hicpro.hic
S02_210917_Granta519Cas9_EBF1_MP_HiCHIP_Nova_S2_R1_001.fastq.gz
S02_210917_Granta519Cas9_EBF1_MP_HiCHIP_Nova_S2_R2_001.fastq.gz

MicroC:
s01_210109_Granta519EBF1KI_cl97_0hr_25U_MicroC_w30KB.hic
s01_230109_Granta519EBF1KI_cl97_0hr_25U_MicroC_Nova_S1_R1_001.fastq.gz
s01_230109_Granta519EBF1KI_cl97_0hr_25U_MicroC_Nova_S1_R2_001.fastq.gz
s01_240711_Granta519EBF1KI_cl27_24hWO_MicroC_25U_Nova_S1_R1_001.fastq.gz
s01_240711_Granta519EBF1KI_cl27_24hWO_MicroC_25U_Nova_S1_R2_001.fastq.gz
s01_240711_Granta519EBF1KI_cl27_24hWO_MicroC_25U_Nova_w30KB.hic
s01_240918_Granta519EBF1KI_cl97_6hWO_25U_MicroC_S1_R1_001.fastq.gz
s01_240918_Granta519EBF1KI_cl97_6hWO_25U_MicroC_S1_R2_001.fastq.gz
s01_240918_Granta519EBF1KI_cl97_6hWO_25U_MicroC_w30KB.hic
s02_230109_Granta519EBF1KI_cl97_24hr_25U_MicroC_Nova_S2_R1_001.fastq.gz
s02_230109_Granta519EBF1KI_cl97_24hr_25U_MicroC_Nova_S2_R2_001.fastq.gz
s02_230109_Granta519EBF1KI_cl97_24hr_25U_MicroC_w30KB.hic
s02_240711_Granta519EBF1KI_cl27_6hWO_MicroC_25U_Nova_S2_R1_001.fastq.gz
s02_240711_Granta519EBF1KI_cl27_6hWO_MicroC_25U_Nova_S2_R2_001.fastq.gz
s02_240711_Granta519EBF1KI_cl27_6hWO_MicroC_25U_Nova_w30KB.hic
s02_240918_Granta519EBF1KI_cl97_24hWO_25U_MicroC_Nova_with30KB.hic
s02_240918_Granta519EBF1KI_cl97_24hWO_25U_MicroC_S2_R1_001.fastq.gz
s02_240918_Granta519EBF1KI_cl97_24hWO_25U_MicroC_S2_R2_001.fastq.gz
s02_241118_DND41_resistant_15U_20U_MicroC_S2_R1.fastq.gz
s02_241118_DND41_resistant_15U_20U_MicroC_S2_R2.fastq.gz
s02_241118_DND41_resistant_15U_20U_MicroC_with30KB.hic
s03_231213_Granta519EBF1KI_cl97_6hr_25U_MicroC_Nova_with30KB.hic
s03_231213_Granta519EBF1KI_cl97_6hr_25U_MicroC_S1_R1_001.fastq.gz
s03_231213_Granta519EBF1KI_cl97_6hr_25U_MicroC_S1_R2_001.fastq.gz
s03_241125_DND41_parental_15U_20U_MicroC_S1_R1_001.fastq.gz
s03_241125_DND41_parental_15U_20U_MicroC_S1_R2_001.fastq.gz
s03_241125_DND41_parental_15U_20U_MicroC_with30KB.hic
s38_221203_Granta519EBF1KI_cl27_0hr_MicroC_25U_Nova_R1.fastq.gz
s38_221203_Granta519EBF1KI_cl27_0hr_MicroC_25U_Nova_R2.fastq.gz
s38_221203_Granta519EBF1KI_cl27_0hr_MicroC_25U_with_30KB.hic
s40_221203_Granta519EBF1KI_cl27_24hr_MicroC_25U_Nova_R1.fastq.gz
s40_221203_Granta519EBF1KI_cl27_24hr_MicroC_25U_Nova_R2.fastq.gz
s40_221203_Granta519EBF1KI_cl27_24hr_MicroC_with30KB.hic
s42_221203_Granta519EBF1KI_cl27_6hr_MicroC_25U_seq2_S18_R1.fastq.gz
s42_221203_Granta519EBF1KI_cl27_6hr_MicroC_25U_seq2_S18_R2.fastq.gz
s42_221203_Granta519EBF1KI_cl27_6hr_MicroC_with30KB.hic

RNAseq:
s01_221115_Granta519EBF1KI_cl26_0hr_RNAseq_rep1_S1_NJ_norm.bw
s01_221115_Granta519EBF1KI_cl26_0hr_RNAseq_rep1_S1_R1.fastq.gz
s01_221115_Granta519EBF1KI_cl26_0hr_RNAseq_rep1_S1_R2.fastq.gz
s01_221126_Granta519EBF1KI_cl29_0hr_RNAseq_rep1_S1_NJ_norm.bw
s01_221126_Granta519EBF1KI_cl29_0hr_RNAseq_rep1_S1_R1.fastq.gz
s01_221126_Granta519EBF1KI_cl29_0hr_RNAseq_rep1_S1_R2.fastq.gz
s01_240415_Granta519cl27_6hdTAGWO_RNAseq_lib1_S1_NJ_norm.bw
s01_240415_Granta519cl27_6hdTAGWO_RNAseq_lib1_S1_R1.fastq.gz
s01_240415_Granta519cl27_6hdTAGWO_RNAseq_lib1_S1_R2.fastq.gz
s02_221115_Granta519EBF1KI_cl26_0hr_RNAseq_rep2_S2_NJ_norm.bw
s02_221115_Granta519EBF1KI_cl26_0hr_RNAseq_rep2_S2_R1.fastq.gz
s02_221115_Granta519EBF1KI_cl26_0hr_RNAseq_rep2_S2_R2.fastq.gz
s02_221126_Granta519EBF1KI_cl29_0hr_RNAseq_rep2_S2_NJ_norm.bw
s02_221126_Granta519EBF1KI_cl29_0hr_RNAseq_rep2_S2_R1.fastq.gz
s02_221126_Granta519EBF1KI_cl29_0hr_RNAseq_rep2_S2_R2.fastq.gz
s02_240415_Granta519cl27_6hdTAGWO_RNAseq_lib2_S2_NJ_norm.bw
s02_240415_Granta519cl27_6hdTAGWO_RNAseq_lib2_S2_R1.fastq.gz
s02_240415_Granta519cl27_6hdTAGWO_RNAseq_lib2_S2_R2.fastq.gz
s03_221115_Granta519EBF1KI_cl26_0hr_RNAseq_rep3_S3_NJ_norm.bw
s03_221115_Granta519EBF1KI_cl26_0hr_RNAseq_rep3_S3_R1.fastq.gz
s03_221115_Granta519EBF1KI_cl26_0hr_RNAseq_rep3_S3_R2.fastq.gz

s03_221126_Granta519EBF1KI_cl29_0hr_RNAseq_rep3_S3_NJ_norm.bw
s03_221126_Granta519EBF1KI_cl29_0hr_RNAseq_rep3_S3_R1.fastq.gz
s03_221126_Granta519EBF1KI_cl29_0hr_RNAseq_rep3_S3_R2.fastq.gz
s03_240415_Granta519cl27_6hdTAGWO_RNAseq_lib3_S3_NJ_norm.bw
s03_240415_Granta519cl27_6hdTAGWO_RNAseq_lib3_S3_R1.fastq.gz
s03_240415_Granta519cl27_6hdTAGWO_RNAseq_lib3_S3_R2.fastq.gz
s04_221115_Granta519EBF1KI_cl26_6hr_RNAseq_rep1_S4_NJ_norm.bw
s04_221115_Granta519EBF1KI_cl26_6hr_RNAseq_rep1_S4_R1.fastq.gz
s04_221115_Granta519EBF1KI_cl26_6hr_RNAseq_rep1_S4_R2.fastq.gz
s04_221126_Granta519EBF1KI_cl29_6hr_RNAseq_rep1_S4_NJ_norm.bw
s04_221126_Granta519EBF1KI_cl29_6hr_RNAseq_rep1_S4_R1.fastq.gz
s04_221126_Granta519EBF1KI_cl29_6hr_RNAseq_rep1_S4_R2.fastq.gz
s04_240415_Granta519cl97_6hdTAGWO_RNAseq_lib1_S4_NJ_norm.bw
s04_240415_Granta519cl97_6hdTAGWO_RNAseq_lib1_S4_R1.fastq.gz
s04_240415_Granta519cl97_6hdTAGWO_RNAseq_lib1_S4_R2.fastq.gz
s05_221115_Granta519EBF1KI_cl26_6hr_RNAseq_rep2_S5_NJ_norm.bw
s05_221115_Granta519EBF1KI_cl26_6hr_RNAseq_rep2_S5_R1.fastq.gz
s05_221115_Granta519EBF1KI_cl26_6hr_RNAseq_rep2_S5_R2.fastq.gz
s05_221126_Granta519EBF1KI_cl29_6hr_RNAseq_rep2_S5_NJ_norm.bw
s05_221126_Granta519EBF1KI_cl29_6hr_RNAseq_rep2_S5_R1.fastq.gz
s05_221126_Granta519EBF1KI_cl29_6hr_RNAseq_rep2_S5_R2.fastq.gz
s05_240415_Granta519cl97_6hdTAGWO_RNAseq_lib2_S5_NJ_norm.bw
s05_240415_Granta519cl97_6hdTAGWO_RNAseq_lib2_S5_R1.fastq.gz
s05_240415_Granta519cl97_6hdTAGWO_RNAseq_lib2_S5_R2.fastq.gz
s06_221115_Granta519EBF1KI_cl26_6hr_RNAseq_rep3_S6_NJ_norm.bw
s06_221115_Granta519EBF1KI_cl26_6hr_RNAseq_rep3_S6_R1.fastq.gz
s06_221115_Granta519EBF1KI_cl26_6hr_RNAseq_rep3_S6_R2.fastq.gz
s06_221126_Granta519EBF1KI_cl29_6hr_RNAseq_rep3_S6_NJ_norm.bw
s06_221126_Granta519EBF1KI_cl29_6hr_RNAseq_rep3_S6_R1.fastq.gz
s06_221126_Granta519EBF1KI_cl29_6hr_RNAseq_rep3_S6_R2.fastq.gz
s06_240415_Granta519cl97_6hdTAGWO_RNAseq_lib3_S6_NJ_norm.bw
s06_240415_Granta519cl97_6hdTAGWO_RNAseq_lib3_S6_R1.fastq.gz
s06_240415_Granta519cl97_6hdTAGWO_RNAseq_lib3_S6_R2.fastq.gz
s07_210730_Granta519_ctrl_RNAseq_rep1_S7_NJ_norm.bw
s07_210730_Granta519_ctrl_RNAseq_rep1_S7_R1.fastq.gz
s07_210730_Granta519_ctrl_RNAseq_rep1_S7_R2.fastq.gz
s07_221115_Granta519EBF1KI_cl27_0hr_RNAseq_rep1_S7_NJ_norm.bw
s07_221115_Granta519EBF1KI_cl27_0hr_RNAseq_rep1_S7_R1.fastq.gz
s07_221115_Granta519EBF1KI_cl27_0hr_RNAseq_rep1_S7_R2.fastq.gz
s07_221126_Granta519EBF1KI_cl97_0hr_RNAseq_rep1_S7_NJ_norm.bw
s07_221126_Granta519EBF1KI_cl97_0hr_RNAseq_rep1_S7_R1.fastq.gz
s07_221126_Granta519EBF1KI_cl97_0hr_RNAseq_rep1_S7_R2.fastq.gz
s07_240415_Granta519cl27_24hdTAGWO_RNAseq_lib1_S7_NJ_norm.bw
s07_240415_Granta519cl27_24hdTAGWO_RNAseq_lib1_S7_R1.fastq.gz
s07_240415_Granta519cl27_24hdTAGWO_RNAseq_lib1_S7_R2.fastq.gz
s08_210730_Granta519_ctrl_RNAseq_rep2_S8_NJ_norm.bw
s08_210730_Granta519_ctrl_RNAseq_rep2_S8_R1.fastq.gz
s08_210730_Granta519_ctrl_RNAseq_rep2_S8_R2.fastq.gz
s08_221115_Granta519EBF1KI_cl27_0hr_RNAseq_rep2_S8_NJ_norm.bw
s08_221115_Granta519EBF1KI_cl27_0hr_RNAseq_rep2_S8_R1.fastq.gz
s08_221115_Granta519EBF1KI_cl27_0hr_RNAseq_rep2_S8_R2.fastq.gz
s08_221126_Granta519EBF1KI_cl97_0hr_RNAseq_rep2_S8_NJ_norm.bw
s08_221126_Granta519EBF1KI_cl97_0hr_RNAseq_rep2_S8_R1.fastq.gz
s08_221126_Granta519EBF1KI_cl97_0hr_RNAseq_rep2_S8_R2.fastq.gz
s08_240415_Granta519cl27_24hdTAGWO_RNAseq_lib2_S8_NJ_norm.bw
s08_240415_Granta519cl27_24hdTAGWO_RNAseq_lib2_S8_R1.fastq.gz
s08_240415_Granta519cl27_24hdTAGWO_RNAseq_lib2_S8_R2.fastq.gz
s09_210730_Granta519_ctrl_RNAseq_rep3_S9_NJ_norm.bw
s09_210730_Granta519_ctrl_RNAseq_rep3_S9_R1.fastq.gz
s09_210730_Granta519_ctrl_RNAseq_rep3_S9_R2.fastq.gz
s09_221115_Granta519EBF1KI_cl27_0hr_RNAseq_rep3_S1_NJ_norm.bw
s09_221115_Granta519EBF1KI_cl27_0hr_RNAseq_rep3_S1_R1.fastq.gz
s09_221115_Granta519EBF1KI_cl27_0hr_RNAseq_rep3_S1_R2.fastq.gz
s09_221126_Granta519EBF1KI_cl97_0hr_RNAseq_rep3_S9_NJ_norm.bw
s09_221126_Granta519EBF1KI_cl97_0hr_RNAseq_rep3_S9_R1.fastq.gz
s09_221126_Granta519EBF1KI_cl97_0hr_RNAseq_rep3_S9_R2.fastq.gz
s09_240415_Granta519cl27_24hdTAGWO_RNAseq_lib3_S9_NJ_norm.bw
s09_240415_Granta519cl27_24hdTAGWO_RNAseq_lib3_S9_R1.fastq.gz
s09_240415_Granta519cl27_24hdTAGWO_RNAseq_lib3_S9_R2.fastq.gz
s10_210730_Granta519_EBF1g7_RNAseq_rep1_S10_NJ_norm.bw
s10_210730_Granta519_EBF1g7_RNAseq_rep1_S10_R1.fastq.gz
s10_210730_Granta519_EBF1g7_RNAseq_rep1_S10_R2.fastq.gz
s10_221115_Granta519EBF1KI_cl27_6hr_RNAseq_rep1_S2_NJ_norm.bw
s10_221115_Granta519EBF1KI_cl27_6hr_RNAseq_rep1_S2_R1.fastq.gz
s10_221115_Granta519EBF1KI_cl27_6hr_RNAseq_rep1_S2_R2.fastq.gz
s10_221126_Granta519EBF1KI_cl97_6hr_RNAseq_rep1_S10_NJ_norm.bw

s10_221126_Granta519EBF1KI_cl97_6hr_RNAseq_rep1_S10_R1.fastq.gz
s10_221126_Granta519EBF1KI_cl97_6hr_RNAseq_rep1_S10_R2.fastq.gz
s10_240415_Granta519cl97_24hdTAGWO_RNAseq_lib1_S10_NJ_norm.bw
s10_240415_Granta519cl97_24hdTAGWO_RNAseq_lib1_S10_R1.fastq.gz
s10_240415_Granta519cl97_24hdTAGWO_RNAseq_lib1_S10_R2.fastq.gz
s11_210730_Granta519_EBF1g7_RNAseq_rep2_S11_NJ_norm.bw
s11_210730_Granta519_EBF1g7_RNAseq_rep2_S11_R1.fastq.gz
s11_210730_Granta519_EBF1g7_RNAseq_rep2_S11_R2.fastq.gz
s11_221115_Granta519EBF1KI_cl27_6hr_RNAseq_rep2_S3_NJ_norm.bw
s11_221115_Granta519EBF1KI_cl27_6hr_RNAseq_rep2_S3_R1.fastq.gz
s11_221115_Granta519EBF1KI_cl27_6hr_RNAseq_rep2_S3_R2.fastq.gz
s11_221126_Granta519EBF1KI_cl97_6hr_RNAseq_rep2_S11_NJ_norm.bw
s11_221126_Granta519EBF1KI_cl97_6hr_RNAseq_rep2_S11_R1.fastq.gz
s11_221126_Granta519EBF1KI_cl97_6hr_RNAseq_rep2_S11_R2.fastq.gz
s11_240415_Granta519cl97_24hdTAGWO_RNAseq_lib2_S11_NJ_norm.bw
s11_240415_Granta519cl97_24hdTAGWO_RNAseq_lib2_S11_R1.fastq.gz
s11_240415_Granta519cl97_24hdTAGWO_RNAseq_lib2_S11_R2.fastq.gz
s12_210730_Granta519_EBF1g7_RNAseq_rep3_S12_NJ_norm.bw
s12_210730_Granta519_EBF1g7_RNAseq_rep3_S12_R1.fastq.gz
s12_210730_Granta519_EBF1g7_RNAseq_rep3_S12_R2.fastq.gz
s12_221115_Granta519EBF1KI_cl27_6hr_RNAseq_rep3_S4_NJ_norm.bw
s12_221115_Granta519EBF1KI_cl27_6hr_RNAseq_rep3_S4_R1.fastq.gz
s12_221115_Granta519EBF1KI_cl27_6hr_RNAseq_rep3_S4_R2.fastq.gz
s12_221126_Granta519EBF1KI_cl97_6hr_RNAseq_rep3_S12_NJ_norm.bw
s12_221126_Granta519EBF1KI_cl97_6hr_RNAseq_rep3_S12_R1.fastq.gz
s12_221126_Granta519EBF1KI_cl97_6hr_RNAseq_rep3_S12_R2.fastq.gz
s12_240415_Granta519cl97_24hdTAGWO_RNAseq_lib3_S12_NJ_norm.bw
s12_240415_Granta519cl97_24hdTAGWO_RNAseq_lib3_S12_R1.fastq.gz
s12_240415_Granta519cl97_24hdTAGWO_RNAseq_lib3_S12_R2.fastq.gz
s19_221115_Granta519EBF1KI_cl26_24hr_RNAseq_rep1_S3_NJ_norm.bw
s19_221115_Granta519EBF1KI_cl26_24hr_RNAseq_rep1_S3_R1.fastq.gz
s19_221115_Granta519EBF1KI_cl26_24hr_RNAseq_rep1_S3_R2.fastq.gz
s19_221126_Granta519EBF1KI_cl29_24hr_RNAseq_rep1_S19_NJ_norm.bw
s19_221126_Granta519EBF1KI_cl29_24hr_RNAseq_rep1_S19_R1.fastq.gz
s19_221126_Granta519EBF1KI_cl29_24hr_RNAseq_rep1_S19_R2.fastq.gz
s20_221115_Granta519EBF1KI_cl26_24hr_RNAseq_rep2_S4_NJ_norm.bw
s20_221115_Granta519EBF1KI_cl26_24hr_RNAseq_rep2_S4_R1.fastq.gz
s20_221115_Granta519EBF1KI_cl26_24hr_RNAseq_rep2_S4_R2.fastq.gz
s20_221126_Granta519EBF1KI_cl29_24hr_RNAseq_rep2_S20_NJ_norm.bw
s20_221126_Granta519EBF1KI_cl29_24hr_RNAseq_rep2_S20_R1.fastq.gz
s20_221126_Granta519EBF1KI_cl29_24hr_RNAseq_rep2_S20_R2.fastq.gz
s21_221115_Granta519EBF1KI_cl26_24hr_RNAseq_rep3_S5_NJ_norm.bw
s21_221115_Granta519EBF1KI_cl26_24hr_RNAseq_rep3_S5_R1.fastq.gz
s21_221115_Granta519EBF1KI_cl26_24hr_RNAseq_rep3_S5_R2.fastq.gz
s21_221126_Granta519EBF1KI_cl29_24hr_RNAseq_rep3_S21_NJ_norm.bw
s21_221126_Granta519EBF1KI_cl29_24hr_RNAseq_rep3_S21_R1.fastq.gz
s21_221126_Granta519EBF1KI_cl29_24hr_RNAseq_rep3_S21_R2.fastq.gz
s22_221115_Granta519EBF1KI_cl27_24hr_RNAseq_rep1_S6_NJ_norm.bw
s22_221115_Granta519EBF1KI_cl27_24hr_RNAseq_rep1_S6_R1.fastq.gz
s22_221115_Granta519EBF1KI_cl27_24hr_RNAseq_rep1_S6_R2.fastq.gz
s22_221126_Granta519EBF1KI_cl97_24hr_RNAseq_rep1_S22_NJ_norm.bw
s22_221126_Granta519EBF1KI_cl97_24hr_RNAseq_rep1_S22_R1.fastq.gz
s22_221126_Granta519EBF1KI_cl97_24hr_RNAseq_rep1_S22_R2.fastq.gz
s23_221115_Granta519EBF1KI_cl27_24hr_RNAseq_rep2_S7_NJ_norm.bw
s23_221115_Granta519EBF1KI_cl27_24hr_RNAseq_rep2_S7_R1.fastq.gz
s23_221115_Granta519EBF1KI_cl27_24hr_RNAseq_rep2_S7_R2.fastq.gz
s23_221126_Granta519EBF1KI_cl97_24hr_RNAseq_rep2_S23_NJ_norm.bw
s23_221126_Granta519EBF1KI_cl97_24hr_RNAseq_rep2_S23_R1.fastq.gz
s23_221126_Granta519EBF1KI_cl97_24hr_RNAseq_rep2_S23_R2.fastq.gz
s24_221115_Granta519EBF1KI_cl27_24hr_RNAseq_rep3_S8_NJ_norm.bw
s24_221115_Granta519EBF1KI_cl27_24hr_RNAseq_rep3_S8_R1.fastq.gz
s24_221115_Granta519EBF1KI_cl27_24hr_RNAseq_rep3_S8_R2.fastq.gz
s24_221126_Granta519EBF1KI_cl97_24hr_RNAseq_rep3_S24_NJ_norm.bw
s24_221126_Granta519EBF1KI_cl97_24hr_RNAseq_rep3_S24_R1.fastq.gz
s24_221126_Granta519EBF1KI_cl97_24hr_RNAseq_rep3_S24_R2.fastq.gz

Genome browser session
(e.g. UCSC)

https://genome.ucsc.edu/cgi-bin/hgTracks?db=hg19&lastVirtModeType=default&lastVirtModeExtraState=&virtModeType=default&virtMode=0&nonVirtPosition=&position=chr8%3A127000000%2D129000000&hgsid=2518550251_vAYJj0yCvG2dAbchK7MmDPyNVZMo

Methodology

Replicates

2 biological replicates per cell line per condition.

Sequencing depth	Paired-end sequenced on Illumina NextSeq 550 (38bp+38bp) or Novaseq 6000 (61bp+61bp). 35 - 100 million reads per sample.
Antibodies	H3K27ac (Active Motif cat# 39133), H3K4me1 (Abcam cat# ab8895), H3K27me3 (CST cat# 9733),polyclonal anti-EBF1 (1C) antibody, which recognizes an N-terminal EBF1 peptide (RG), commercial EBF1 antibody (Millipore cat# AB10523), SMC1a (Bethyl, cat# A300-055A), YY1 (Active motif cat# 61779), CTCF (EMD Millipore cat# 07-729)
Peak calling parameters	As below
Data quality	ChIP-seq data analysis For Granta519 EBF1 ChIPseq, peaks of each library were identified using MACS2 (version 2.0.9)95- with parameters -p 1E-3 -g hs --nomodel --shiftsize=0.5*fragment_length --format=BAM --bw=300 --keep-dup=1 and with corresponding input control. 25,227 reproducible EBF1 ChIP-seq peaks identified in libraries of both replicates of both antibodies were used in downstream analyses. For comparing protein loading, reproducible EBF1-bound regions were quantified on each ChIP-seq bam files using bedtools 'coverage' and normalized to RPKM and averaged between the two replicates of each antibody. Clustering of reproducible EBF1-bound regions (Fig. 1A) was performed with R function hclust(dc, method="average", members=NULL) and hc_tree <- cutree(hc, k = 15) and visualized with 'pheatmap'. Dynamic EBF1 peaks were filtered as reproducible EBF1 peaks > 1 averaged RPKM in untreated Granta519-EBF1-FKBP-KI clone 27. 7,777 peaks with Log2(fold change) < -1 of averaged RPKM between 6h and 24h dTAG-treated versus untreated and Log2(fold change) > 1 of averaged RPKM between 6h and 24h washout versus 24h dTAG-treated were defined as dynamic EBF1 peaks. SMC1, CTCF and YY1 ChIP-seq libraries were individually quantified on EBF1 peaks using bedtools 'coverage' and normalized to RPKM and averaged between the two replicates per condition, and Log2 fold changes were calculated as above. For tag density plots, aligned bam files of the two replicates of each condition were merged using samtools (version 1.3)97 'cat' command. For each merged library, fragment length was estimated with HOMER 'makeTagDirectory'. HOMER 'annotatePeaks.pl' was used on merged libraries and visualized with R function 'pheatmap'. For merged libraries genome tracks, bedgraph of reads normalized to reads per million (RPM) were generated with bedtools 'genomecov'. Selected genomic loci were visualized with R package Sushi (version 1.18.0)98 function 'plotBedgraph'. Genome-wide uploadable bigWig files were generated with UCSC tools (version 329)99 'bedGraphToBigWig'.
Software	As above

Flow Cytometry

Plots

Confirm that:

☒ The axis labels state the marker and fluorochrome used (e.g. CD4-FITC).

☒ The axis scales are clearly visible. Include numbers along axes only for bottom left plot of group (a 'group' is an analysis of identical markers).

☒ All plots are contour plots with outliers or pseudocolor plots.

☒ A numerical value for number of cells or percentage (with statistics) is provided.

Methodology

Sample preparation	Flowcytometry analysis Granta519-Cas9, JVM-2-Cas9 and PGA-1-Cas9 cells with control or LRmCherry2.1-EBF1-g7 were sorted 3 days post transduction and cultured for 3 days (day 6). For each replicate, 5x105 cells were washed in 1X PBS and resuspended in 100 µl 1X Annexin V binding buffer (BD cat# 556454). 5 µL FITC-Annexin V (BD cat# 556420) was added and incubated in the dark at room temperature for 15min. 400 µL of 1X Annexin V binding buffer containing 1:1000 TO-PRO3 (ThermoFisherScientific cat# R37170) was added and immediately proceeded to Flow cytometry analysis on BD LSR II. 1x106 Granta519 EBF1-FKBP-KI clones 27 and 97 were treated with 125 nM dTAG for 0, 6 and 24 hours and stained with L/D Aqua (Invitrogen cat# L34957) for 15 min at room temperature. Cells were washed with 1X PBS and then stained with 5 µL APC human anti-PD-L1 (BioLegend cat# 329708) in 100 µL 1X PBS for 15 min on ice before analysis on BD LSR II. Experiments were repeated three times with 3-5 replicates per condition.
Instrument	BD LSR II
Software	BD FACSDiva 8.0.2
Cell population abundance	1,000,000 cells were measured per replicate.
Gating strategy	FSC / SSC gating for cells and excluding debris. SSC-H / SSC-A gating for singlets. DAPI or L/D aqua negative for live cells. mCherry + for gRNA-transfected cells. APC / FITC for apoptotic or dead cells.

☒ Tick this box to confirm that a figure exemplifying the gating strategy is provided in the Supplementary Information.